THE THERMOMECHANICAL RESPONSE OF OIL SHALE

by

Peter Michael Switchenko
B.S., Trinity College
1977

SUBMITTED IN PARTIAL FULFILLMENT
OF THE REQUIREMENTS FOR THE
DEGREE OF

MASTER OF SCIENCE

at the

MASSACHUSETTS INSTITUTE OF TECHNOLOGY

August, 1979

Signature redacted

Signature of Author.....
Department of Mechanical Engineering, August 22, 1979

Signature redacted

Certified by.....
Thesis Supervisor

Signature redacted

Accepted by.....
Chairman, Department Committee

THE THERMOMECHANICAL RESPONSE OF OIL SHALE

by

Peter Michael Switchenko

Submitted to the Department of Mechanical Engineering on August 22, 1979 in partial fulfillment of the requirements for the Degree of Master of Science.

ABSTRACT

The general background on oil shale and shale oil extraction in situ is discussed with emphasis on the technology needed to successfully implement the various access, preparation, and retorting sequences. In particular, the need for an adequate thermomechanical characterization is emphasized. To initiate this characterization, high temperature tests were performed for deformation and fracture response on representative samples of oil shale (assayed at 26.5 to 34.4 gpt) from Anvil Points, Colorado. Homogeneous uniaxial testing in tension and compression was conducted to 204°C on cores cut parallel, normal and at $\theta=\pi/4$ to bedding; triaxial compression tests were performed at 21°C to elicit response to simulated confinement. Significant nonlinear straining was observed in both uniaxial and triaxial tests, due to growth of microcracks and increased shale compliance at higher temperatures. Tensile (compressive) strengths/strains at 21°C were about 2 MPa (73 MPa)/.2mε (12mε), 8 MPa (65 MPa)/1mε (6mε), and 6 MPa (64 MPa)/.4mε (7mε) perpendicular, parallel, and at $\theta=45°$ to bedding, respectively. To 204°C, the compressive strength (strain) decreased (increased) roughly five-fold; Young's moduli decreased by two hundred-fold over that same temperature range. Tensile strength decreased, with temperature, twice as fast normal to bedding as parallel to bedding, suggesting the more dominant role of organic breakdown in overall shale response. Failures and thermal cracking tended to occur more along the bedding with increasing temperature. The effect of confinement up to 69 MPa (10,000 psi) increased tangent moduli about two-fold, strengths three-fold, and failure strains ten-fold, both normal and parallel to bedding. Coefficients of thermal expansion were calculated at $1.1\times10^{-5}/°C$ and $2.8\times10^{-5}/°C$, parallel and normal to bedding, respectively.

Significant stress-induced anisotropies and hysteresis were observed in compressive stress cycling and relief tests on shale specimens. Cores cut normal to bedding exhibited the greatest relief and hysteresis (on unloading) at 21°C, while those at $\theta = \pi/4$ to bedding exhibited the most relief and hysteresis at 204°C.

Additional data, including thermal effects, were incorporated into the general constitutive relation. As well, a strength characterization model was initiated.

Fracture toughness measurements, using the J-integral method, were made to 93°C on the nominal 30 gpt shale for characterization in the three relevant crack orientation geometries (divider, arrester, and short transverse). The divider and short transverse geometries showed highest and lowest toughnesses, respectively, at maximum load; the unconfined arrester and divider were comparable, up to 38°C, at the onset of crack growth. Toughness values generally had increased two-fold by 93°C, but arrester decreased two-fold. Indeed, added confinement (2 MPa), at 21°C in arrester tests, lowered the toughness value, due to channeling of stress: even so, toughness increased two-fold to 93°C. Extensive subcritical crack growth, before macro-fracturing was observed to 93°C, but minimal thermal cracking was detected along the bedding at temperatures greater than 93°C.

Comparable uniaxial and fracture toughness tests at 21°C were done on a reservoir sandstone. Tensile (compressive) strengths/strains were about 2 MPa (50 MPa)/ .5 me (3 me); Young's modulus was found to be roughly 12 GPa. J-integral toughness measured at maximum load averaged 35 Joules/m^2, about one-half of that derived in the shale divider and arrester toughness tests. Motivation for these tests lay in the consideration of schemes for producing contained fractures toward access to the shale formation: some interesting conclusions can be drawn about barriers to fracture spreading and other structural considerations.

Thesis Supervisor: Michael P. Cleary
Title: Associate Professor of Mechanical Engineering

TABLE OF CONTENTS

Page

Abstract..... 2

List of Figures..... 5

List of Tables..... 14

Acknowledgements..... 16

Introduction..... 17

Background..... 24

Experimental Procedure..... 49

Experimental Results and Discussion..... 58

Conclusions..... 157

Appendix I - Specimen Preparation..... 164

Appendix II - High Temperature Uniaxial Tension Tension Testing Procedure..... 170

Appendix III - Electronic Equipment for Load and Strain Measurement and High Temperature Calibration Procedures..... 174

Appendix IV - High Temperature Uniaxial Compression Testing Procedure..... 179

Appendix V - High Temperature Fracture Toughness Testing Procedure..... 181

Appendix VI - Triaxial Testing Procedure..... 185

Appendix VII - Generalized Constitutive Relation and Curve Fits..... 187

Appendix VIII - Strength Envelopes Derivation..... 200

References..... 204

LIST OF FIGURES

Figure Number		Page
1	Diagram of crack geometries for transversely isotropic oil shale.....	54
2a	Axial stress vs. axial strain for unconfined tension perpendicular to bedding for nominal 30 gpt shale. Larger number designations indicate temperature is °C smaller designations specify particular test specimens.....	59
2b	Axial stress vs. transverse strain for unconfined tension perpendicular to bedding for nominal 30 gpt shale.....	60
3a	Axial stress vs. axial strain for unconfined tension parallel to bedding for nominal 30 gpt shale.....	62
3b	Axial stress vs. transverse strain for unconfined tension parallel to bedding for nominal 30 gpt shale. Transverse strain measured normal to bedding.....	63
3c	Axial stress vs. transverse strain for unconfined tension parallel to bedding for nominal 30 gpt shale. Transverse strain measured parallel to bedding.....	64
4	New directional vectors for specimens tested at angle θ to the normal vector. Direction $\underset{\sim}{e}_1$ is arbitrarily chosen to coincide with the original $\underset{\sim}{t}$ direction.....	66
5a	Axial stress vs. axial strain for unconfined tension 45° to bedding for nominal 30 gpt shale.....	67
5b	Axial stress vs. transverse strain for unconfined tension 45° to bedding for nominal 30 gpt shale. Transverse strain measured in $\underset{\sim}{e}_2$ direction.....	68

LIST OF FIGURES (CONTINUED)

Figure Number		Page
5c	Axial stress vs. transverse strain for unconfined tension 45° to bedding for nominal 30 gpt shale. Transverse strain measured in $\underline{e}_1$ direction.....	69
6	Nominal 30 gpt shale specimens failed in uniaxial tension at various temperatures. //, ⊥, and 45° refer to tests parallel, perpendicular, and at 45° to bedding, respectively.....	74
7	Direct platen loading and resultant material stress state.....	76
8a	Axial stress vs. axial strain for unconfined compression perpendicular to bedding for nominal 30 gpt shale. Compressive stress taken as positive.....	78
8b	Axial stress vs. transverse strain for unconfined compression perpendicular to bedding for nominal 30 gpt shale. Compressive stress taken as positive.....	79
9a	Axial stress vs. axial strain for unconfined compression parallel to bedding for nominal 30 gpt shale. Compressive stress taken as positive.....	82
9b	Axial stress vs. transverse strain for unconfined compression parallel to bedding for nominal 30 gpt shale. Transverse strain measured normal to bedding. Compressive stress taken as positive.....	83
9c	Axial stress vs. transverse strain for unconfined compression parallel to bedding for nominal 30 gpt shale. Transverse strain measured parallel to bedding. Compressive stress taken as positive.....	84

LIST OF FIGURES (CONTINUED)

Figure Number		Page
10a	Axial stress vs. axial strain for unconfined compression 45° to bedding for nominal 30 gpt shale. Compressive stress taken as positive.....	86
10b	Axial stress vs. transverse strain for unconfined compression 45° to bedding for nominal 30 gpt shale. Transverse strain measured in $\tilde{e}_2$ direction. Compressive stress taken as positive.....	87
10c	Axial stress vs. transverse strain for unconfined compression 45° to bedding for nominal 30 gpt shale. Transverse strain measured in $\tilde{e}_1$ direction. Compressive stress taken as positive.....	88
11a	Nominal 30 gpt shale specimens failed in uniaxial compression at various temperatures $\perp$ designates tests perpendicular to bedding.....	92
11b	Nominal 30 gpt shale specimens failed in uniaxial compression at various temperatures. // designates tests parallel to bedding.....	93
11c	Nominal 30 gpt shale specimens, 45° to bedding, failed in uniaxial compression at various temperatures.....	94
12	Plots of compressive failure strengths vs. temperatures for tests perpendicular and 45° to bedding for nominal 30 gpt shale. Compressive failure strengths taken as positive.....	97
13	Axial stress vs. axial and transverse strains for unconfined compression perpendicular to bedding for nominal 30 gpt shale. First, second and tenth designate the first, second and tenth cycles, respectively. Compressive stress taken as positive.....	100

LIST OF FIGURES (CONTINUED)

Figure Number		Page
14a	Axial stress vs. axial and transverse strains for unconfined compression parallel to bedding at 21°C for nominal 30 gpt shale. Transverse strain, ε_{nn}, measured perpendicular to bedding. Compressive stress taken as positive.....	101
14b	Axial stress vs. transverse strain for unconfined compression parallel to bedding at 21°C for nominal 30 gpt shale. Transverse strain measured parallel to bedding. Compressive stress taken as positive.....	102
15a	Axial stress vs. axial and transverse strains for unconfined compression 45° to bedding at 21°C for nominal 30 gpt shale. Transverse strain measured in $\underset{\sim}{e}_2$ direction. Compressive stress taken as positive.....	103
15b	Axial stress vs. transverse strains for unconfined compression 45° to bedding at 21°C for nominal 30 gpt shale. ε_{32} and ε_{11} strains measured in $\underset{\sim}{e}_1$ and $\underset{\sim}{n}$ directions, respectively. Compressive stress taken as positive.....	104
16a	Axial stress vs. axial and transverse strains at 21°C for cycling and stress relief for unconfined compression normal to bedding. Stress relief at 80% of failure load with one, two, five, ten, and thirty minute increments shown for the nominal 30 gpt shale. Compressive stress taken as positive.....	106

LIST OF FIGURES (CONTINUED)

Figure Number		Page
16b	Axial stress vs. axial and transverse strains at 93°C for stress cycling and relief for unconfined compression normal to bedding. One, two, five, ten, and thirty minute increments shown for nominal 30 gpt shale. Compressive stress taken as positive.....	107
16c	Axial stress vs. axial strain at 204°C for stress cycling and relief for unconfined compression normal to bedding. One, two, five, ten, and thirty minute increments shown for nominal 30 gpt shale. Compressive stress taken as positive.....	108
17a	Axial stress vs. axial and transverse strains at 21°C for stress cycling and relief for unconfined compression parallel to bedding. Transverse strain measured normal to bedding. One, two, five, ten and thirty minute increments shown for nominal 30 gpt shale. Compressive stress taken as positive.....	109
17b	Axial stress vs. axial (T=93°) and transverse (T=21°) strains for stress cycling and relief for unconfined compression parallel to bedding. Transverse strain measured parallel to bedding for nominal 30 gpt shale. Compressive stress taken as positive.....	110
17c	Axial stress vs. transverse strains at 93°C for stress cycling and relief for unconfined compression parallel to bedding. ε_{nn} and ε_{tt} represent transverse strains normal and parallel to bedding, respectively, for nominal 30 gpt shale. Compressive stress taken as positive.....	111

LIST OF FIGURES (CONTINUED)

Figure Numbers		Page
17d	Axial stress vs. axial strain at 204°C for stress cycling and relief for unconfined compression parallel to bedding. One, two, five, ten, and thirty minute increments shown for nominal 30 gpt shale. Compressive stress taken as positive.....	112
18a	Axial stress vs. axial and transverse strains at 21°C for stress cycling and relief for unconfined compression at 45° to bedding. Transverse strain ε_{11}, measured in $\underset{\sim}{e}_1$ direction for nominal 30 gpt shale. Compressive stress taken as positive.....	113
18b	Axial stress vs. axial (T=93°C) and transverse (T=21°C) strains for stress cycling and relief for unconfined compression 45° to bedding. Transverse strain, ε_{22}, measured in $\underset{\sim}{e}_2$ direction for nominal 30 gpt shale. Compressive stress taken as positive.....	114
18c	Axial stress vs. transverse strains at 93° for stress cycling and relief for unconfined compression 45° to bedding. ε_{11} and ε_{22} represent transverse strains measured in $\underset{\sim}{e}_1$ and $\underset{\sim}{e}_2$ directions, respectively, for nominal 30 gpt shale. Compressive stress taken as positive.....	115
18d	Axial stress vs. axial strain at 204°C for stress cycling and relief for unconfined compression 45° to bedding. One, two, five, ten, and thirty minute increments shown for nominal 30 gpt shale. Compressive stress taken as positive.....	116

LIST OF FIGURES (CONTINUED)

Figure Numbers		Page
19	Deviatoric stress vs. axial strain for triaxial compression perpendicular to bedding at 21°C for nominal 30 gpt shale. Plots are 0, 3ksi, 5 ksi and 10 ksi confining pressure are shown. Compressive stress taken as positive.....	119
20	Deviatoric stress vs. axial strain for triaxial compression parallel to bedding at 21°C for nominal 30 gpt shale. Plots for 0, 3 ksi and 10 ksi confining pressure are shown. Compressive stress taken as positive.....	120
21	Nominal 30 gpt specimens failed in triaxial compression at 21°C. //, ⊥, and 45° refer to tests parallel, normal, and 45° to beds, respectively.....	123
22	Load vs. load-point displacement plot for compact tension specimen in the divider orientation. Pt. A refers to point of 2% deviation from power law for nominal 30 gpt shale at various temperatures.....	128
23	Load vs. load-point displacement plot for compact tension specimens in the short transverse orientation. Pt. A refers to point of 2% deviation from power law for nominal 30 gpt shale at various temperatures.....	129
24	Load vs. load-point displacement plot for compact tension specimens in the arrester orientation. Pt. A refers to point of 2% deviation from power law for nominal 30 gpt shale at various temperatures.....	130

LIST OF FIGURES (CONTINUED)

Figure Numbers		Page
25	Load vs. load-point displacement plot for compact tension specimens in the arrester orientation with confinement. Pt. A refers to point of 2% deviation from power law for nominal 30 gpt shale at various temperatures.....	132
26	Load vs. load-point displacement plot for compact tension specimen in the arrester orientation with cycling. Test at 21°C for nominal 30 gpt shale.....	138
27	Load vs. load-point displacement plot for compact tension specimen in the divider orientation with cycling. Test at 21°C for nominal 30 gpt shale.....	139
28	Load vs. load-point displacement plot for compact tension specimen in the short transverse orientation with cycling. Test at 21° for nominal 30 gpt shale.....	140
29	Axial stress vs. axial and transverse strains for uniaxial tension for a Kirkwood sandstone.....	150
30	Axial stress vs. axial and transverse strains for uniaxial compression for a Kirkwood sandstone. Compressive stress taken as positive.....	151
31	Load vs. load-point displacement plot for compact tension specimens for a Kirkwood sandstone.....	155

LIST OF FIGURES (CONTINUED)

Figure Number		Page
I-1	Compact tension design for measurement of fracture toughness, J, in the shale and sandstone specimens	169
II-1	Tensile specimen, grips, and attached strain gages prior to heat-up and testing in the environmental chamber	173
III-1	Cart with electronic equipment and X-Y recorders for data acquisition	176
IV-1	Compression specimen, gages and compression cage prior to heat-up and testing in the environmental chamber	180
V-1	Compact tension arrangement, with the compression gig, LVDT's and grips in the Instron chamber	182

LIST OF TABLES

Table Number		Page
I	Average chemical composition of Green River Shale	25
II	Fuel resources of the United States (1973).	28
III	Results of Fischer Assay	50
IV	Initial tangent moduli, Poisson ratios, and failure strengths and strains for nomial 30 gpt shale at elevated temperatures in uniaxial tension	72
V	Initial tangent moduli, Poisson ratios, and failure strengths and strains for nomial 30 gpt shale at elevated temperatures in uniaxial compression	81
VI	Initial tangent moduli, and failure strengths and strains versus confining stress for nomial 30 gpt shale at ambient temperature	121
VII	High temperature fracture toughness data for nominal 30 gpt shale	134
VIII	Comparison of shale toughness data at ambient temperature	144
IX	Uniaxial tension and compression results for a Kirkwood sandstone	152
X	Fracture toughness data for a Kirkwood sandstone	156

LIST OF TABLES (CONTINUED)

Table Number		Page
XI	Quadratic curve fits	197
XII	Linear strain fits	198
XIII	Individual specimen plots and range of strain values employed in curve fits	199
XIV	Data for strength envelope characterization	203

ACKNOWLEDGEMENTS

I am grateful to Professor Michael P. Cleary for suggesting this work and for providing financial support through a Research Assistantship and National Science Foundation Traineeship. His support throughout the duration of this work is appreciated.

I would also like to thank Dr. Weldon Wilkening and Mr. Wayne Hawkins, who, with their experimental expertise, assisted me in overcoming some of the many problems encountered during the tests.

I am especially grateful to my wife, Pat, for her support and understanding these past two years. Her moral assistance, particularly the last couple of months, helped me complete this thesis on time.

The speedy typing of this thesis by Mary and Nancy Toscano is also most appreciated.

INTRODUCTION

The emergence of the current energy crisis and the prospective energy needs of the American economy have necessitated the search for alternative sources of energy. In an effort to decrease our dependence on foreign oil, which currently accounts for approximately fifty percent of total U.S. consumption (18 million barrels* (bbl) per day), interest is now being focused on potential energy resources lying within our own borders. One such alternative energy source, now coming under closer scrutiny, is in the generation of synthetic fuels (e.g. by use of gasified coal, natural gas, tar sands, oil shale). The potential reserves from our oil shale deposits alone are massive. In particular, the high grade shale deposits in the Green River Formation of Colorado, Utah, and Wyoming have been estimated to contain the equivalent of 600-1200 billion barrels of oil, an amount comparable to the known world reserves (Cameron Engineers, 1975). Roughly 600 billion barrels are accessible and of sufficient grade (greater than 20 gallons per ton) to make it exploitable. To date, however, the costs of aboveground retorting, e.g., as proposed by Fenix and Scisson (1975) and Cameron Engineers (1975), have been prohibitive for commercial exploitation. Within the limits of current technology, the small-scale cost of mining oil shale by conventional drill and blast methods, retorting

*One barrel is equivalent to 42.4 U.S. gallons.

and subsequent refining causes the cost of the "syncrude" to be greater than the present price of imported foreign crude (ca. $18 per bbl*). However, with oil import costs estimated to increase approximately 20% per year (James, 1979), with non-contract sales currently yielding upwards from $23.50 per bbl on the world "spot-market", and while the availability of oil from conventional sources is being commonly estimated to deplete within two decades, added incentive is given to exploitation of our oil shale-rich regions.

The above considerations have stirred interest and research support for innovative mining technologies (e.g. Peterson, 1977). It should be pointed out that these novel technologies do not pertain exclusively to the shale oil extraction process: the research should have great value, as well, toward the structural understanding and machinery innovations needed for other in situ processes (e.g. coal gasification in the extensive coal areas of the U.S.). However, there are stringent requirements for any proposed method, including 1) technical feasibility, 2) cost effectiveness (for commercialization), and 3) environmental acceptability. In-depth laboratory and analytical studies of the proposed methods should initially be performed to test for thermomechanical feasibility, as dictated by

---

*Saudi Arabian price resulting from latest increase - O. P. E. C. conference, June, 1979.

a thorough evaluation of actual field conditions. Once the thermomechanical feasibility has been verified, economical and ecological evaluations can then be conducted.

From preliminary analyses, some proposed methods for shale oil recovery, involving a combination of in situ retorting and specialized conventional mining processes which minimize expansion room excavation, appear technically attractive. Some special conventional mining (Peterson, 1977) may be required to obtain the necessary homogeneous permeability and/or self-containment for the in situ process. However, from initial tests, it is apparent that for any in situ method to be cost effective, the procedure must require minimal excavation mining, while still being technically feasible. The costs of access shafts, haulage drifts, etc.,(Dravo Corporation, 1974) are prohibitive in shale oil extraction.

In particular, to properly assess the in situ process, a technique is required to adequately perform structural analyses for understanding static and dynamic deformation and fracture, thermomechanical response, and general stability in the process zone. These factors are all crucial in any effort at in situ extraction. The current level of understanding seems to be far below that needed for a successful assessment of the proposed process. The U.S. Bureau of Mines has sponsored considerable work for years in the oil shale area (e.g. see Hendrickson, 1974), along

with several experimental mines operated by oil company consortiums (e.g. Continental Oil, Shell Oil, Occidental) but, to date, most operations have been conventional in scope.

The purpose and goals of this study are to: 1) give background to the state-of-the-art situation with reference to problems involved in an in situ process, 2) explain our approach to the problems, 3) examine what technical knowledge is needed to implement the various concepts for in situ processes, 4) analyze new data for quasi-static thermomechanical and thermophysical behavior, 5) qualitatively characterize the thermo-deformation and fracture mechanism response, 6) continue in the development of a nonlinear constitutive model introduced by Cleary (1978b), 7) initiate the development of strength envelopes, 8) propose other pertinent tests (experimental and analytical) to obtain necessary data for the in situ process, and 9) propose an overall feasibility of in situ extraction of shale oil based on completed tests.

Additional data for oil shale response to stress and temperature were obtained by means of the following tests: uniaxial tension (21°C to 149°C), uniaxial compression (21°C to 204°C), compressive stress cycling and stress relief (21°C to 204°C), triaxial compression (21°C), and "compact tension" fracture toughness (21°C to 149°C). Cyclic loading was performed during particular uniaxial compression

and fracture toughness tests in order to respectively elicit the material's unloading response from stresses near failure (stress-induced anisotropies), and to determine the loss (if any) of material toughness due to growth of microcrack arrays ahead of crack tips (or some other dissipative process).

Comparative uniaxial and fracture toughness tests were also performed on a Kirkwood sandstone from Illinois. These tests afforded initial but approximate quantitative and qualitative contrasts to the shale results. More complex triaxial and confined toughness experiments are planned in proceeding research. These tests are required not only on sandstone, but on other rock types which may surround the oil shale stratum. This information will aid considerably in successful containment and efficient process control in the retort zone.

Previous tensile test data, specifically concerning oil shale, have been provided by Merrill (1954), Schmidt (1977), Hangen (1977); as well, some triaxial testing has been done (e.g. Chang and Bondurant, 1979). Various fracture geometries have been employed (e.g. Schmidt, 1975; Hangen, 1977). These uniaxial and triaxial tests are important, both in the constitutive modeling herein, which requires information about the shale's deformation response to all paths in stress and temperature space, and conjunctively in performing relevant structural analyses. Also, the

effective toughness of the oil shale must be determined, in examining the relative merits of any type of mining or fracturing (e.g. hydraulic, explosive), in order to characterize the crack propagation behavior.

Therefore, to expound further on the results presented by Hangen (1977), this report hopes to initiate an adequate (although still primitive) understanding of the complex thermomechanical response of oil shale. This response includes: deformability and strength variations versus temperature, high temperature failure mechanisms, thermal expansion, and diffusivity of heat and melted kerogen. Understanding this temperature dependence is crucial for any in situ shale oil extraction process, since temperatures of order the retort value (about 400°C) will occur in regions near the occurrence of kerogen-matrix separation. This thesis expands work already done on a transversely-isotropic constitutive relation - suggested by the symmetrically-bedded nature of oil shale; it accounts for temperature effects and introduces a convenient strength characterization. This research in unique in the thermo-mechanical characterization of oil shale.

This investigation should give qualitative credibility to a proposed in situ method, by providing a basic thermal characterization. Qualitative insight is also obtained into the exploitative possibilities of other interesting extraction schemes. Suggestions are therefore made on the

overall feasibility of these schemes and the current technical problems associated with them.

I. BACKGROUND

A. Physical Description, Occurrence, and Origin

The designation "oil shale" pertains to a diverse group of fine-grained sedimentary rocks composed primarily of inorganic material and containing an average of 14% refractory organic material (see Table I). Approximately 90% of the earth's continental area is covered with sedimentary rocks, of which an estimated 5% are shales with an organic content (normally expressed in terms of gallons per ton (gpt)) of 5% or greater. The range of organic content in oil shales extends from a lower end of roughly 10 gpt (3.8 weight percent organics) to a value of 200 gpt (90^{+} wgt.% organics) found in some Australian shales (Yen, 1976b). Typical values lie in the 20 gpt to 30 gpt range; 10 gpt is generally considered a lower limit for exploitation. The organic material (kerogen) consists of complex polycyclic subunits interconnected by long chain alkanes and fatty acids. The extensive cross-linking of the subunits leads to the insoluble nature of kerogen. Pyrolysis of the crushed shale at atmospheric pressure and about 400°C (800°F) yields 60% by weight oil vapor, 18% gases, 15% carbonaceous residue, and 7% water vapor, on average (Yen, 1976b). The residue contains traces of uranium, iron, vanadium, and other elements which in reaction with

TABLE I

AVERAGE CHEMICAL COMPOSITION ON GREEN RIVER SHALE (YEN, 1976b)

Inorganic Mineral Matter (86.2 wgt %)		Organic Matter (13.8 wgt %)	
Dolomite and calcite (marlstone)	43.1	Bitumen (soluble in CS_2)	2.8
Feldspar	16.4	Kerogen (insoluble in CS_2)	11.0
Illite	12.9		
Quartz	8.6		
(Rest)	5.2		

the noble metals pose serious environmental considerations (discussed later).

Although their exact origin is speculative because of the diffuse range of environmental conditions in different areas, a generalized concept of the genesis of oil shales indicates a process analogous to that which formed other sedimentary rocks. The following are the factors (Yen, 1976a) necessary for deposition and accumulation of organics and inorganics, which, under continued sedimentation and subsidence (involving pressure and temperature), results in a sedimentary rock with measureable amounts of organic residues: 1) abundant organic productivity, 2) early development of anaerobic conditions, and 3) lack of destructive organisms. In most instances, the oil shale formation initiated in some tranquil body (e.g., marine basin lake, or pond) where the above conditions predominated. The shale of the Green River Formation is of lacustrine origin, deposited principally from the large Eocene Lakes of the Eocene Age (400 million years ago). Other potential U.S. resources include the Jurassic and Triassic marine shales in Alaska, the Permian deposits of the Phosphoria Formation in Montana, the Devonian and Mississippian shales of central and eastern U.S., the Ordovician black shales in the Appalachian Basin, and the Nonesuch shale of Precambrian Age in Michigan and Wisconsin. On a worldwide basis, worthwhile deposits exist in Australia, China, several

areas in Russia, and Scotland.

The Green River Formation of Colorado, Utah, and Wyoming is believed to be the world's single largest hydrocarbon deposit (Obert, 1973). Of this reserve, 15% is recoverable by present technology with only about 1% projected for development before 1985.

The most economical yields from refining Green River shale oil are (Obert, 1973): 15-17% gasoline, 30-32% kerosene, 18-26% gas, 15-18% light lube oil, and 10-12% heavy oils and paraffin wax. The economic importance of oil shale and its potential reserve in comparison to other forms of energy currently being used (or planned) in the United States are shown in Table II. Large-scale commercial production of crude from oil shale is still nonexistent in our country; however, government sponsored minimal production by conventional techniques, and some relatively small-scale experimental procedures (e.g. by Occidental Corp.-McCarthy and Chan,1977), are presently in operation.

TABLE II

FUEL RESOURCES OF THE UNITED STATES (OBERT, 1973)

Fuel	Production (1972)	Energy Content	Estimated Total Economic Resource		
			Units Shown	Q(10^{18}BTU)	Equiv. 10^9bbl crude
Crude Oil (Conventional)	3.48×10^9 bbl	$5.8 \times 10^6 \frac{BTU}{bbl}$	250×10^9bbl	1.5	250
Coal	551×10^6 Ton	$24 \times 10^6 \frac{BTU}{Ton}$	1000×10^9Ton	24	3000
Natural Gas	$23.9 \times 10^{12} ft^3$	$1000 \frac{BTU}{ft^3}$	$1700 \times 10^{12} ft^3$	1.7	143
Shale Oil	-	$9 \times 10^6 \frac{BTU}{Ton}$	1300×10^9Ton	12	1000
Tar Sands	-	$5 \times 10^6 \frac{BTU}{Ton}$	100×10^9Ton	0.5	42

B. Resource Recovery Techniques and Analyses

1. Conventional Mining Techniques. The application of standard mining techniques, many of which include the convential operations of drilling, blasting, and muck haulage to surface retorts (and then to refineries), is well documented (e.g. Dravo Corporation, 1974). These extraction methods have problems representative of several types of resource recovery techniques, including coal mining and underground gasification, mineral extraction from ore bodies, and even secondary/tertiary oil removal from existing wells. The need for innovative designs in both machinery and mine layout to optimize mechanization and reduce expenses has been emphasized by Peterson (1977). However, the historically slow evolutionary pace of mining technology is not expected to meet the deadline of a slow-down in world oil production. A massive network of mine operations will be required to meet future U.S. needs, with each facility having the capacity to handle 85,000 tons of shale rock per day in order to produce an equivalent 50,000 barrels of crude oil (Cameron Engineers, 1975). No fewer than one hundred would be needed to relieve our daily imports, currently at 8.2 million barrels per day (James, 1979).

Many novel methods of rock excavation have been assessed (e.g. Cook and Harvey, 1973; Cunningham, 1977; Grantmyre and Hawkes, 1975), including hydraulic, mechanical, thermal,

and electromagnetic techniques. Their conclusions confirm a former belief by experts in the field that there is little chance of appreciable future improvements in rock penetration rates by drill and blast methods (a crucial factor in minimizing specific work). Because of the high degree of specialization already attributed to the drill and blast process, totally new extraction methods need to be conceived. This is further necessitated by the shale's high toughness and resistance to indentation (Hill, 1979).

2. Oil Shale Retorting. The destructive pyrolysis process (retorting) by which the organic matter (kerogen) is separated from the inorganic substance of the shale has been extensively examined (e.g. Carpenter and Sohms, 1974). Suffice it to say that when the rock is heated to temperatures of about 400°C (800°F) in an appropriate retort, components of fluid and vapor are liberated, collected, and then upgraded into a liquid roughly equivalent to a crude oil.

a. Ex Situ Recovery. The ex situ version of this process, in which shale rock is mined, crushed, and conveyed to a retorter on the surface, has been extensively studied. Recent large-scale*, continuous production processes employing various ex situ methods include the following

---

*Retorts holding upwards of 150 tons of shale rock.

(Hendrickson, 1974): 1) Union oil process, in which the necessary heat is provided by the combustion of coke inside the retort; the process is unusual in that the shale is fed in through the bottom and propelled to the top via a vacuum-type pumping system, 2) Cameron and Jones process (Petrosix), in which shale is fed through the top of the retort and heat is supplied solely from recycled gas, 3) TOSCO II process, where externally heated ceramic balls supply heat to crushed shale rock in a revolving drum structure, 4) NTU process (U.S. Bureau of Mines sponsored in 1940's -- forerunner of Garrett process; 1600°F heat is provided by air and recycled gas to the retort, and 5) Lurgi-Rohrges process, in which the retort temperature is supplied by solid material (e.g., sand) fed into the retort to continually mix with the crushed shale. In general, these processes are continuous in nature, and effectively extract roughly 75% of the trapped organic matter in the shale. The processes typically consume 15% of the potential energy of the syncrude; however, use of recycled gas and fluid from the system lowers the total energy consumption by, on the average, 25%.

Advantages of these ex situ methods include high recovery efficiency and the capability of adequate control of the process variables. Recovery efficiency

based on Fischer Assay* is high relative to present day *in situ* techniques; however, state-of-the art technology (Yen, 1976a) of the above processes yields at best only 80% organic material liberation, without extensive energy input. For good efficiency, the passage of air and product gases must be essentially homogeneous throughout the "process zone" in a retort. This can be accomplished in an *ex situ* retort process inasmuch as the engineer is able to monitor and control the temperature and shale flow in the retort.

A crucial limiting factor in any *ex situ* recovery process is the high cost of operation and labor necessitated by the mining, hauling, and retorting steps required. Initial capital costs for most mining operations run into the hundreds of millions of dollars (Cameron Engineers, 1975; Dravo Corporation, 1974); in cases of deep ore deposits, requiring special mining techniques (e.g. sublevel caving, open stopping), the return on investment is negligible for years. Presently, then, this limits operations to shale deposits lying near the surface (less than 2000 ft deep) where open pit or room and pillar mining can be exploited. Additionally, the retorting phase alone requires the input of energy equivalent to 12% of that extracted

*Laboratory procedure for retorting oil shale and assessing oil, water, gas, and mineral contents.

(Yen, 1976a).

Another constraint arises from the environmental impact on the area (e.g., spent shale disposal, pollution control, water supply). The disposal requirement for a typical five million bbl per day production capability is obviously of order 200,000 tons of shale rock per day*. Only 10% by weight of crushed shale is producible oil for a typical 25 gpt shale. Because of the short supply of water around the sources, and in view of recent government regulations on air and water quality standards, another major technical hurdle has yet to be crossed toward successful commercial shale oil exploitation by ex situ means.

3. Currently Proposed In Situ Recovery Processes. The attractiveness of an in situ oil extraction process is readily apparent, from both economical and ecological points of view. With minimal mining for ore access and excavation of passageways, spent shale disposal is decreased substantially. The consequencies of ground subsidence are likewise reduced. Also, oil recovery from deep deposits and extraction from leaner shales (less than 15 gpt) are now economically acceptable.

---

*Volume of spent shale is typically 15% greater than original shale rock volume, due to crushing and retorting (James, 1979).

However, maintenance of adequate process control, in particular for in situ retorting, is limited severely by the state of current technology. The establishment of the necessary homogeneous permeability for efficient fluid flow during the pyrolytic reaction is crucial in the retort zone. Much work has yet to be done in this respect to understand the essential features of deformation and fracture, particularly time and temperature dependence, under various ambient stress conditions. For instance, the openings in the retort area must be maintained for a smooth, continuous operation. Containment of the entire procedure, from initial shale access and bed preparation (e.g., Peterson, 1977; Schmidt, 1975) to retorting and shale oil extraction (e.g., Schmidt, 1975), also poses major technical problems. A more in-depth analysis of the primary technical difficulties to be encountered during in situ retorting is discussed in Section 1.4.

Included in the general category of currently proposed in situ production methodologies are the following: 1) subsurface chimney, 2) natural fractures, and 3) physical induction of fractures with no subsurface voids. The various processes categorized as subsurface chimney include: a nuclear chimney suggested by Phillips Petroleum (Parker, 1970); hot gas systems developed by Atlantic Richfield (Ellington, 1972), McDonnell Douglas (Busey, 1972), Continental Oil (Gilliland, 1969), and Mobil Oil

(Walton and Slusser, 1971); hot fluid systems developed by Shell Oil (Ueber, et al. 1974) and Garrett (Garrett, 1972); and a unique chemical extraction method proposed by Shell Oil (Herce, 1972). Perhaps the largest private endeavor to date which may be classified as a subsurface chimney was that developed by the Occidental Exploration and Production Company (McCarthy and Chan,1977). Based on the assumption that the major problem in performing underground oil shale retorting was in providing sufficient permeability for controlled gas flow, Occidental developed a modified in situ process. The process consisted of excavating 15 to 20 percent of the shale deposit under the retort zone, expanding (caving) the remaining shale into the void volume, and then retorting the rubblized oil shale in place.

Unmodified natural fracture processes for shale oil extraction include proposals by Shell Oil (Clossmann and Nordgren, 1968), Marathon Oil (Allred, 1974), and Resources R&D from South Africa (Felix et al., 1974). Alternately, a method employing a specialized leaching technique to enlarge the natural fractures was proposed by Shell Oil (Prats, 1967).

Lastly, a physical induction procedure for in situ recovery of shale oil and other minerals via borehole and usage of high-intensity laser beams was proposed by

Netherland's based Woods Research and Development (Purce, 1975). A somewhat similar induction method was proposed by Bridges, et al.,(1978). This method incorporated radio frequency dielectric heating, similar to the heating process which occurs in a microwave oven, to volumetrically heat oil shale in situ to pyrolysis temperatures. Work is still proceeding in this area.

It would be inappropriate at this time to state that one particular retort procedure, whether in situ, ex situ, or some combination of both, would be best for exploiting our oil shale reserves. The complexity of the issue cannot truly be resolved without further laboratory and field tests, some as yet to be devised. The point, however, is that a more intense investigation in this area should be undertaken immediately to help relieve U.S. dependency on foreign imports of crude oil. In an address* before Congress following the crisis of the 1973 Oil Embargo, a particular path was paved for future work in shale oil extraction. Scientists and engineers there concurred that "current thinking is that only an in situ retorting and extraction method will be practical for the future."

*Hearing before the subcommittee on Energy, 93rd Congress on H.R. 9693, "Oil Shale Technology," 1974.

Recent political developments (July, 1979), with resulting determination to stimulate synthetic fuel production, should help to establish a practical mode of shale oil exploitation.

4. In Situ Retorting and Recovery, Problem Definition.

In order to successfully exploit our huge oil shale reserves (perhaps also including tar sands), adequate knowledge must be obtained, through experimental and/or analytical investigation, in connection with several technical considerations. Foremost among these is sufficient process control: can the necessary permeability and communication in the formation be induced with minimal rock excavation? Can void volume be introduced by extraction of melted and diffusing kerogen, while it is reduced by thermal expansion of the matrix material during the pyrolytic reaction? It has been suggested (e.g., Panel on Rock Mech. - U.S. Nat. Comm. for Rock Mech., 1978) that in situ recovery is strongly dependent on the establishment of homogeneous prosity/permeability in the producing zones. In fact, many conclude that this homogeneity is an absolute requirement for both economical and technical feasibility. High recovery efficiency is very crucial in an in situ process (Fenix and Scisson, 1975). Satisfactory means of consistently obtaining this efficiency under various operating conditions must be

determined.

Another technical difficulty worthy of intense study in an in situ process is that of containment both during preparation for access to the zone, and during production. The effects of crack blunting or retardation at different interfaces, and branching of fractures to more favorable orientations due to a mixed-mode stress field must be more rigorously understood (Cleary, 1978d). Containment within the designated process zone is vital for high recovery efficiency and for prevention of shale oil loss or contamination (e.g., of water supply) in surrounding strata. An understanding of bulk material response, dependence on time and temperature etc., is particularly pertinent during the production (retorting) stage. Research in this area has thus far been relatively limited (e.g., McCarthy and Chan,1977).

a. Need for Constitutive Model. Form the preceding enumeration of problems, it is evident that a need exists for the development of an experimental and analytical basis for understanding and predicting the deformation and fracture behavior of oil shale. This basis would incorporate static and dynamic constitutive relations, fracture behavior, and heat and mass transfer characteristics (e.g., conductivity, permeability), over relevant ranges of the following parameters: 1) organic

content, 2) temperature, 3) in situ stress state, and 4) environment (e.g., corrosive fluids). Structural configurations of most interest include crack tip environments in various geometries and, in particular, the response around cavities or inclusions of all shapes; boundary conditions may be imposed on stress or displacement, temperature or heat flow, and pore pressure or mass flow.

The characteristics required for realistic and analytically useful constitutive relations* for oil shale include: physically-motivated macroscopic transverse isotropy in the initial state; nonlinearity, including dilational effects and hysteresis in load/unload cycles (e.g., see Jaegar and Cook, 1975); rate-dependency; thermal response; and various environmental effects. These relations are extremely important in understanding the fundamental mechanical principles used to assess the features of various extraction schemes. Ideally we might hope that an adequate assessment could be made by using laboratory experiments on representative specimens obtained from the field site. The economic benefits of these less expensive laboratory tests, which may lend themselves to effective theoretical analyses, must be carefully weighed against more expensive, but perhaps more

*The particular constitutive relation employed in this thesis is presented in Appendix VII.

technically-accurate, large-scale field tests.

b. Procedures Needing Examination Toward Optimizing Access, Fracturing and Retorting in Situ. The initial step toward an in situ retorting scheme involves an in-depth underground mapping of the shale deposit, including any relevant geological features (e.g., primary faults, discontinuities, other mineral, fluid or gas pockets) which may influence the overall procedure. A complete description of the surrounding strata, with information on structure, aquifers, and the like, is crucial particularly for containment purposes. The technical means of outlining the shale deposit and the zone designated for in situ production is available (Einstein and Alva-Hurtado, 1975; Fenix and Scisson, 1975). However, a more exact ermination of the rock's bedding planes, which result regional anisotropies in material moduli and strength, ; required. This is especially important in process :one preparation, during which crack propagation, branching, arresting, and blunting at different bed boundaries may occur. The extent to which topology and ambient conditions can be determined from cores and measurements taken in boreholes, an important economic factor, has yet to be resolved completely.

Efficient access to and preparation of the retort zone also requires an accurate measurement of the pre-existing tectonic stress state. Cleary (1978d) has postulated that this initial stress state has the greatest potential for dictating evolution of fracture shapes. Fracture behavior is an important component of bed preparation -- whether performed by large-scale detonation (Reed and Boade, 1977) or hydraulic fracturing (e.g., Schmidt, 1975). Large principal stress differences which lead to consistent fracture growth orientations must be determined and exploited appropriately. Because most of the Green River shale deposits exist in upper strata (Cameron Engineers, 1975), high lateral stresses are generally improbable. This condition will, for instance, allow biased crack growth toward the divider orientation (discussed later). Present state-of-the-art technology (e.g., Parker, 1968 ; Einstein and Alva-Hurtado, 1975) is insufficient in reaching the degree of sophistication needed in this respect. Information on local stress state conditions is ideally required continuously: this might be done by positioning the necessary equipment in strategic locations throughout the retort zone (for instance, in the boreholes used for initial access to the shale and primary bedding plane determinations).

Thirdly, the ability to map fracture patterns, in both direction and length, must be developed to a much greater sophistication. This achievement is vital, not only for projecting the homogeneity of the fracture pattern in the retort area (an important factor for high recovery efficiency, as stated previously), but also in verifying the possibility of secondary cracking due to thermal effects or pore fluid diffusion during the retort phase. Since these secondary cracks are likely to be an order of magnitude or more smaller than the initial preparatory fractures, this ability must be improved to a very high degree of sophistication. Greenfield, et al., (1977) has experimented with electrical monitoring but the complexity of the strata and surrounding wellborne conditions led them to suggest refined measurement systems, data reduction, and analysis techniques. More complex models are needed to account for the multitude of effects. They likewise advocated dynamic, continuous monitoring of voltage changes before, during, and after fracturing operations. This should improve the accuracy and resolution of the pattern by decreasing background interference. Other mapping techniques are referred to in (Cleary, 1978c).

Another procedure requiring more in-depth analysis is that of bed preparation. An effective, and highly efficient means of establishing the necessary permeability

throughout the retort zone for continuous fluid and gas flow, while maintaining good process control and production containment, has yet to be devised. Proposed techniques include sub-level caving or open stopping (Dravo Corporation, 1974), explosive means (Reed and Boade, 1977) and other aforementioned methods. For purposes of this paper, though, retort zone preparation by hydraulic fracturing will be most intimately discussed. This writer agrees with the contention of Cleary (priv., comm., 1977-78) that any future commercial exploitation of the oil shale reserves can greatly benefit from proper implementation of hydraulic fracturing (either alone or in conjunction with other access techniques) for efficient bed preparation.

c. Relevant Mechanics of Fracturing and Retorting. An essential feature of underground fracturing relevant to efficient bed preparation for retorting is the ability to propagate cracks in preferential directions with suitable spacing. This is important, not only for homogeneous dispersion of accessways throughout the process zone (as needed for successful retorting), but also for containing the process components and retort products so that efficient extraction can be achieved throughout the zone. The fracturing appears strongly dependent on the local

pre-existing stress state, material anisotropies, and other inhomogeneities (Cleary, 1978d). Additionally, the extent to which the method of fracture generation affects fracture geometry should be more carefully examined. Maintenance of these fracture channels during retorting is also a critical feature of good process control.

Another feature of hydraulic fracturing which pertains to bed preparation is that of crack growth in media having creep characteristics and second-phase diffusion. Considerations of influences due to "drained" and "undrained" bulk responses, and creep crack growth (e.g., Knauss, 1976) are obviously important. Cleary (1978d) has postulated that the energy to induce crack growth in fluid-soaked media increases appreciably with crack speed times the ratio of crack length over diffusivity. Creep effects might also increase the fracture toughness of the shale by introducing plastic deformation around the crack tip which would effectively shield the near-tip process zone from any remotely-applied stresses.

Better understanding is also required in relation to interface effects on fractures generated during access operations. Toward the all-important achievement of containment, crack blunting, arresting, branching, or reinitiation in surrounding strata must be examined under various stress state conditions (Cleary, 1978d): barriers to crack propagation into surrounding strata

(e.g., due to contrasts in toughness or elastic moduli and blunting), should be further explored. For example, weak-bonding state that exists between the shale zone and an adjacent stratum significantly lowers the probability of crack reinitiation in that stratum, thus resulting in the blunting of the fracture. If the capability for determining or achieving this condition beforehand is developed, it could then be exploited beneficially for containment purposes.

A final step towards optimization, particularly of the retorting state of the in situ extraction process, involves a thorough understanding of the thermomechanical and thermophysical response of oil shale. Determination of the shale's response to the high temperature and varying stress conditions, to which it will be subjected during retorting, will aid considerably in overall process control. It is important to assess the effects of kerogen (liquid and vapor) diffusion in situ and the role of secondary thermal cracking in preserving the necessary permeability as the retort or "burn" front propagates through the zone. Determination of the temperature at which measurable thermal cracking appears, under sundry confining stresses, will assist in optimizing the energy input into the system. Tertiary thermal cracking should provide additional aid both in reducing the average particle size of the rubble

(e.g., as a clogging deterrent) and in the efficacious distribution of void space throughout the process area.

Because of the anisotropic and inhomogeneous characteristics of oil shale, the thermomechanical response to time and temperature effects is assuredly very complex. These characteristics originate from (e.g., Jaegar and Cook, 1975): 1) the non-random distribution of constituents and microcracks in the rock, 2) a preferred orientation of minerals with different properties or anisotropic crystal structures ("rock fabric"), and 3) stress-induced microcracking in preferential directions during loading (e.g., Brace, 1971).

A detailed analysis of the chemical characteristics of kerogen upon thermal decomposition, as was briefly mentioned earlier in this section, is important for several reasons (Yen, 1976b). Firstly, identification of product recovery is essential from an economic point of view. Not only can crude oil be extracted via the <u>in situ</u> process, but other minerals of value (e.g., aluminum, magnesium, copper, lead), which may be trapped in the sedimentary rock, may also be exploited. Secondly, the chemical analysis of kerogen should assist in preserving the structural integrity of the process zone during the production stage. Knowledge of shale response following kerogen removal is important to maintain accessways and flow channels by preventing any clogging resulting from

residue deposition.

Finally, an understanding is required of the components of decomposed kerogen toward prevention of possible underground contamination and toward an adequate evaluation of the syncrude to determine the extent of initial processing (before transporting to refinery). Should containment of the process area be lost for some reason during retorting of the shale, an accurate assessment must be made to determine the adverse effects (if any) to the surround strata.

For instance, decomposition of kerogen has shown it to contain traces of uranium, iron, vanadium, nickel and molybdenum (Yen, 1976a): combination of these elements with the noble metals produce carcinogens. Additionally, retorting of oil shale has been shown (Obert, 1973) to produce toxic hydrocarbon, nitric oxide, and carbon monoxide emissions. These potential by-products of in situ retorting could result in dire environmental consequences should they leak into the underground water systems or be inadvertently dispersed into the air.

Thus, the work presented here is a first step towards understanding the complex thermomechanical response of oil shale. The primary thrust is towards experimental tests and analyses: however, we give a more detailed treatment of the constitutive relation introduced by Cleary (1978b), accounting for temperature effects. Furthermore, we performed uniaxial tests at $\theta = \pi/4$ to the bedding planes,

and also some triaxial experiments, to determine more of the coefficients in the relation. An analysis is developed of some observed regimes of interest of shale response at various temperatures. Tests and discussions are given for more fracture toughness measurements to include thermal and confining stress effects.

An overall qualitative analysis is presented of the oil shale's reaction to a multitude of interesting parameters during the preparatory stages of the experiments (e.g., heating, cooling, cutting, grinding, coring, epoxying). Further experimental and analytical tests needed for the possible solution of an in situ process and a feasibility study for future developments of this procedure are then detailed in the conclusion of the thesis.

II. EXPERIMENTAL PROCEDURE

A. Specimen and Equipment Preparation

The majority of the specimens were obtained from a single, large block of oil shale (about 150 kilograms) received from the Paraho Anvil Points Mine*. Many smaller pieces (less than 10 kilograms) were also received, but they were primarily used in initial characterization tests. The large shale block was noticeably darker in color than those used by Hangen (1977); however, Fischer Assay** of two representative pieces from opposite ends of the block revealed a lower organic content (Table III). This casts suspicion on visible determination of approximate kerogen content. The difference in organic content from one side of the block to the other (block length of order 1 meter) is clearly evident. A more localized description of process areas may be needed for some purposes, such as structural analysis. A particular density correlation with organic content (Smith, 1969) was obeyed very closely by our assay results: a representative piece of shale, with a calculated density of 2.157 g/cm^3 should, as empirically derived by

---

*Courtesy of Mr. Earl Mast of Development Engineering, Inc.

**Fischer Assay performed by National Resources Laboratory, Inc.

TABLE III

RESULTS OF FISCHER ASSAY

Sample	Density g/cm^3	Oil gpt(wgt%)	H_2O gpt(wgt%)	% Spent Shale	% Gas +Loss
A	2.179	26.5(10.1)	3.9(1.6)	86.4	1.9
B	2.145	34.4(13.1)	1.8(0.5)	83.8	2.6

Smith (1969), contain 29.1 gpt organic material. This value falls almost midway between the assayed samples (Table III).

The large shale block was rough-cut into manageable slabs by a 6-inch water-cooled diamond saw and then further refined into appropriate blocks for later use. Cylindrical specimens 2.7 cm and 3.8 cm in diameter were cored out of suitably-oriented blocks yielding cores with axes parallel, perpendicular, and 45° to the bedding planes. Core lengths varied because of pre-existing cracks in the blocks, but nominal lengths of 10 cm and 8.9 cm were obtained for tension and compression tests respectively. Cores to be used for a particular type of test (e.g. compression) were all cut from the same block to avoid possible discrepancies in organic content. The ends of the cores designated for uni-axial tension experiments were then faced off on a lathe and drilled with a 1.25 cm diamond corer. Aluminum end pieces

were epoxied to them with a high-temperature, high-strength epoxy. The outside diameter of each was then machined down to a nominal 2.54 cm, with the ends threaded for the specific tensile use.

The ends of the cores designated for uniaxial compression were ground to a smooth finish, and afterwards were found to be parallel to within angles of 2'. No other preparation was required since the diamond corer and drill press used to core out the specimen left the sides perfectly smooth and round. Compression tests were performed without aluminum ends (direct platen loading). Triaxial cores were prepared in a manner similar to those for compression except that some early specimens of nominal 1.7 cm diameter and 3.3 cm length were cut. This size was required by the testing apparatus; however, cores of much greater size (maximum 14 cm diameter by 19 cm length) will be used for testing in a new triaxial cell.

Fracture toughness specimens (compact-tension geometry - discussed later) were sliced from a previously prepared block to a nominal thickness of 2.54 cm, with the water-cooled diamond saw. The perimeters were then more finely cut with the diamond saw to a nominal 12 cm square. Pin holes of 1.3 cm diameter were then cut with a diamond corer, eliminating the chip breakoff problem discussed by Hangen (1977). Finally, the notch required was cut

by a smaller 5 cm diameter saw.

The rock's affinity to oils and grease was readily observable. It was found during the testing, though, that moisture had a negligible effect on shale properties. Cracking due to drying out of the shale was not detected until the end of the testing, about one year after storage.

All of the high temperature experiments were performed in an environmental chamber. Strain gages were applied shortly before testing, and were used to 121°C (250°F). Above that temperature, an extensometer was employed to measure specimen strain. The prepared cores, with gages, were placed in the environmental chamber, heated to temperature, and then allowed to stabilize for one hour. A more detailed discussion of specimen preparation and equipment is given in Appendix I.

1. <u>High Temperature Uniaxial Tension Testing</u>. Tensile tests were performed in the three relevant orientations (parallel, perpendicular, and at 45° to bedding), up to temperatures of 149°C (300°F). The experiments were done using the equipment developed by Wilkening (1976), which is extensively detailed by Hangen (1977). Strain gages, employed to measure longitudinal and transverse deformations, were applied just prior to specimen insertion into the temperature chamber. Further details can be found in Appendix II. The equipment used for multiple strain

measurements and load application, with sensitivities of about 5 με and 14 Pa (2 psi) respectively, are discussed in Appendix III.

2. High Temperature Uniaxial Compression Testing. A compression cage was designed and constructed for use inside the Instron environmental chamber. Tests were performed using direct platen loading, at temperatures up to 204°C (400°F); again strain gages were used to measure the relevant strains, but above 121°C (250°F), an extensometer was used with the capability of measuring the much larger strains. Tests were performed to failure in both principal directions and at 45° to bedding. Details are given in Appendix IV.

3. High Temperature Fracture Toughness Testing. The nominal 30 gpt shale was additionally tested by using compact-tension fracture specimens. Experiments were conducted in each of the three distinct orientations available for a transversely isotropic material -- divider, arrester, and short transverse (see Figure 1). Specimens were sliced from the previously prepared parallelipiped blocks. The limited availability of material from the master block restricted the number of tests to one or two per orientation per temperature selected. The load-point displacements were measured differentially with a twin

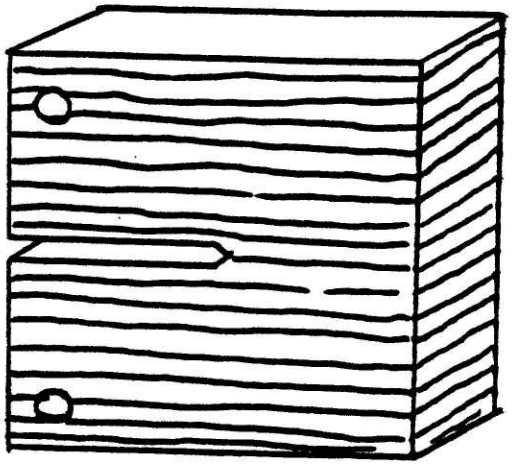

SHORT TRANSVERSE

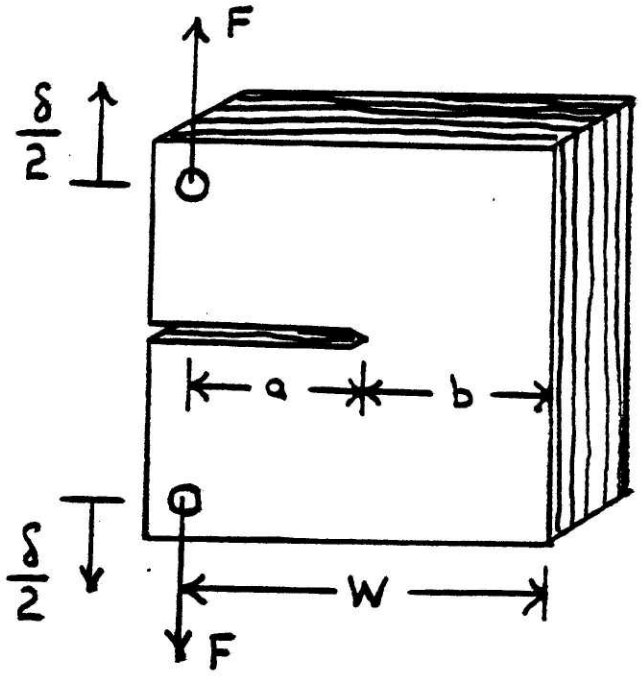

DIVIDER

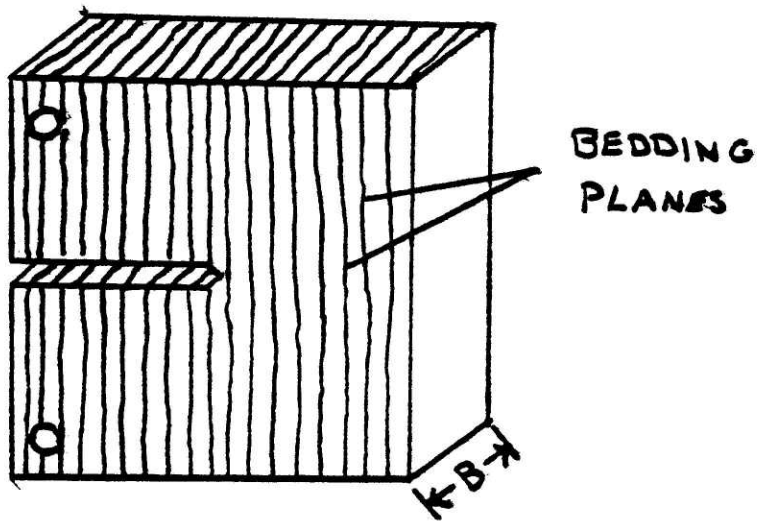

ARRESTER

Figure 1: Diagram of crack geometires for transversely isotropic oil shale

LVDT device (Wilkening, 1976).

To avoid branching into favorable bedding planes, a nominal 1.5 MPa (200 psi) confining stress was applied to some of the arrester specimens; this was done with small vice-like compression gigs which encompassed the samples. These tests were meant to simulate fracture response in the presence of overburden pressure. After preparation, the tests were again allowed to stabilize at temperature for one hour. Consult Appendix V for additional details.

4. Triaxial Testing. A series of experiments were performed at room temperature, using a very rigid, displacement-controlled triaxial machine*. Specimen size was dictated to be a nominal 1.9 cm diameter and 3.3 cm length, due to internal dimensions of the triaxial chamber. The samples were wrapped, prior to testing, with an impermeable plastic jacket. Longitudinal strain was measured outside the pressurized chamber with an LVDT arrangement. Confining pressure was induced with a petroleum ether. The tests were conducted over a confining stress range from atmospheric to 69 MPa (10,000 psi). Further specimen and equipment preparation details are to be found in Appendix VI.

*Courtesy of Dr. William Brace and associates in the Earth and Planetary Sciences Department.

5. Uniaxial and Fracture Toughness Testing of a Reservoir Sandstone. Similar tensile, compressive, and compact tension toughness tests were performed on a Kirkwood sandstone*, mostly to provide a comparison. The original disc-like shape, of the sandstone core slices, decreased the maximum size of suitable specimens to about 2.5 cm diameter, for a 7.5 cm maximum length, in both tension and compression; slabs of 2.5 cm x 10 cm x 8.8 cm could be obtained for fracture toughness tests. Although more abrasive and less machineable than the shale, identical preparatory techniques were employed. All tests were done at room temperature and made use of the same equipment (e.g., Appendices I, II, III)..

6. High Temperature Strain Gage Application. A modified technique was developed and used to strain gage application up to temperatures of 121°C, on the uniaxial test specimens. To determine thermal effects for the gages and epoxy alone, a gage was mounted on a bar of low carbon steel which was then heated to, and held at, the temperatures used throughout the actual tests. The residual thermal strains on the strain gage and epoxy were recorded and later subtracted from actual test re-

*Obtained from Marathon Oil Company, in connection with a tertiary recovery project in the Kirkwood Reservoir sands of Illinois.

sults. A further correction factor was measured to account for thermal expansion of a typical shale core. Thus, the resulting stress-strain curves to be presented closely represent a purely mechanical response of the shale. Details are given in Apendix III.

Kerogen pyrolysis was noted to have a negligible effect on the strain gage adhesive. No gage slippage was detected to 121°C. The temperature limitation of the strain gages and epoxy prevented their usage above 121°C. Measurement of transverse strains above this temperature will require special gages and adhesives, or a new method; this is being pursued in ongoing work.

III. EXPERIMENTAL RESULTS AND DISCUSSION

A. High Temperature Uniaxial Tension Tests

Results for tensile tests perpendicular to the bedding planes showing longitudinal and transverse strains are presented in Figures 2(a,b). Within the accuracy of equipment sensitivity, deviation from linearity was observed to begin at stress levels well below peak stress, ranging from 1 MPa (145 psi) at 21°C to less than .05 MPa (7 psi) at 149°C. Somewhat less scatter in response appears to be present at higher temperatures. This may be attributable to the relative importance of pre-existing cracks, and perhaps to the consequences of placing a strain gage inadvertently over one of them. At higher temperatures, shale response is much more compliant - particularly so in this orientation. The importance of pre-existing cracks is therefore offset by this increasing compliance and the general softening of the oil shale especially along bedding planes. Initial tensile moduli ranged from between 7.9 GPa (1.1×10^6 psi) and 8.7 GPa (1.3×10^6 psi) at 21°C to between 0.82 GPa (1.1×10^5 psi) and 0.85 GPa (1.2×10^5 psi) at 121°C.

Failure strengths and strains, both measured at peak stress, showed moderate scatter at all temperatures. A six-fold decrease in strength and roughly a four-fold increase in strain were measured from ambient to 149°C. Table IV can be

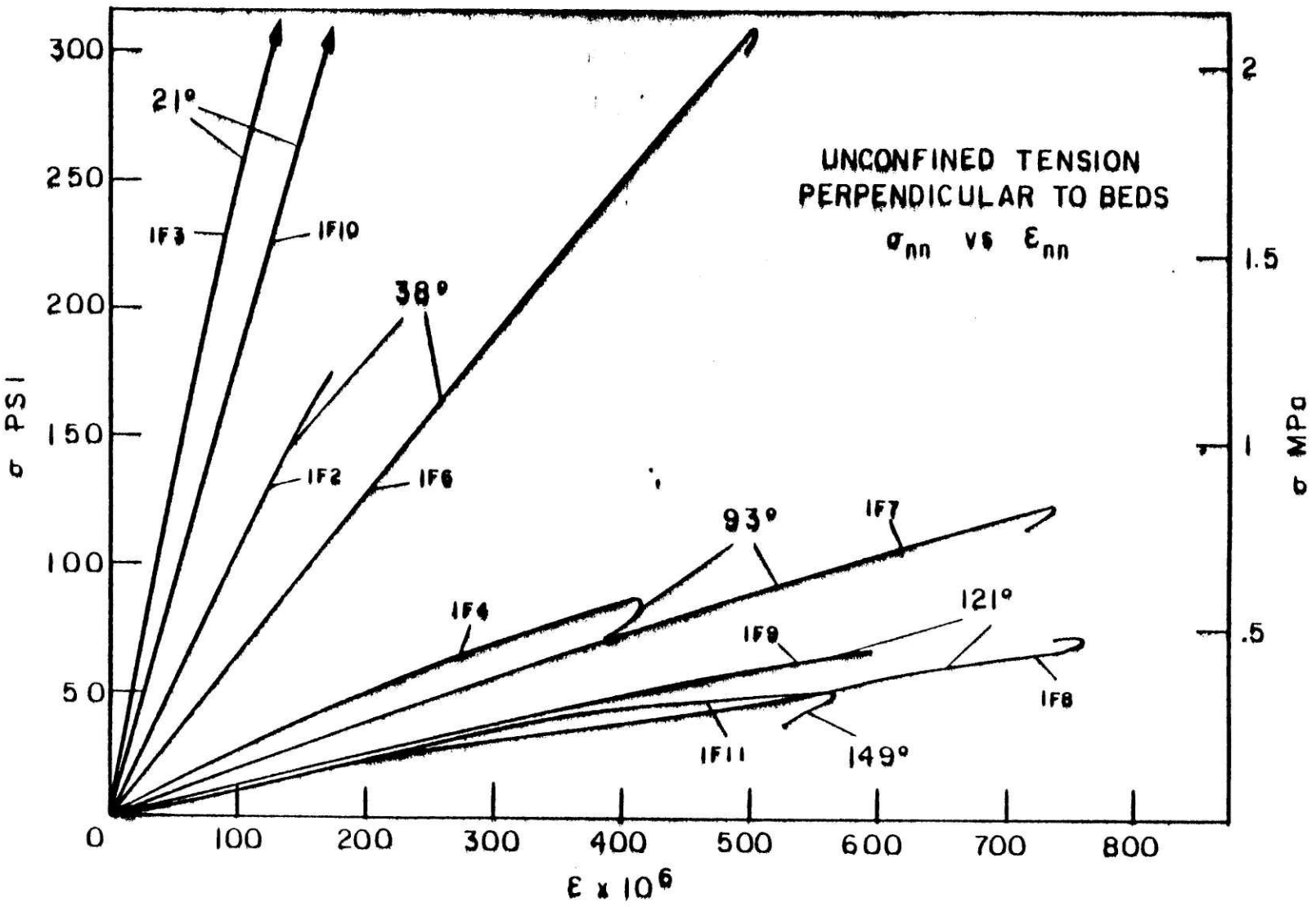

Figure 2a: Axial stress vs. axial strain for unconfined tension perpendicular to bedding for nominal 30 gpt shale.

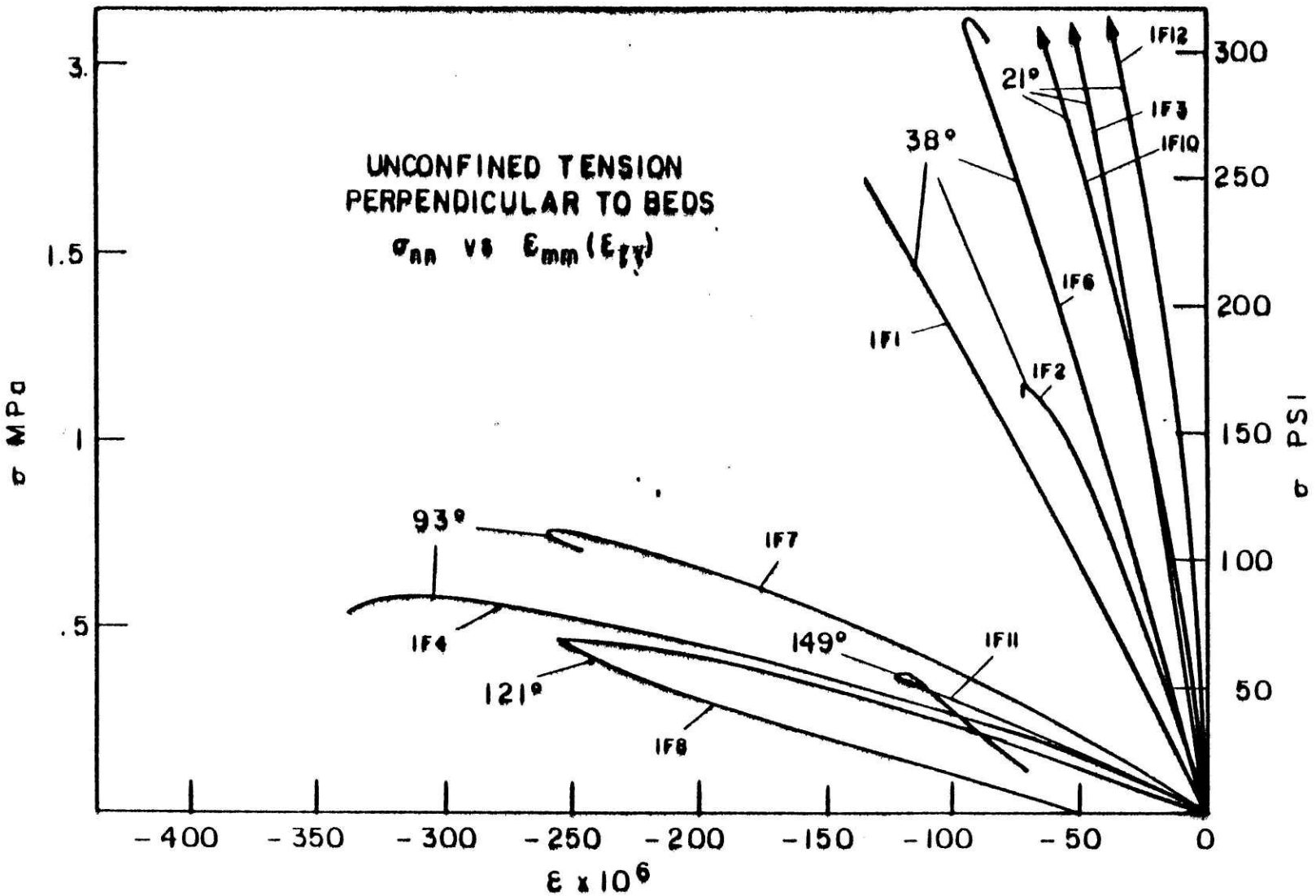

Figure 2b: Axial stress vs. transverse strain for unconfined tension perpendicular to bedding for nominal 30 gpt shale.

consulted for more specific results.

The stress-strain curves for longitudinal and transverse strains, for tension parallel to bedding, are shown in Figures 3(a,b,c). Predictably, nonlinearity did not occur in this orientation until higher stress levels were reached, by comparison with tests normal to bedding. Nonlinear response began around 2 MPa (300 psi) at 21°C; a lower "yield stress" was found at higher temperatures, e.g. about 0.5 MPa (70 psi) at 93°C, because of increased inelastic straining. Testing in this orientation initially produced failures through the epoxy layers, especially at the higher temperatures, but a revised epoxying technique corrected this problem (Appendix I). The small deviation from linearity at temperatures up to 38°C suggests limited crack growth prior to failure. However, at higher temperatures, fracture occurs much more slowly, resulting in more nonlinearity in the curves. This is discussed further under section III.A.2 dealing with failure mechanisms. Initial tangent moduli for tests parallel to the bedding planes varied from between 10.2 GPa (1.5×10^6 psi) and 17.4 GPa (2.5×10^6 psi) at 21°C to between 1.2 GPa (1.7×10^5 psi) and 1.7 GPa (2.5×10^5 psi) at 93°C.

Maximum strengths of 7.6 MPa (1100 psi) were recorded in this orientation at room temperature. At 93°C, average strengths had decreased to 2.2 MPa (325 psi). The scatter in failure strengths was minimal at all temperatures (with

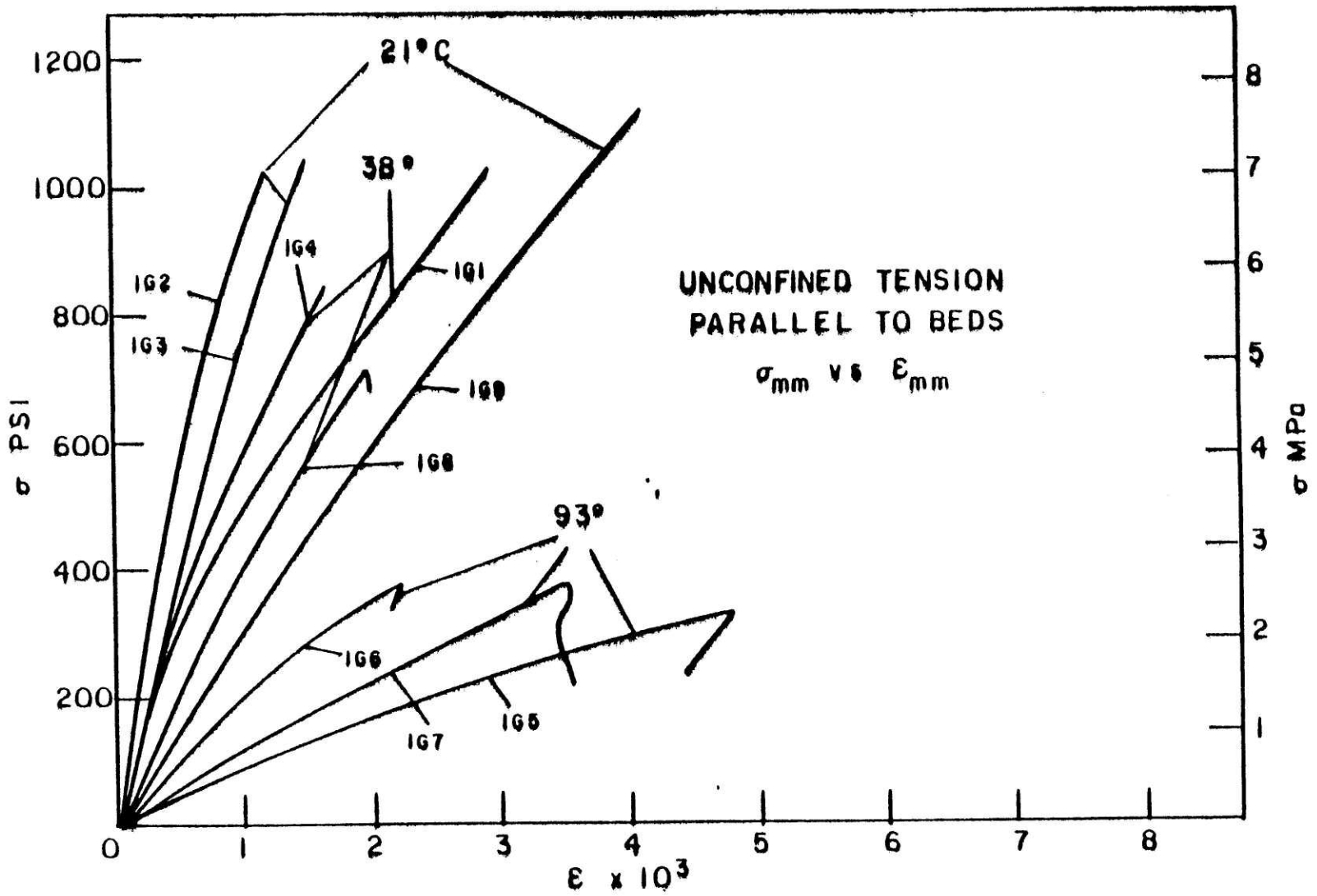

Figure 3a: Axial stress vs. axial strain for unconfined tension parallel to bedding for nominal 30 gpt shale.

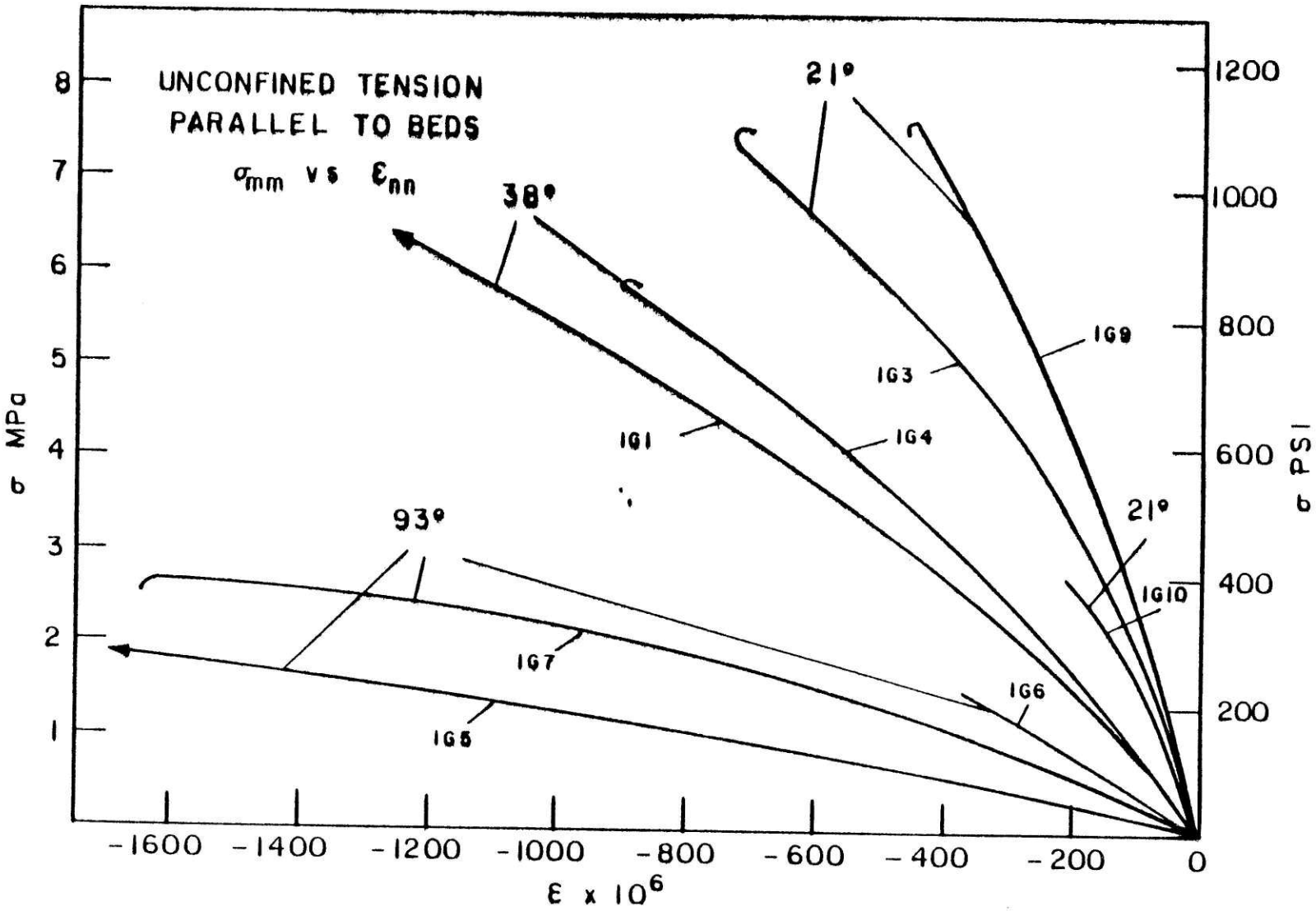

Figure 3b: Axial stress vs. transverse strain for unconfined tension parallel to bedding for nominal 30 gpt shale. Transverse strain measured normal to bedding.

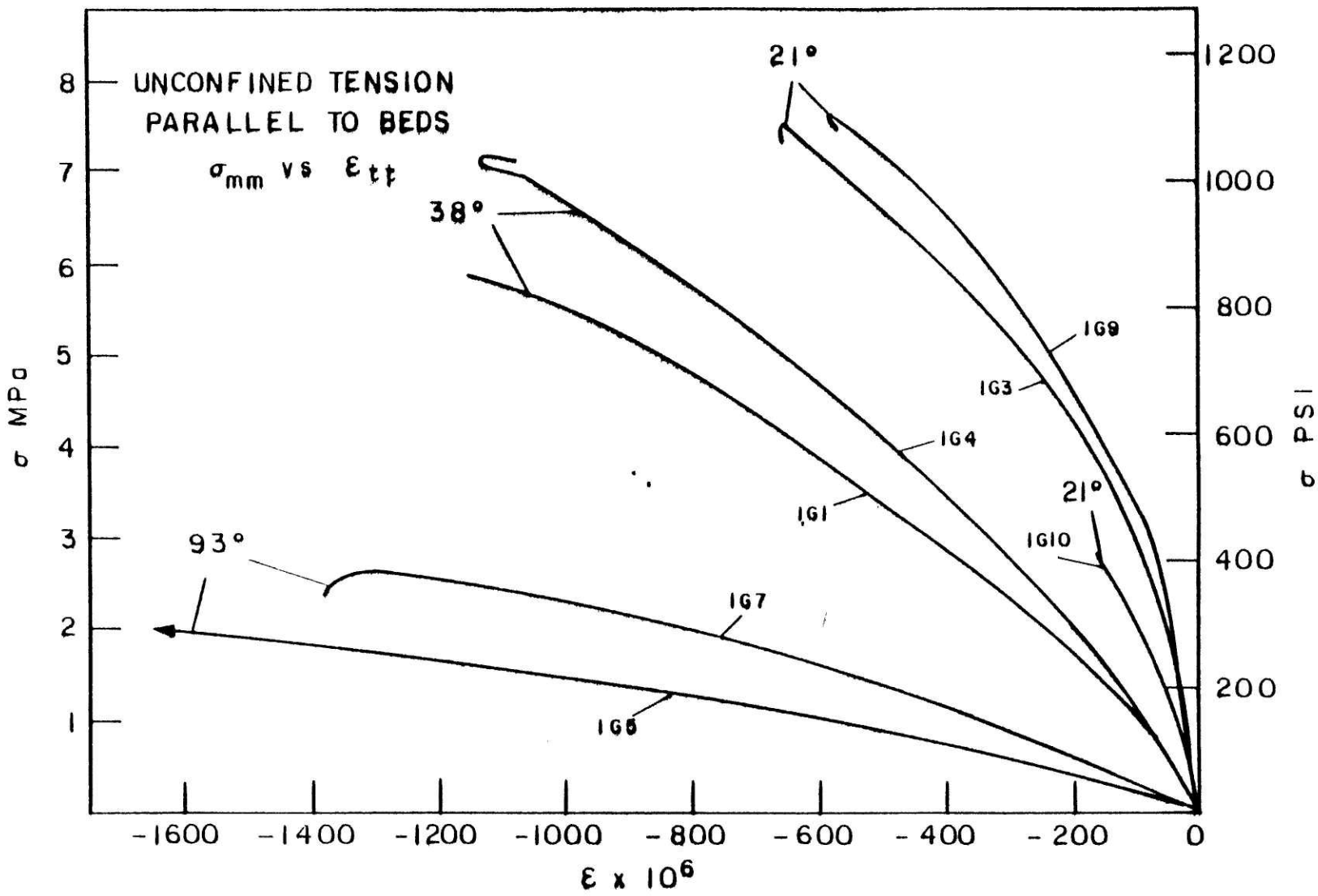

Figure 3c: Axial stress vs. transverse strain for unconfined tension parallel to bedding for nominal 30 gpt shale. Transverse strain measured parallel to bedding.

calculated standard deviations less than 5% of mean values in all cases. Failure strains showed a four-fold increase over this temperature range. Some tests were also performed on specimens that were machined down to a dogbone shape. It was concluded that the additional time needed to prepare the samples was unrewarding since differences in tests results were observed to be within the scatter band.

Tensile testing was also conducted on oil shale specimens cored at an angle of $\pi/4$ with respect to the bedding planes. Those tests provided data for determining the shear modulus G_{mn} out of the-plane of symmetry (e.g. Hearmon, 1961); they also gave additional information for specifying some of the remaining coefficients in the constitutive model (Appendix VII). New principal directions (for reference) are illustrated in Figure 4. Plots of longitudinal and transverse strains versus axial stress are presented in Figs. 5(a,b,c).

Although the results for normal strains might have been anticipated to lie midway between those tests parallel and normal to the bedding planes (viz. as to initial tangent moduli, Poisson ratios, strengths, etc.), a close correlation was actually found with data in the parallel orientation (Fig. 3). A five-fold decrease in

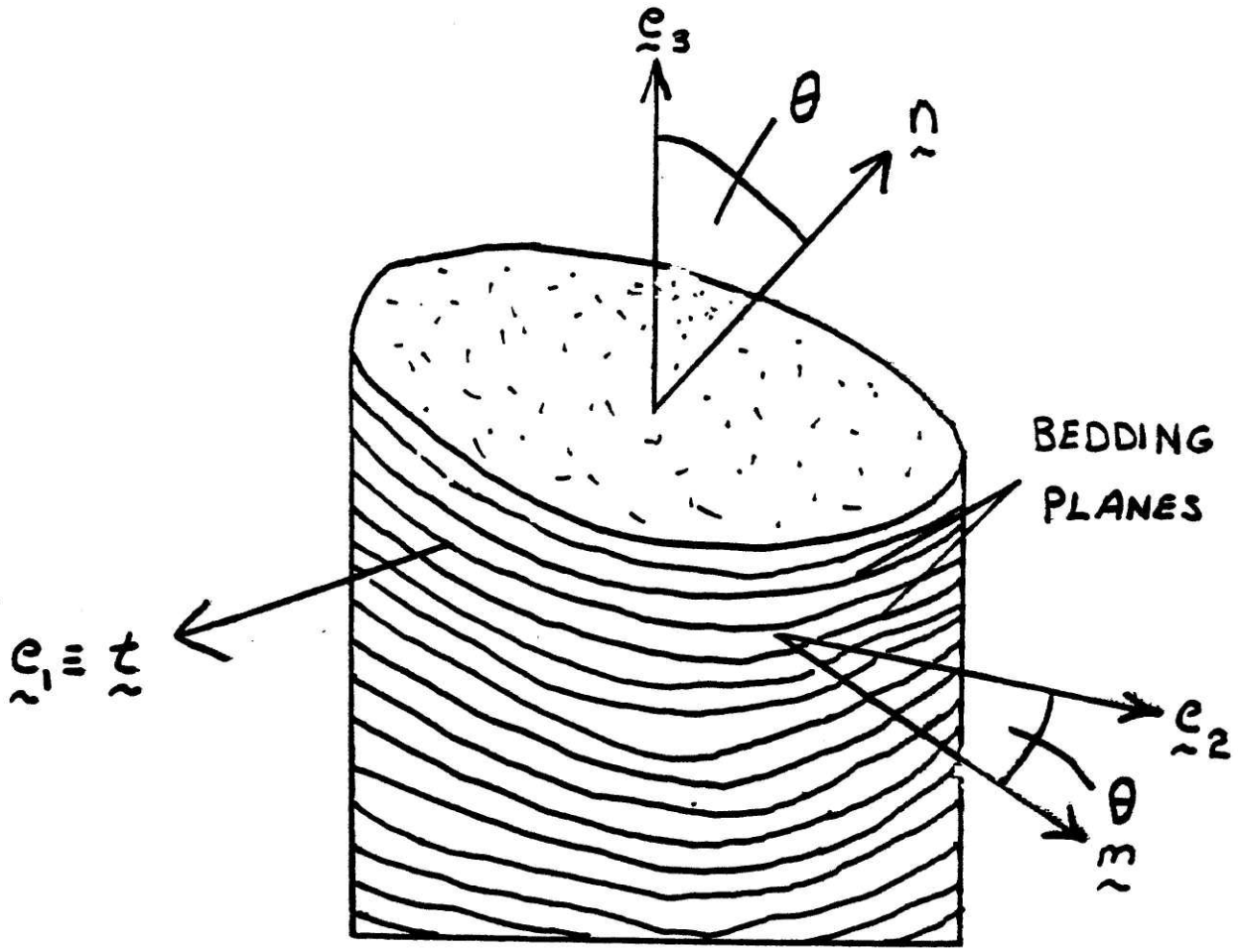

Figure 4: New direction vectors for specimens tested at angle θ to the normal vector. Direction e_1 is arbitrarily chosen to coincide with the original t direction.

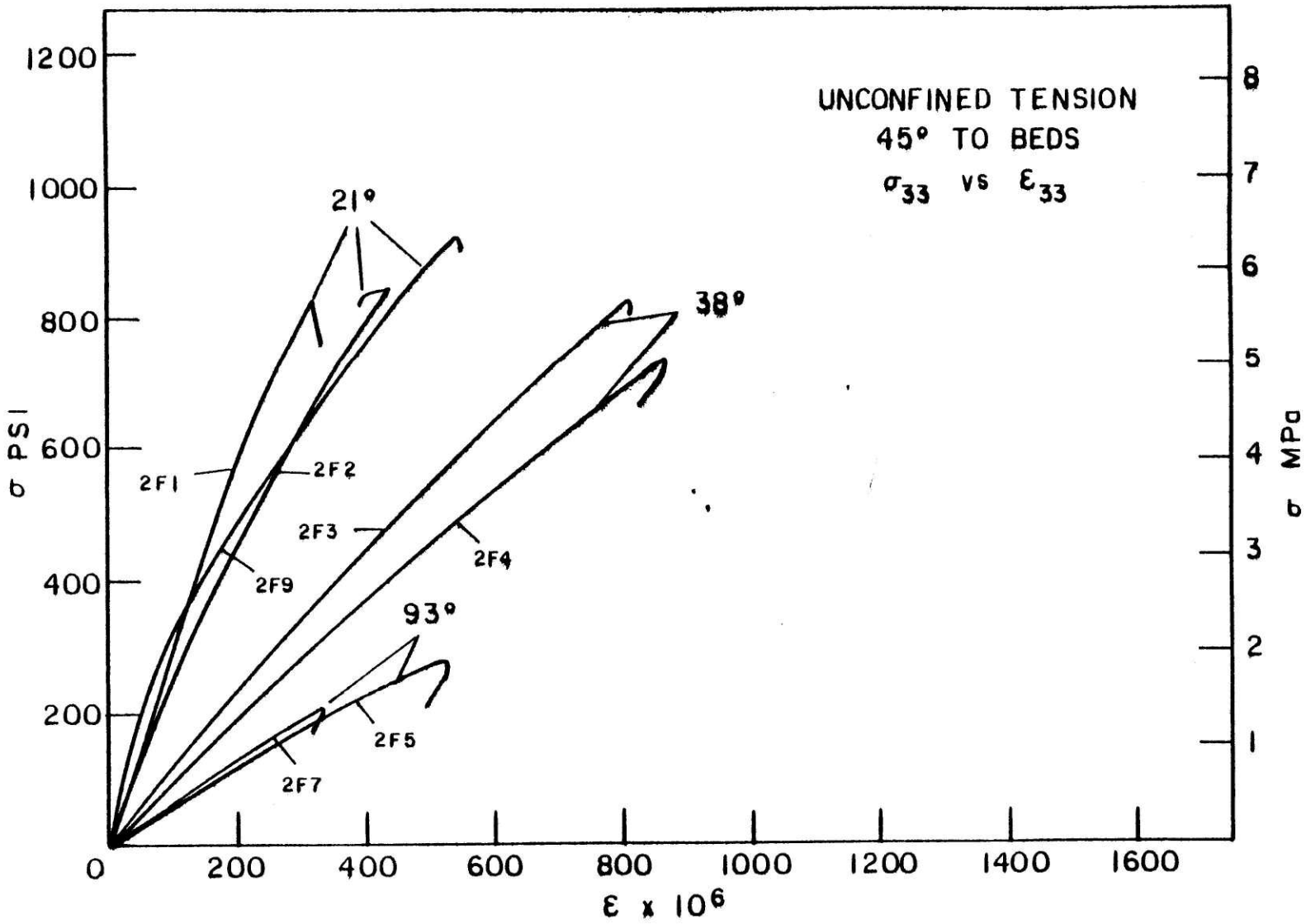

Figure 5a; Axial stress vs. axial strain for unconfined tension 45° to bedding for nominal 30 gpt shale.

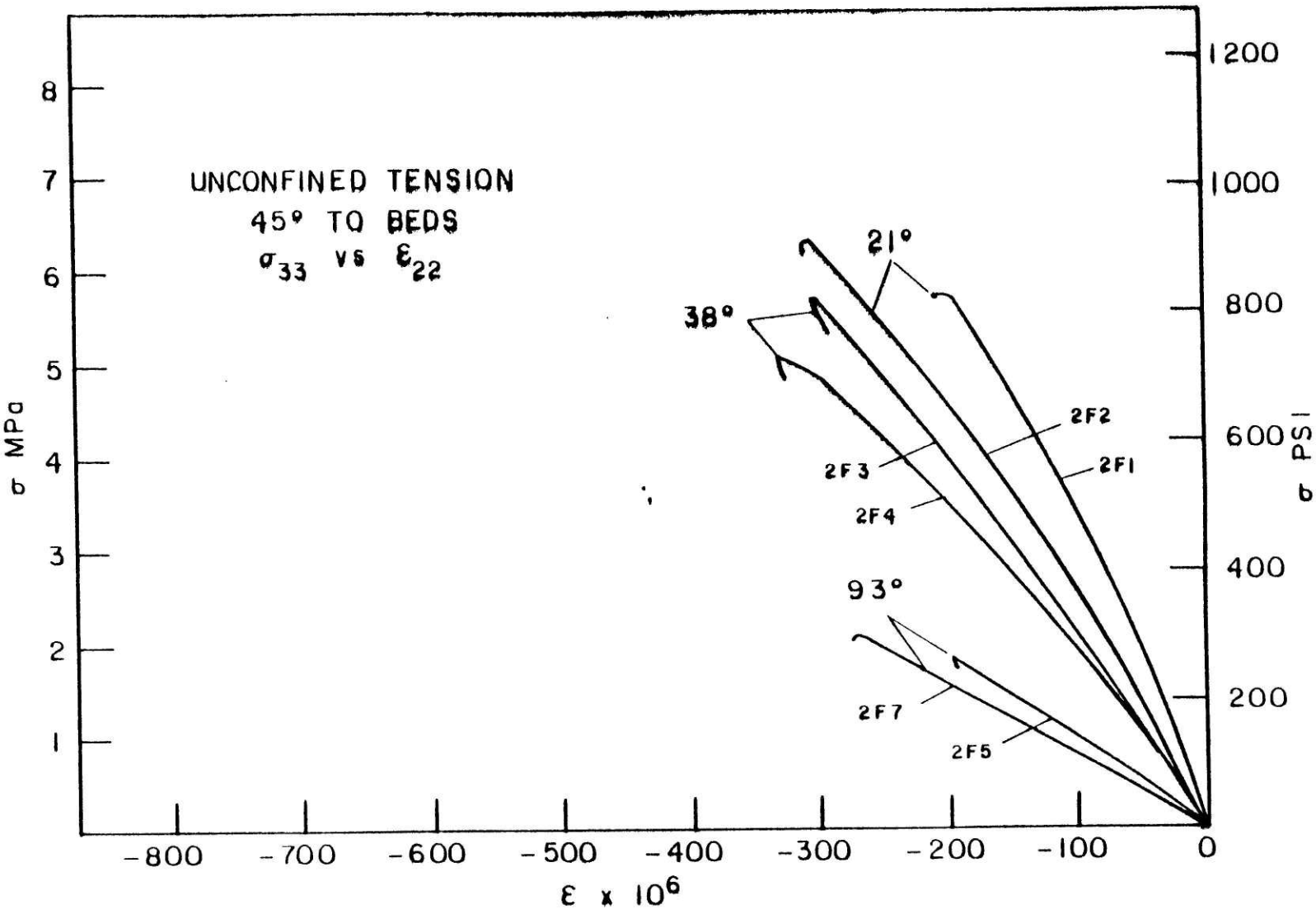

Figure 5b: Axial stress vs. transverse strain for unconfined tension 45° to bedding for nominal 30 gpt shale. Transverse strain measured in $\underset{\sim}{e}_2$ direction.

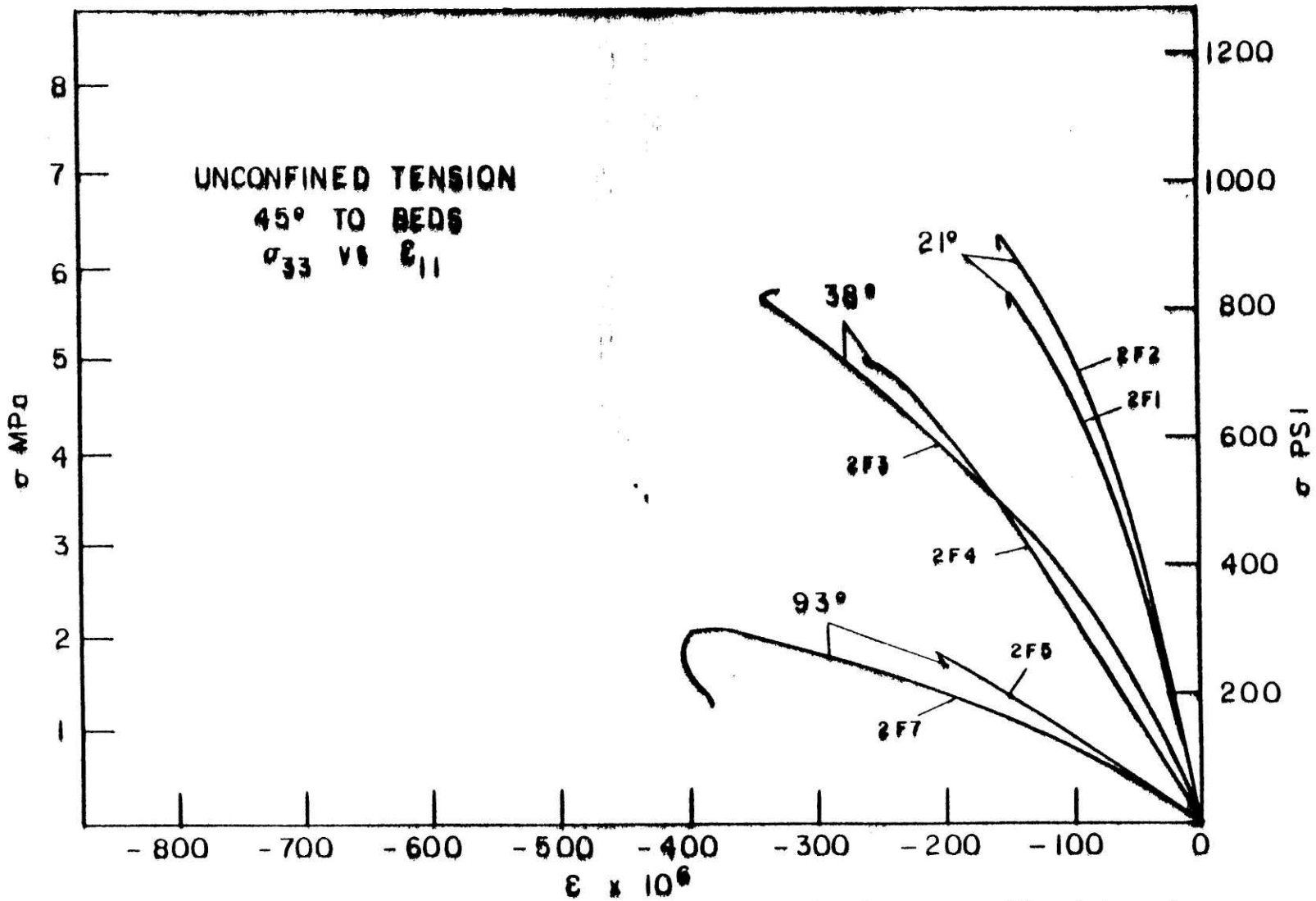

Figure 5c: Axial stress vs. transverse strain for unconfined tension 45° to bedding for nominal 30 gpt shale. Transverse strain measured in $\underline{e}_1$ direction.

tangent moduli (to 4.5GPa (6.5×10^5 psi)) and an approximate four-fold decrease in failure strength were recorded in going from room temperature up to 93°C (200°F). Thus, for 45° tension, at least to 93°C, interplanar weaknesses due to onset of organic breakdown* was not a predominant factor in the failure of the specimen. Failure stress, however, exhibited a closer similarity with those for tests run normal to the bedding planes. Fracture strains of less than 1 me were measured, even at 93°C (200°F).

Calculated values for shear moduli showed moderate scattering, particularly at the lower temperatures. Standard deviations were roughly 40% of mean at 21°C (70°F), decreasing to 5% of mean at 93°C (200°F). Average values for G_{mn}, from the $\theta=\pi/4$ tests, ranged from 7.6 GPa (1.1×10^6 psi) at 21°C (70°F) to 1.6 GPa (2.3×10^5 psi) at 93°C (200°F).

1. Comparative Results. Previous tensile testing of oil shale, albeit at room temperature only, has been done by Hangen (1977). An adequate comparison of data can be

*It was found throughout all the higher temperature (>93°c) tests that this initial organic breakdown led to a general weakening between the bedding planes (where most of the organic matter is thought to exist). This invariably induced failure along the bedding planes for tests in all orientations.

made with his results for nominally 34gpt nahcolite shale. The presence of nahcolite in his test specimens (which he described as serendipitous) is noted and, therefore, a careful comparison is made in light of his analysis of its effects on his results. Hangen (1977) reported initial tangent moduli of 5.56 Pa (8.0 x 10^5 psi) and 16.7 GPa (2.5 x 10^6 psi) for tests normal and parallel to beds, respectively. Measurements were also given for failure strengths/strains,namely 2.0 MPa (290 psi)/0.30 me and 9.0 MPa (1730 psi)/0.50me for the normal/parallel tests. The presence of nahcolite in his samples apparently weakened his shale to some extent (as he rationalized), since his failure strengths and strains are consistently lower than these found in Table IV. However, the other values illustrated in Table IV all agree with his, within experimental scatter.

Other static (and literature values of dynamic) Young's moduli are presented by Hangen (1977). Close agreement is found with static data reported by Seller, et al. (1972) and Schmidt and Schuler (1974), i.e., $E_{mm} \simeq$ 11.0 GPa (1.6x10^6psi) and $E_{nn} \simeq$ 10.0 GPa (1.5x10^6 psi), respectively.

TABLE IV

INITIAL TANGENT MODULI, POISSON RATIOS, AND FAILURE STRENGTHS AND STRAINS FOR NOMINAL 30 GPT SHALE AT ELEVATED TEMPERATURES IN UNIAXIAL TENSION

#Tests	Orient.	Temp. °C(°F)	E_{nn} GPa(psi)	ν_{mn}		Failure σ:MPa(psi)	ε:mε
3	1	21 (70)	8.3 (1.8×10^6)	.25		2.5 (365)	0.17
3	1	38 (100)	6.6 (9.5×10^5)	.33		1.9 (280)	0.30
2	1	93 (200)	1.7 (2.4×10^5)	.42		0.65 (95)	0.57
2	1	121 (250)	0.83(1.2×10^5)	.35		0.48 (70)	0.65
1	1	149 (300)	0.97(1.4×10^5)	.40		0.41 (60)	0.55
			E_{mm}	ν_{nm}	ν_{tm}		
3	//	21 (70)	16.5 (2.4×10^6)	.28	.21	7.6(1100)	1.0
3	//	38 (100)	9.0 (1.3×10^6)	.32	.28	6.3 (910)	2.0
3	//	93 (200)	1.4 (2.1×10^5)	.43	.35	2.4 (350)	3.7
			E_{33}	ν_{13}	ν_{23}		
3	$\pi/4$	21 (70)	20.6 (3.0×10^6)	.33	.38	6.0 (875)	0.40
3	$\pi/4$	38 (100)	7.6 (1.1×10^6)	.36	.36	5.4 (780)	0.81
2	$\pi/4$	93 (200)	4.5 (6.5×10^5)	.50	.41	1.7 (250)	0.50

2. Fracture Mechanisms. For consistency, the tensile tests were all performed at a loading rate of approximately 0.01 MPa per second (1.5 psi/sec) - unless stated otherwise. Figure 6 shows several tensile specimens after failure. They reveal that failure inevitably occurred between the bedding planes at all temperatures except in tests parallel to the beds (e.g., Schuler, 1977). Further testing for the critical $\theta > \pi/4$ is, therefore, warranted to explore where this failure transition occurs. The marked decreases in failure strengths and initial moduli (Table IV) between 38°C and 93°C suggest an initiation of kerogen pyrolysis and a breakdown of inter-bed bond strength. Some delamination along bedding planes was noticed at temperatures greater than 93°C (200°F). Brittle fractures were observed in all orientations up to 38°C (100°F). Between that temperature and 93°C, however, a transition to more "ductile" failure was detected, and rupture occurred long after the maximum stress level was attained.

Although kerogen pyrolysis was indeed suggested at temperatures greater than 38°C, no visible excretions of kerogen were observed (Figure 6). Color alterations (presumably due to pyrolysis) were observed at all temperatures above ambient. Thermal cracking (probably in a more general sense than classically used) was

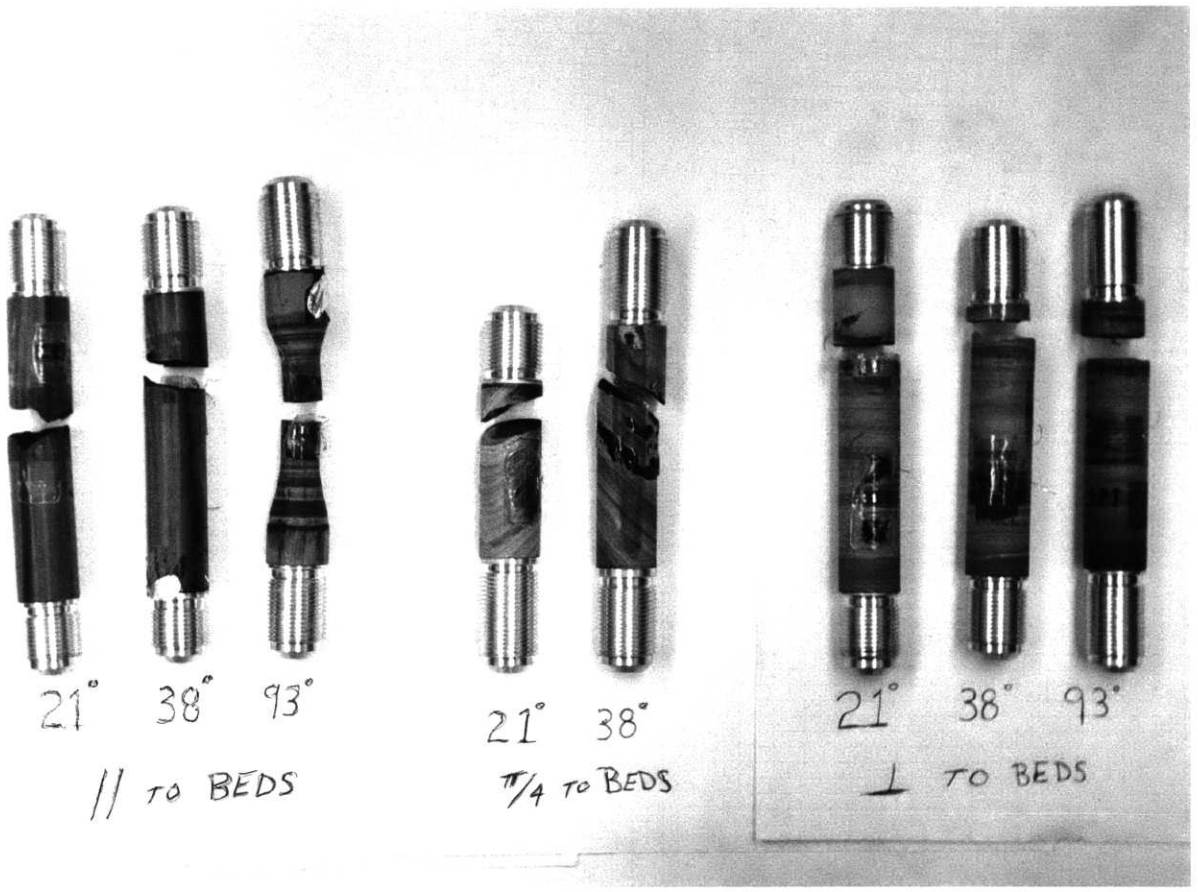

Figure 6: Nominal 30gpt shale specimens failed in uniaxial tension at various temperatures. //, ⊥, and 45° refer to tests parallel, perpendicular, and at 45° to bedding, respectively.

particularly evident at temperatures of 93°C or more, and for cores cut normal to the bedding -- indicating a size effect previously noted by Hangen (1977). Whether or not these crack could have formed under a confining stress is an important factor that will be determined in future testing.

B. High Temperature Uniaxial Compression Tests

Unconfined compression tests were performed from room temperature up to 204°C (400°F) using a special compression cage in an environmental chamber (Appendix IV). The specimens were loaded perfectly by the inner cage platens, without end pieces. It is known (e.g., Lama and Vutukuri, 1978) that direct platen loading introduces a triaxial state of stress at the contact surfaces due to frictional effects (see Figure 7). This stress region extends into the specimen in a cone-type shape, beyond which there exists an effectively uniform stress distribution. Tests were also performed using aluminum end pieces to achieve a more uniform stress state throughout the entire core and these are designated accordingly. For loading normal to the bedding planes, results showing longitudinal and transverse strains are illustrated in

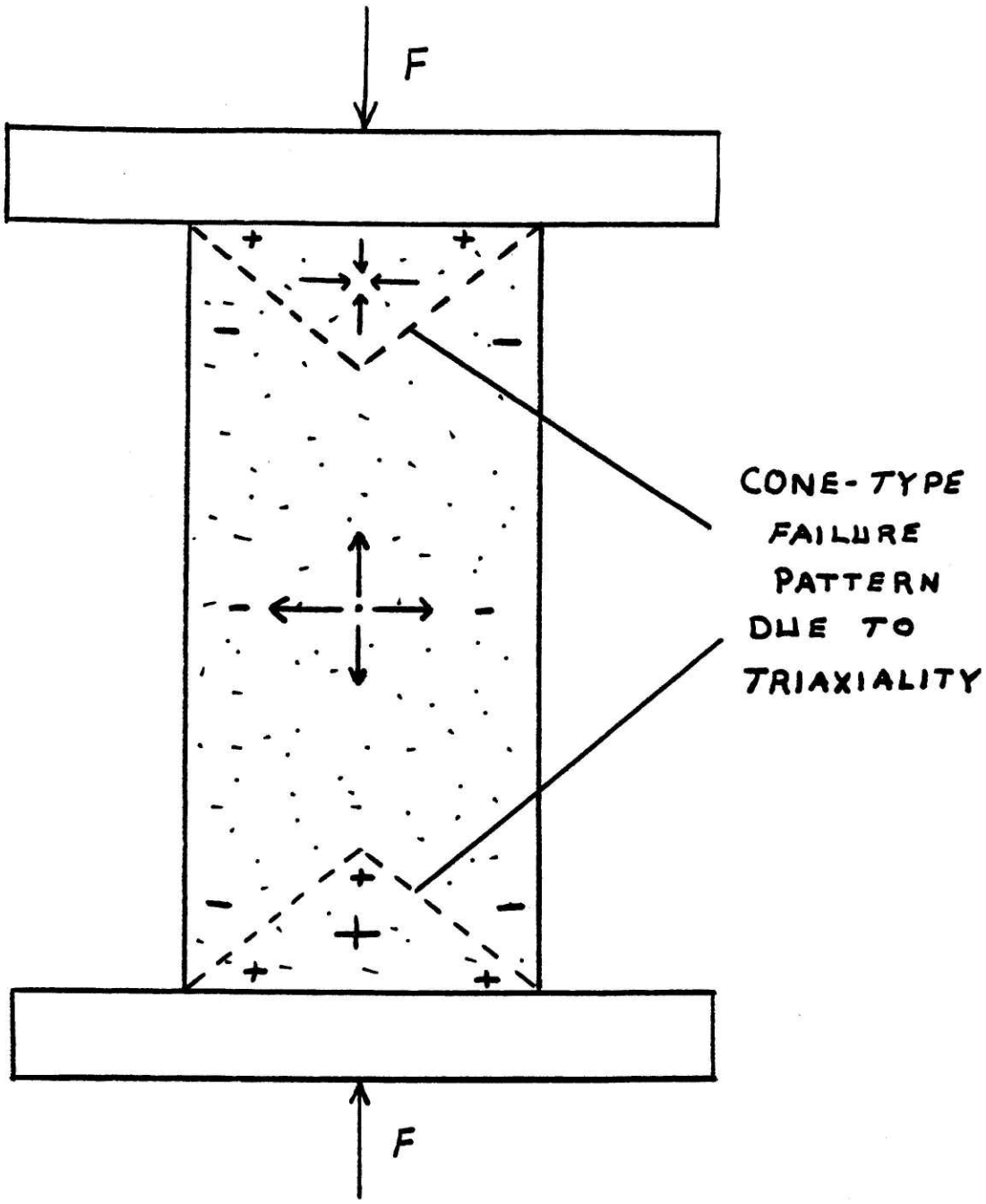

Figure 7: Direct platen loading and resultant material stress state

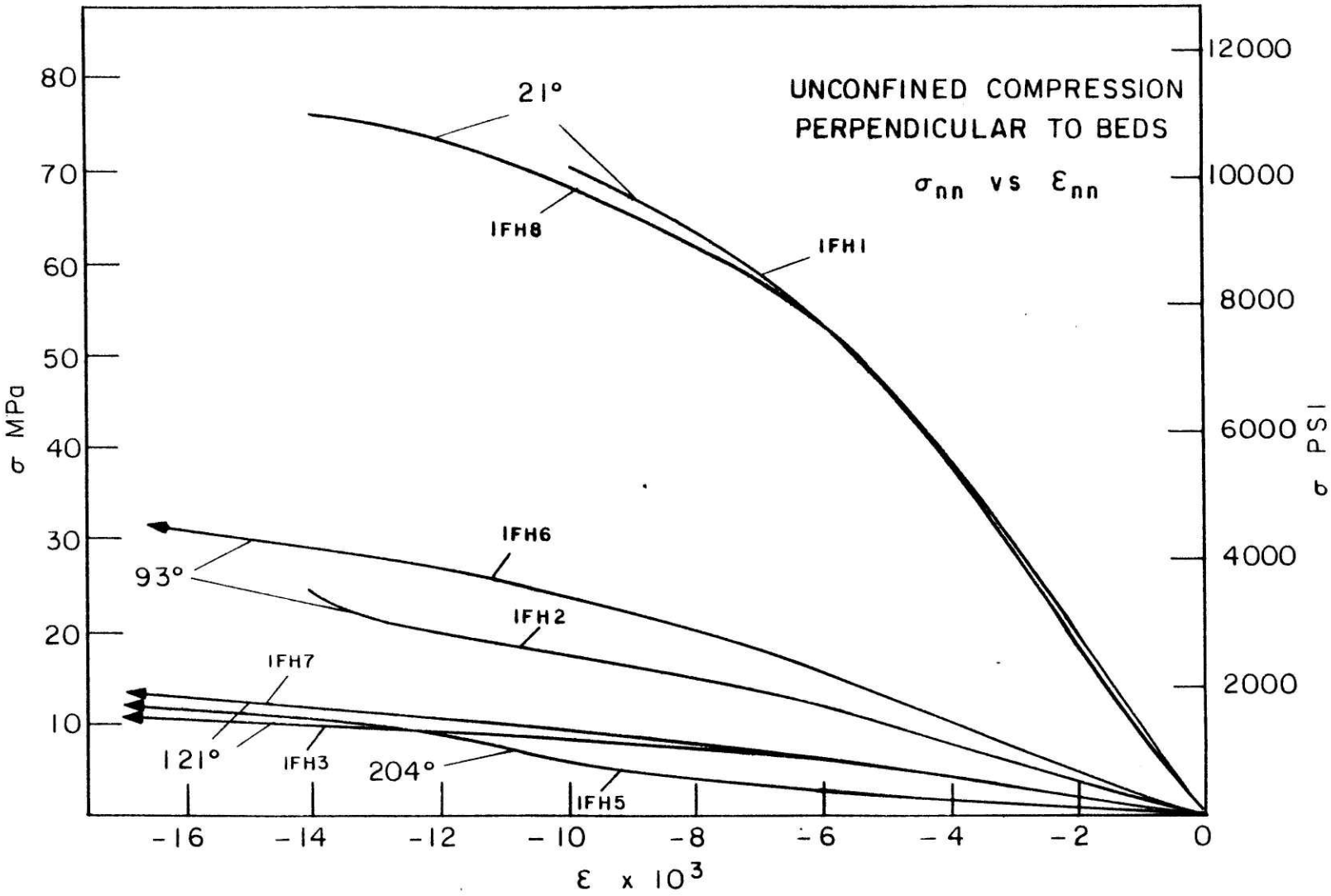

Figure 8a: Axial stress vs. axial strain for unconfined compression perpendicular to bedding for nominal 30 gpt shale. Compressive stress taken as positive.

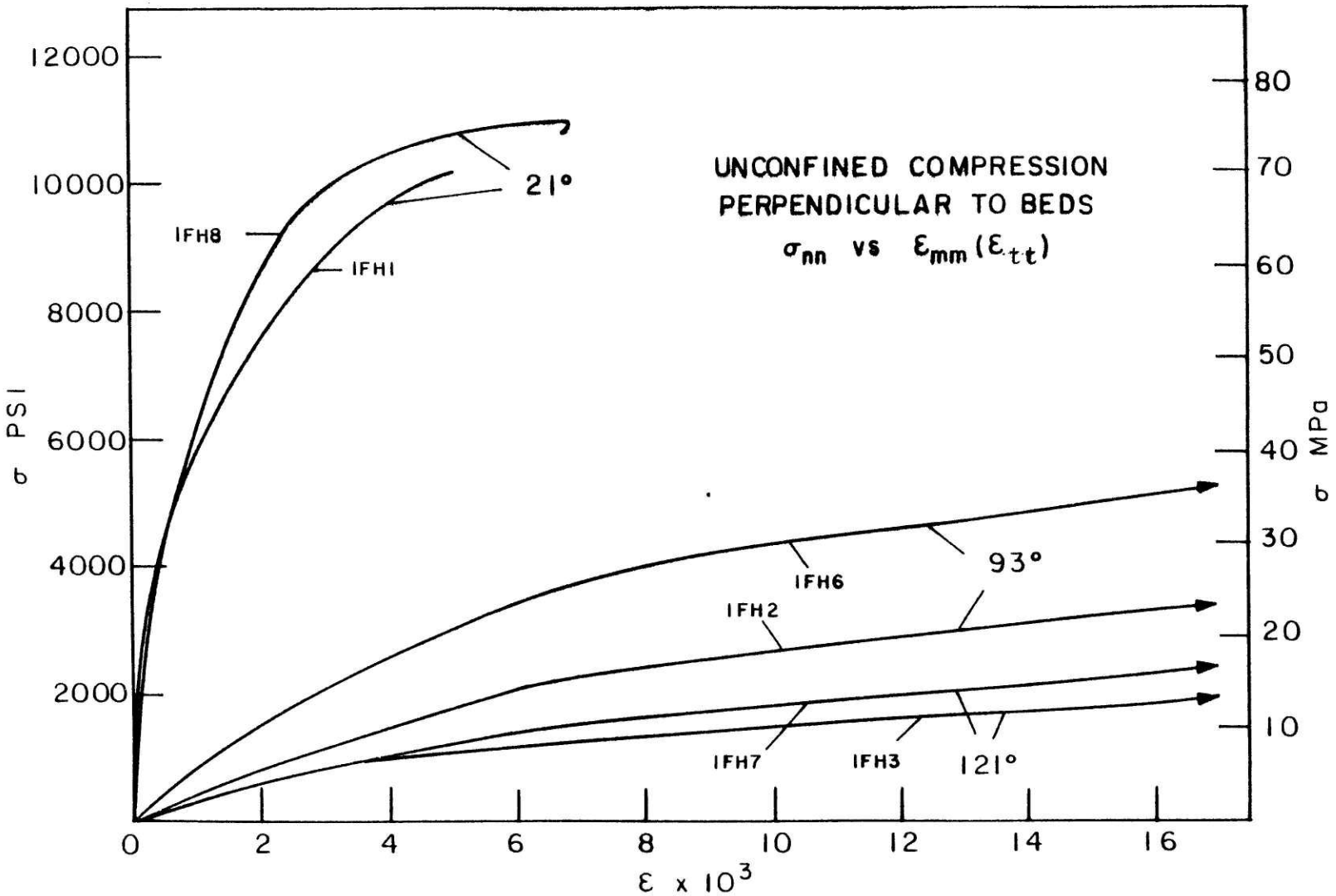

Figure 8b: Axial stress vs. transverse strain for unconfined compression perpendicular to bedding for nominal 30 gpt shale. Compressive stress taken as positive.

with increasing temperature. As in the tensile tests, this suggests a rapid intensification of organic material breakdown somewhere between 38°C (100°F) and 93°C (200°F). This was noted throughout all the tests.

Additional data is presented in Table V for high temperature compression tests.

The stress-strain curves for longitudinal and transverse strains, for compression parallel to the bedding planes, are plotted in Figures 9(a,b,c). Strain gage measurement of pertinent transverse strains was possible to 121°C (200°F). An immediate fall-off in longitudinal stress response is apparent in Figure 9a, suggesting minimal early crack closing in this orientation.* However, for tests at 93°C or above, initial high compliancy was indeed observed. This suggests that some kerogen exists in the planes themselves, where matrix material predominates. Along with any matrix inhomogeneities, this general reorganization of internal structure resulted in the observed initial reverse curvature, followed by the characteristic decreasing modulus of inelastic response. Initial tangent moduli ranged from 22.0 GPa (3.2×10^6 psi) at 21°C to

*Since most cracks are found in the planes of the beds, this would be anticipated.

TABLE V

INITIAL TANGENT MODULI, POISSON RATIOS, AND FAILURE STRENGTHS AND STRAINS FOR NOMINAL 30 GPT SHALE AT ELEVATED TEMPERATURES IN UNIAXIAL COMPRESSION: (⊥) NORMAL TO BEDDING, (//) PARALLEL TO BEDDING, ($\pi/4$) 45° PARALLEL TO BEDDING (FIGURE 4).

Tests	Orient.	Temp. °C	(°F)	Enn GPa (psi)	ν_{mn}	Failure σ_{nn} MPa (psi)	ε_{nn} me
2	⊥	21	(70)	7.6 (1.1×10^6)	.26	72.5 (10500)	12
2	⊥	93	(200	1.7 (2.5×10^5)	.52	30.3 (4500)	30
2	⊥	121	(250)	1.4 (2.1×10^5)	(.60)	21.4 (3100)	45
2	⊥	204	(400)	0.31(4.5×10^4)	-	15.2 (2200)	50
				Emm GPa (psi)	ν_{nm} ν_{tm}	σ_{mm}	ε_{mm}
3	//	21	(70)	22.0 (3.2×10^6)	.29 .24	64.9 (9400)	6.0
3	//	93	(200)	2.8 (4.1×10^5)	(.70) (.61)	30.3 (4400)	11
2	//	121	(250)	1.4 (2.1×10^5)	(.83) (.80)	18.6 (2700)	16
3	//	204	(400)	0.21($3x0x10^4$)	- -	9.7 (1400)	35
				E_{33}	ν_{13} ν_{23}	σ_{33}	ε_{33}
4	$\pi/4$	21	(70)	14.5 (2.1×10^6)	.22 .30	63.4 (9200)	6.8
1	$\pi/4$	38	(100)	8.3 (1.2×10^6)	.26 .32	60.0 (8700)	7.0
3	$\pi/4$	93	(200)	4.6 (6.7×10^5)	.45 .50	45.5 (6600)	13
2	$\pi/4$	121	(250)	1.7 (2.4×10^5)	(.52) (.51)	31.0 (4500)	21
2	$\pi/4$	204	(400)	0.21(3.1×10^4)	- -	9.0 (1300)	40

* These values (ν) are not truly Poisson ratios per se, because of thermal effects, but are given for referral purposes.

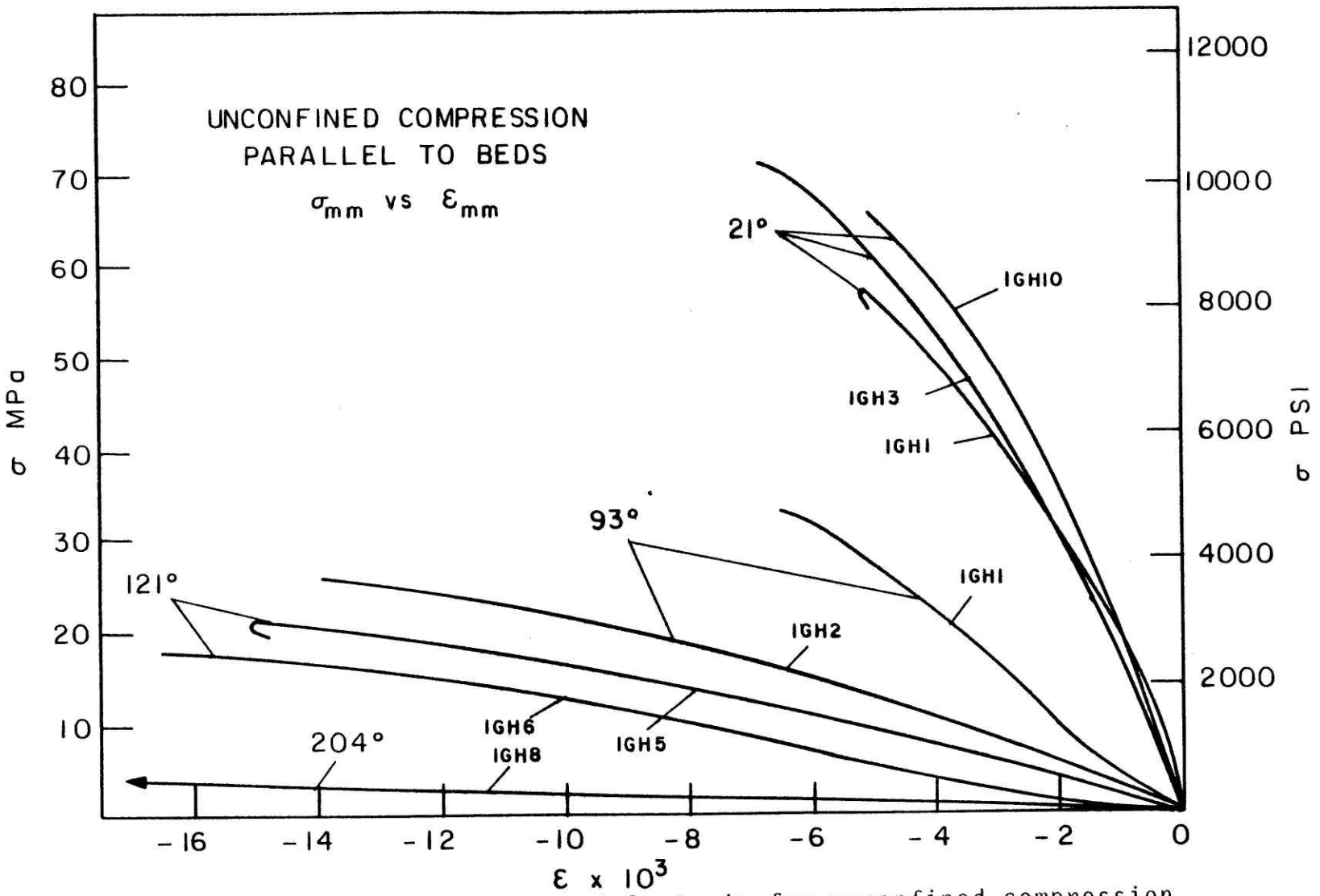

Figure 9a: Axial stress vs. axial strain for unconfined compression parallel to bedding for nominal 30 gpt shale. Compressive stress taken as positive.

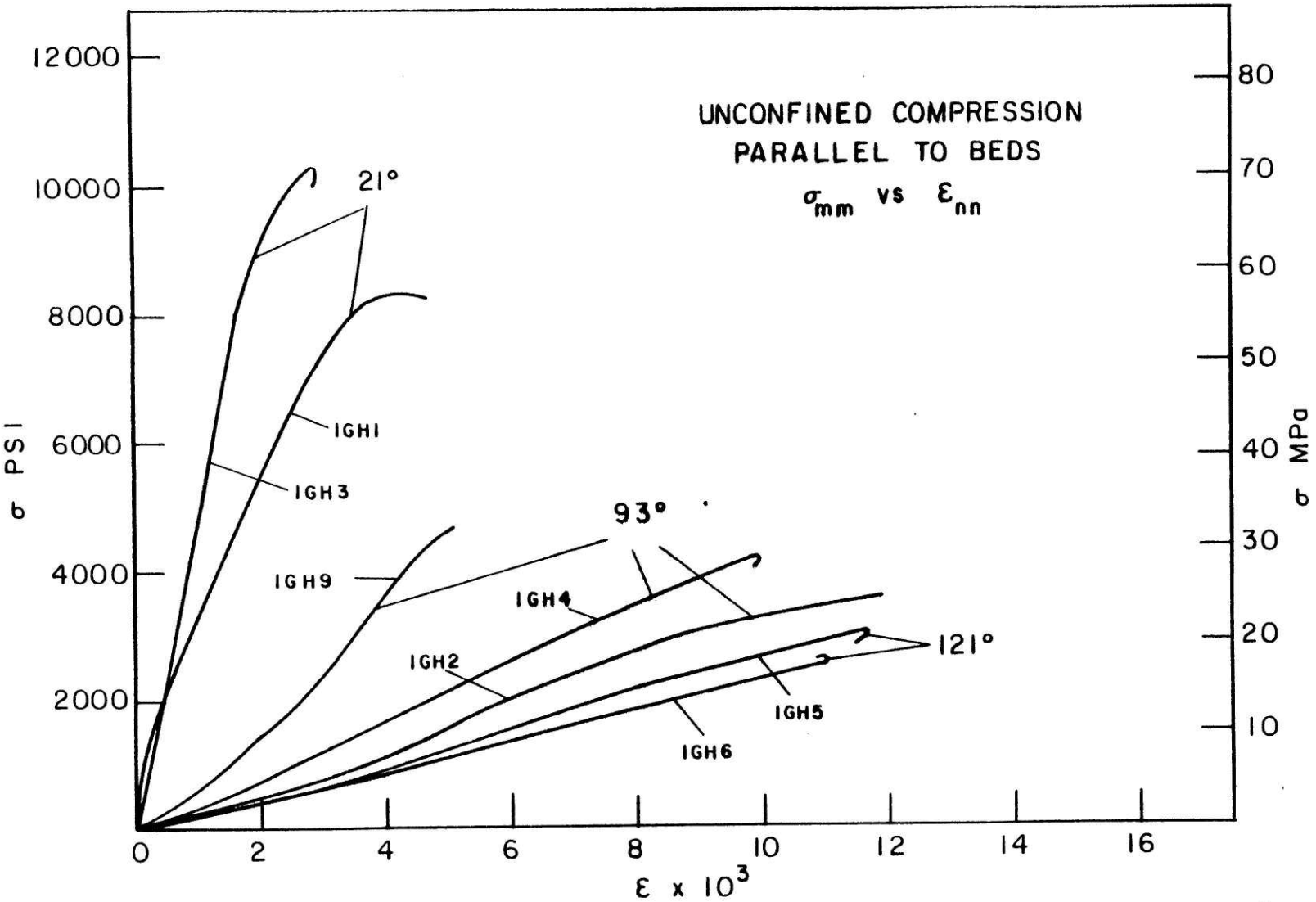

Figure 9b: Axial stress vs. transverse strain for unconfined compression parallel to bedding for nominal 30 gpt shale. Transverse strain measured normal to bedding. Compressive stress taken as positive.

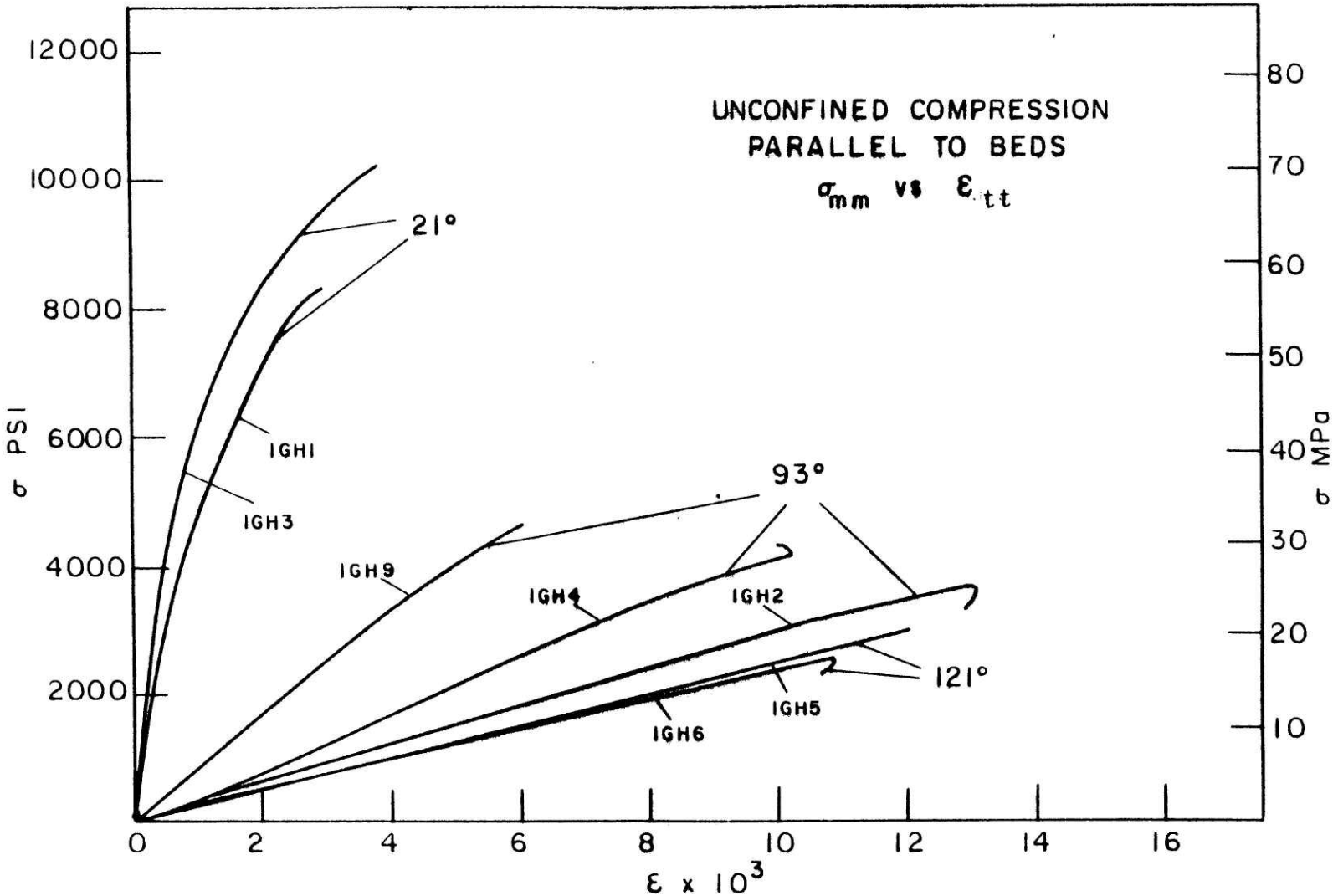

Figure 9c: Axial stress vs. transverse strain for unconfined compression parallel to bedding for nominal 30 gpt shale. Transverse strain measured parallel to bedding. Compressive stress taken as positive.

0.21 GPa (3.0×10^4 psi) at 204°C. Failure strengths(strains) decreased (increased) seven-fold (six-fold) over that same temperature range. Scatter was again minimal ($s^* \leq 15$ % of average value) for all categories, being generally even smaller than that for compression normal to beds. High transverse strains in both the $\underset{\sim}{n}$ and $\underset{\sim}{t}$ directions were observed above 38°C (100°F), resulting in gross delaminations upon failure (to be discussed later). Consult Table V for more specific data.

Experimental tests were also performed on specimens in the $\theta = \pi/4$ orientation (Figure 4); the results are presented in Figs. 10(a,b,c). The onset of nonlinearity can be identified up to 93°C: this happens roughly at 10 MPa (1500 psi) for 21°C and 5.5 MPa (80°psi) for 93°C. From ambient to 204°C, seventy-fold decreases in tangent moduli and seven-fold decreases in strength, and an approximate six-fold increase in failure strain were measured. Failures were solely along the bedding planes, with no thermal cracking or organic secretions in evidence (as discussed later). Also, failure strengths were surprisingly high in the 38°C - 121°C range, indicating that shear and normal stresses do not reinforce each other to produce failure, viz. not in accordance with a simple

---

*s = standard deviation.

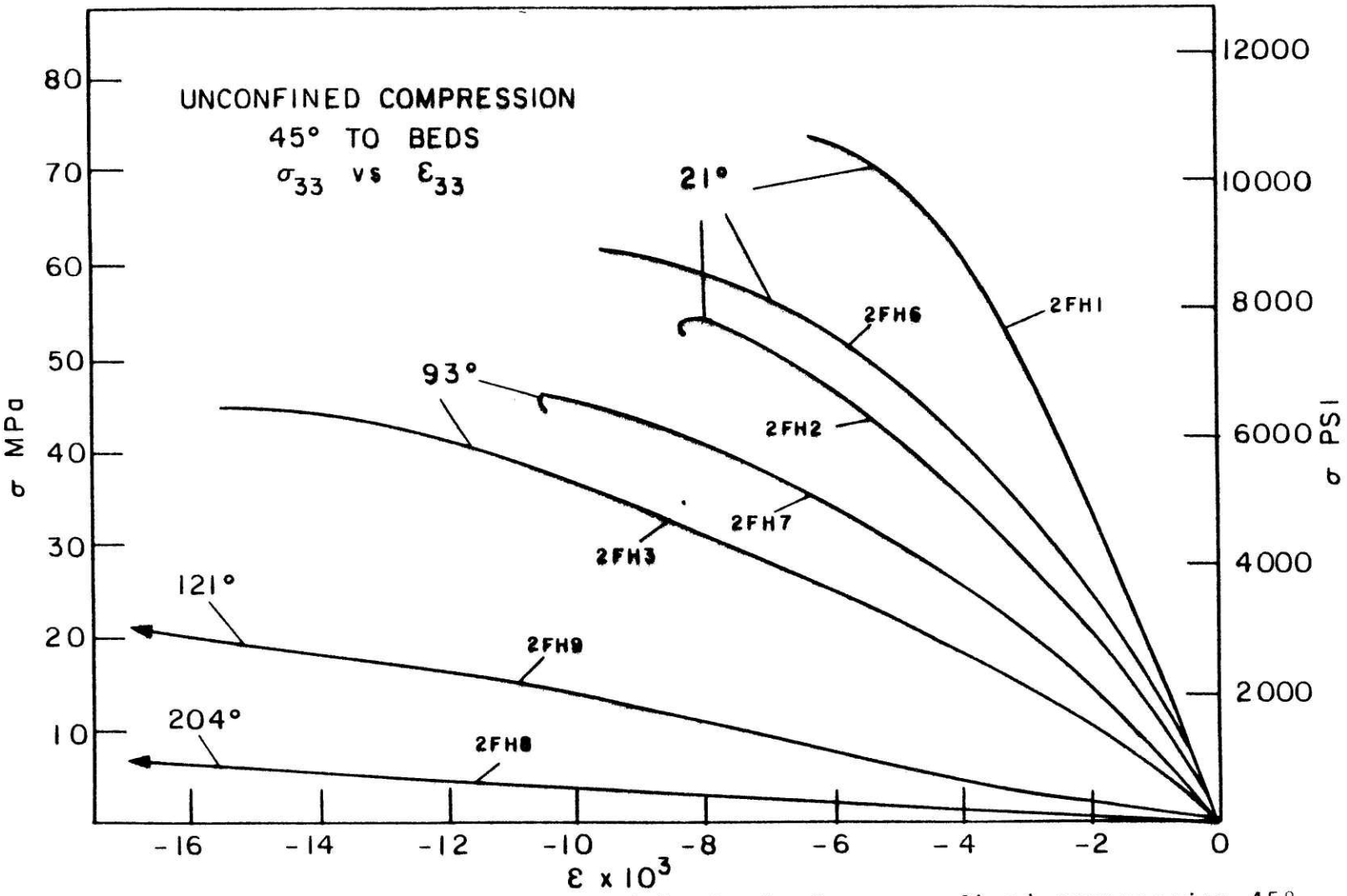

Figure 10a: Axial stress vs. axial strain for unconfined compression 45° to bedding for nominal 30 gpt shale. Compressive stress taken as positive.

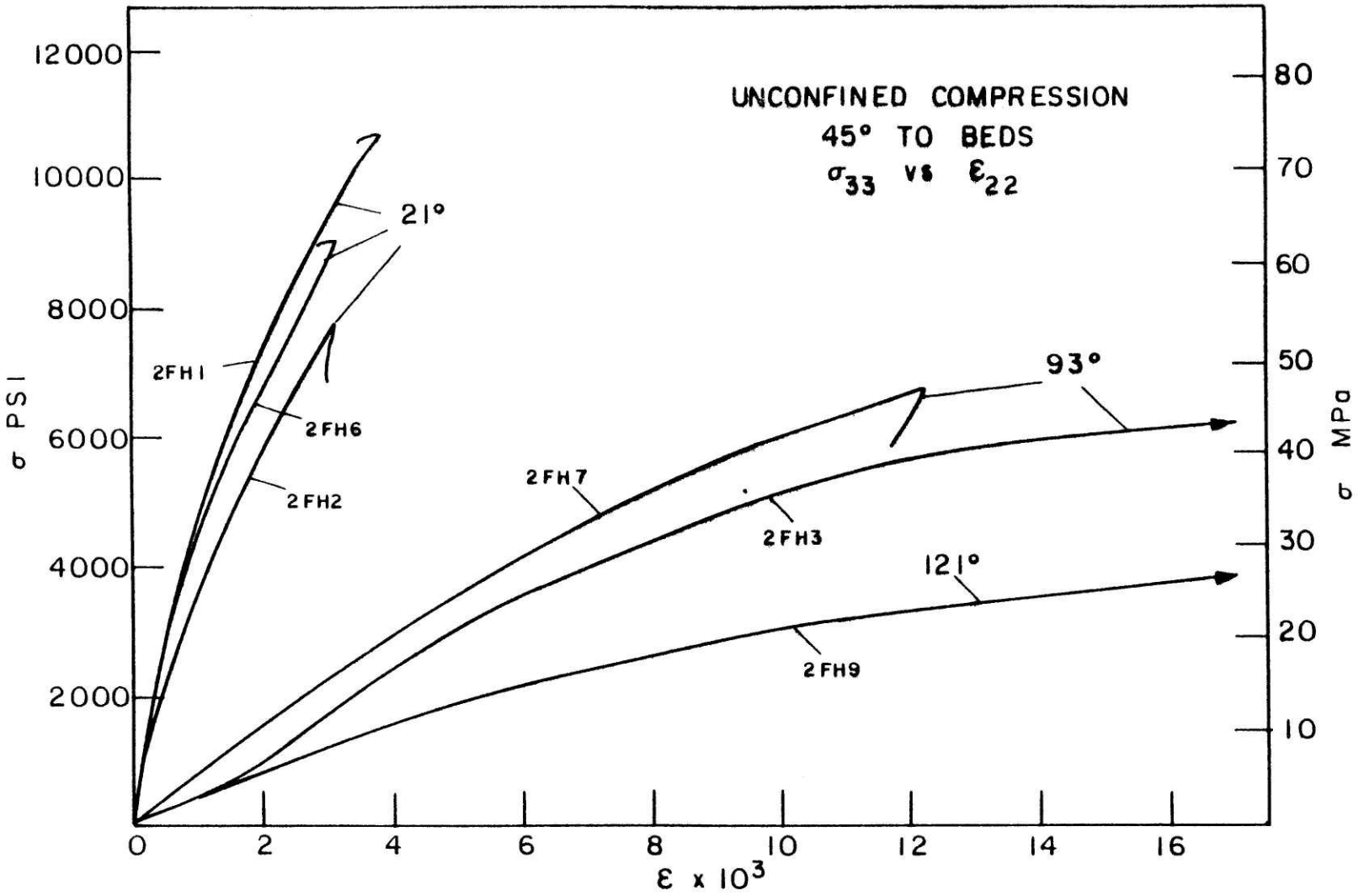

Figure 10b: Axial stress vs. transverse strain for unconfined compression 45° to bedding for nominal 30 gpt shale. Transverse strain measured in $\underset{\sim}{e}_2$ direction. Compressive stress taken as positive.

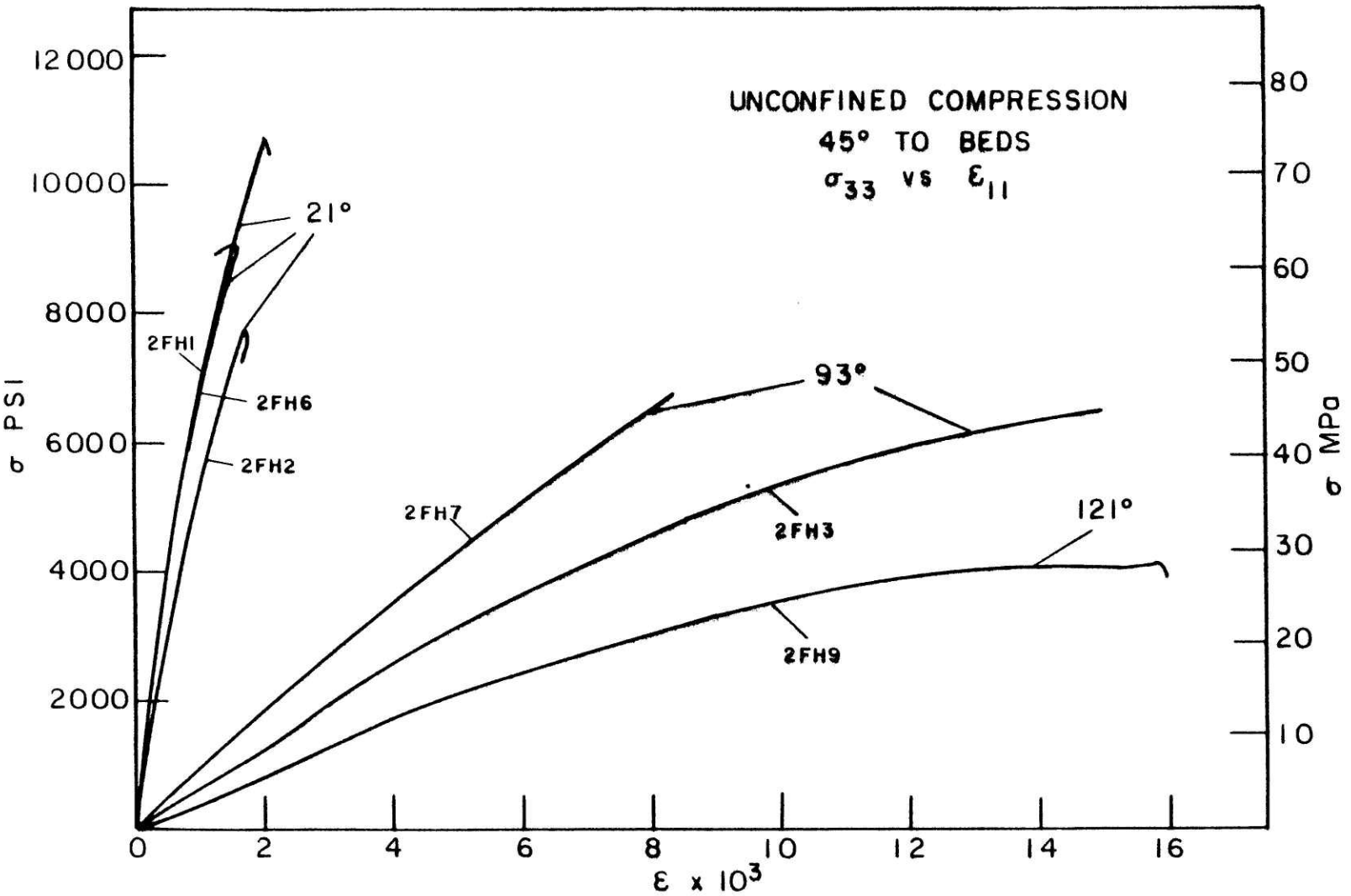

Figure 10c: Axial stress vs. transverse strain for unconfined compression 45° to bedding for nominal 30 gpt shale. Transverse strain measured in $\underset{\sim}{e}_1$ direction. Compressive stress taken as positive.

isotropic law; this anisotropy in strength is characterized later.

Shear moduli values G_{mn} determined from these tests ranged from 56 GPa (8.1×10^5 psi) at 21°C to 0.54 GPa (7.8×10^4 psi) at 121°C. The overall consistency of the data again improved immensely at higher temperatures ($s \sim 50\%$ of mean at 21°C; $s \sim 10\%$ of mean at 121°C), illustrating less variation of response as temperature is increased. These moduli values appear again later in the constitutive relation.

1. Comparative Results: Comparison of the above results with those of Hangen (1977), again using his data for the nominal 34 gpt shale, reveals statistically comparable values for initial moduli, Poisson ratios, and failure strains in both principal directions. However, a discrepancy of a factor of two in failure strength is seen in tests normal to the bed, reported as 40.0 MPa (5,000 psi) by Hangen. This variation, as well as others detected, may be attributable to a difference in specimen preparation between the two studies. In order to achieve a more uniform uniaxial stress throughout the samples, insofar as the inhomogeneities of oil shale allow, Hangen (1977) applied loading through aluminum end pieces epoxied to the shale (analogous to preparation of tensile specimens).

These end pieces do not constrain the contact surfaces of the specimen to an extent equivalent with direct platen loading; consequently, lower strengths may result. Buckling was another factor involved in most of the compressive failures reported by Hangen . Since loading via direct platen was typically employed in this study, and also because length to diameter ratios were maintained between 2.0 and 2.3, no buckling failures were observed through the course of this work. However, several tests performed using caps showed consistently lower failure strengths and strains in both principal directions (48.3 MPa (7,000 psi) and $\epsilon_F \sim 15$ ms for both // and ⊥), confirming the trend in Hangen (1977).

High temperature tests reported by Hangen were for a nominal 65.1 gpt shale; therefore, only a qualitative comparison should be made. Over a temperature range of 38°C to 204°C, Hangen showed a six-fold (14-fold) decrease in failure strength and 50-fold (60-fold) decrease in tangent moduli for experiments normal (parallel) to the bedding plane. Much smaller decreases are reported here (Table V) for both strengths and moduli over that temperature range. This suggests a strong dependence of thermomechanical response on organic contact in the shales, as might be expected. Increased compliance with higher kerogen contact has been reported previously by other

researchers also, (e.g., Cameron Engineers, 1975; Sellers, et al. 1972; Schmidt and Schuler, 1974).

2. Fracture Mechanisms. Several compressive tests to failure at various temperatures in the three test orientations are pictured in Figures 11(a,b,c). All tests were run at a quasi-static loading rate of approximately 7MPa per minute (∿ 1000 psi/min) with lower rates in the case of higher temperature runs (∿ 1MPa per minute). Equivalent strain-rates of about 1 mε/min at 21°C to about 5mε/min at 204°C were achieved. Additionally, each specimen was stabilized at temperature for one hour* before axial loading was administered.

Failure modes at room temperature showed the familiar pattern, namely cone-type failure (explained in Figure 7) due to triaxiality at ends, for tests normal to bedding planes, and a diagonal, wedge-like failure pattern for cores parallel to beds, due to the linking up of smaller cracks between the beds - resulting from the weak inter-planar** tensile strength of the shale. Specimens at $\theta = \pi/4$

*It was determined in initial characterization tests that the 1.5 in. diameter cores required roughly 1/2 hour at temperature to reach thermal stability. (Appendix I).

**Tensile strength normal to bedding planes was approximately one fifth (1/5) of that for specimens parallel to the beds for all temperatures.

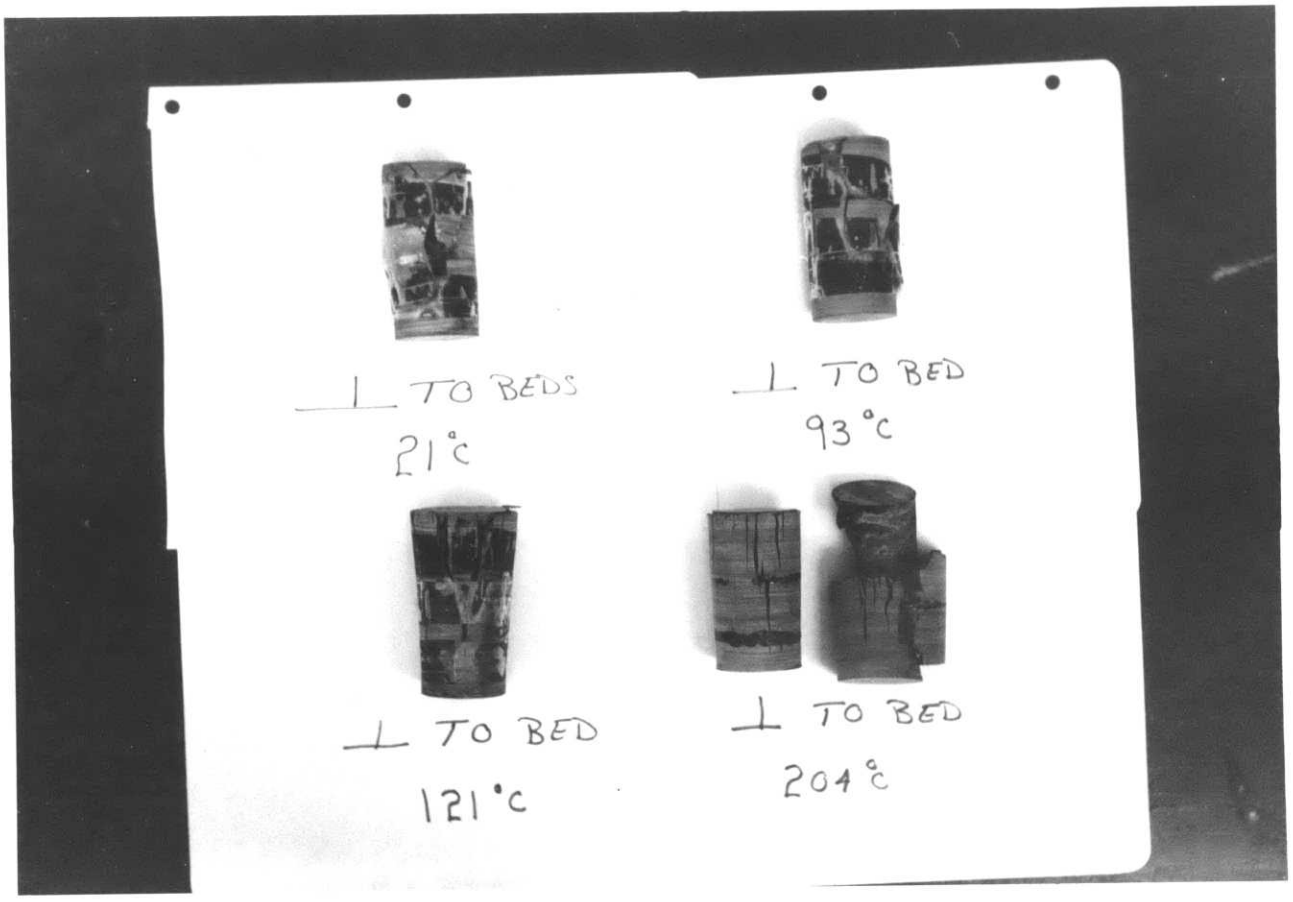

Figure 11a: Nominal 30 gpt shale specimens failed in uniaxial compression at various temperatures ⊥ designates tests perpendicular to bedding.

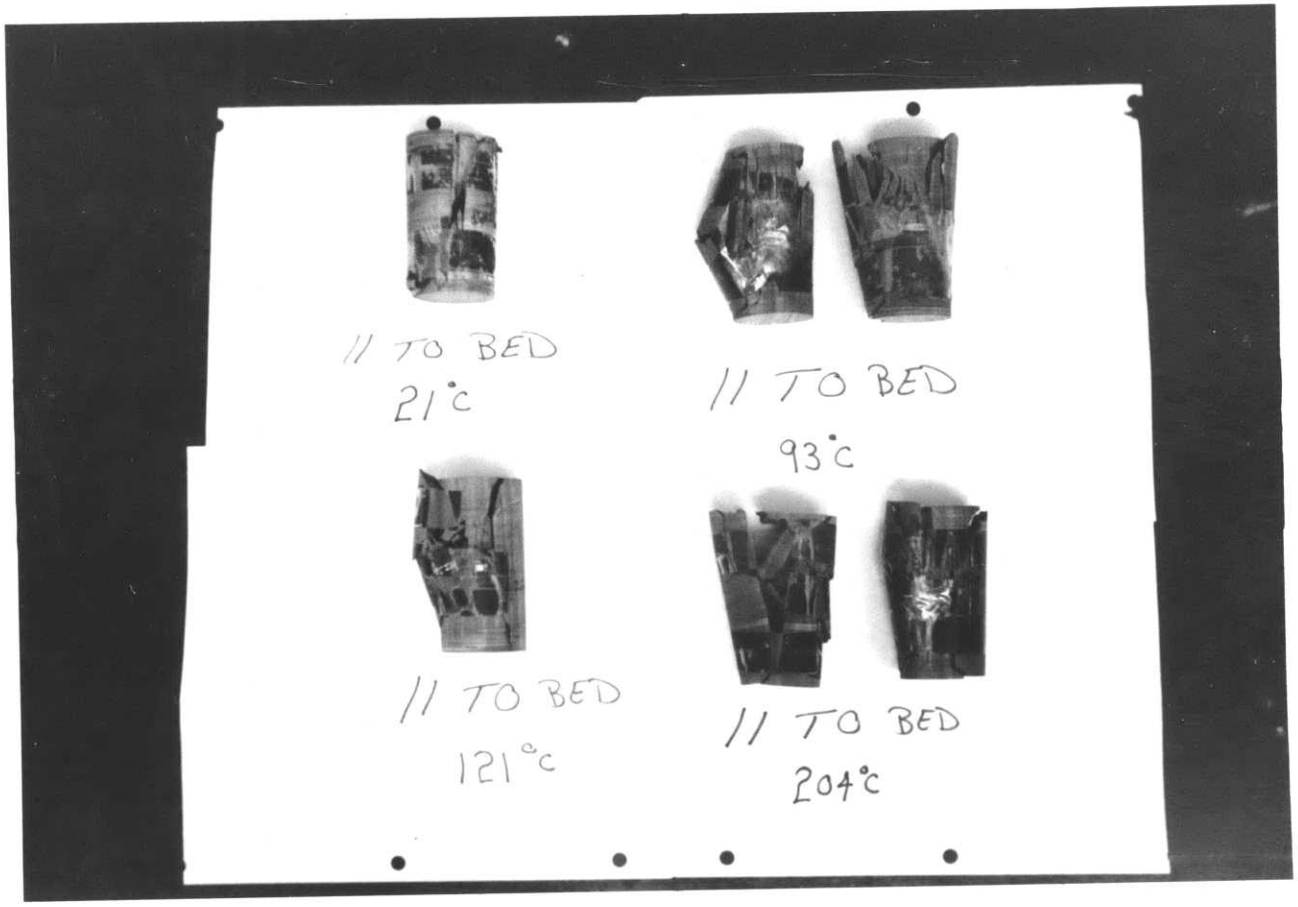

Figure 11b: Nominal 30 gpt shale specimens failed in uniaxial compression at various temperatures. // designates tests parallel to bedding.

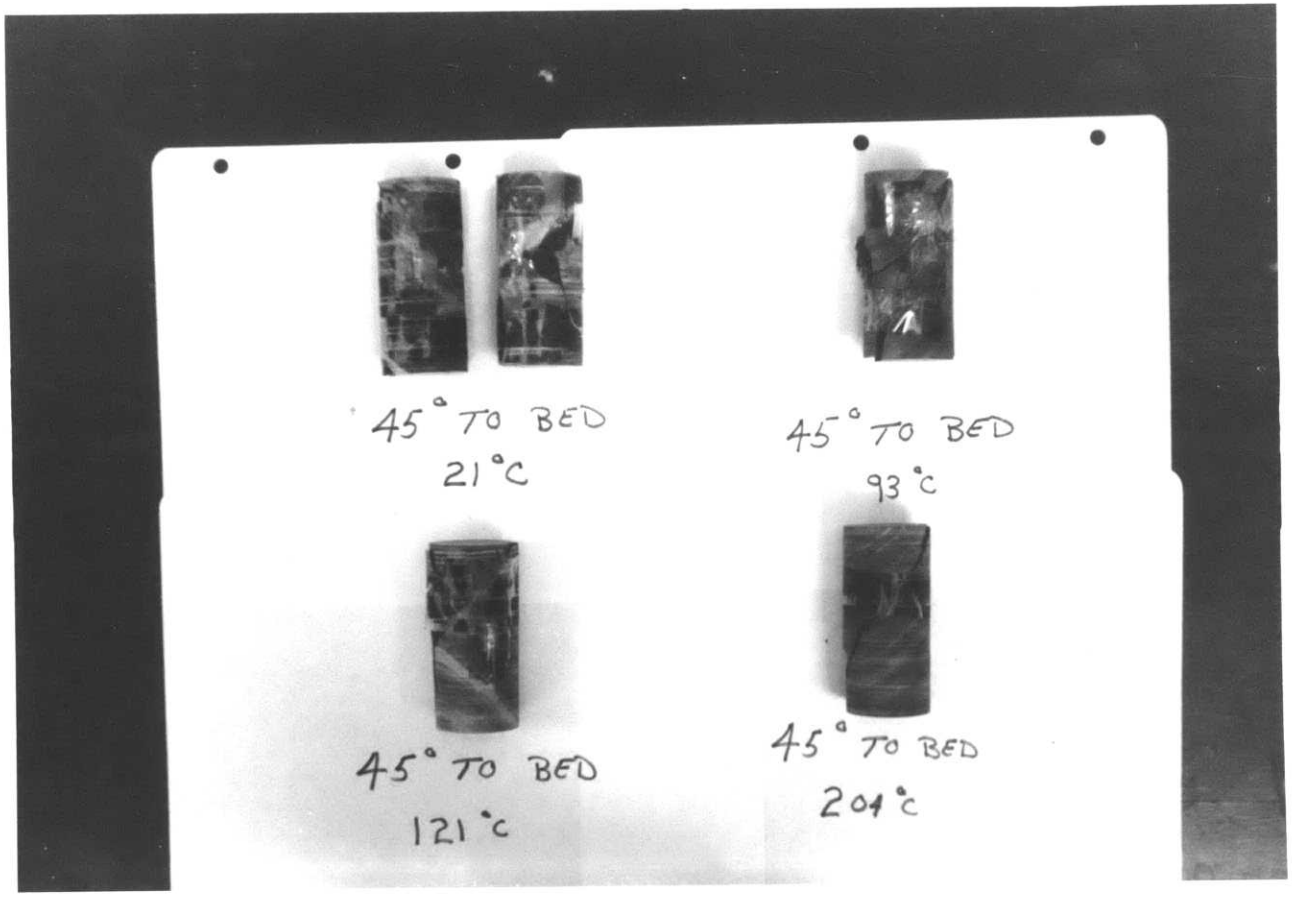

Figure 11c: Nominal 30 gpt shale specimens, 45° to bedding, failed in uniaxial compression at various temperatures.

showed failure along the bedding planes, again due to the shale's weak inter-planar strength (see Figure 11).

However, as the temperature was increased, several interesting observations were made. Firstly, for samples cored normal to bedding, the failure pattern was again the typical cone-like shape, even up to 204°C; still, as shown in Figure 11a, extensive vertical cracks began to appear at temperatures above 93°C. This suggested that a barrelling-induced circumferential stress was produced by the end constraints. It became obvious that this stress dominated more and more in specimen failure as temperatures increased. At 204°C (400°F), the effect was vividly clear (Figure 11a). Kerogen pyrolysis was most apparent in this orientation; actual fluid excretions were detected above 121°C, being very noticeable above 204°C. These organic excretions appeared to be purely thermally-induced, since fluid flow was observed prior to testing and remained essentially constant throughout the test. Although visible color alterations were observed for all orientations, generally increasing with temperature, no organic excretions were perceived other than in the tests perpendicular to the beds. As mentioned earlier, this suggests a size effect in the cores which warrants further investigation.

For temperatures at or above 93°C, tests performed

on cores cut parallel to the bedding planes revealed gross delamination of the beds prior to complete failure (Figure 11b). Thermal cracking was particularly evident along the beds in this orientation. This failure mode suggests increased kerogen pyrolysis with temperature, followed by a drastic reduction in interplanar strength (as was illustrated in tensile tests normal to beds). The barrelling-induced circumferential stress literally peeled away the bedding planes from one another.

Tests conducted on specimens in the $\theta = \pi/4$ orientation revealed a consistent failure mode - along the bedding planes-up to the highest temperature attainable (204°C). Minimal cracking, either mechanically on thermally-induced, outside of the main failure line was detected (Figure 11c). An important observation, however, pertains to the failure strength values presented in Table V. Although exhibiting failure strengths equal to those in tests in the two principal directions near room temperature and above 149°C (300°F), the 45° specimens demonstrated consistently higher strengths to failure in the range of 38°C - 149°C (see Figure 12 for compressive failure strengths versus temperature). This suggests an additional frictional sliding and hardening effect of bed on bed, not found in tests utilizing cores in the parallel on normal orientations. At lower temperatures (< 38°C), this

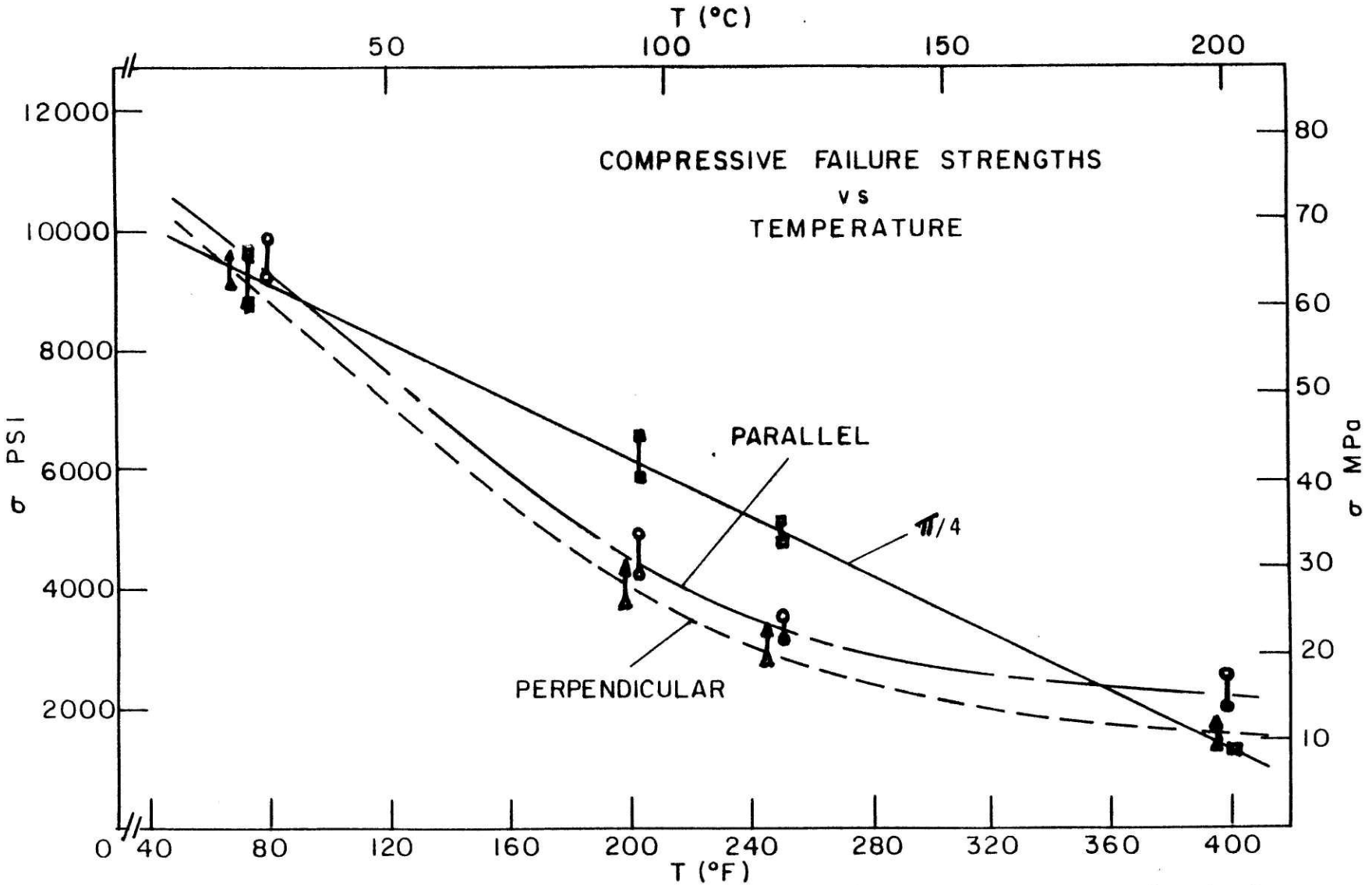

Figure 12: Plots of compressive failure strength vs. temperatures for tests perpendicular and 45° to bedding for nominal 30 gpt shale. Compressive failure strengths taken as positive.

frictional component would have some significance; however, as temperatures rise, this component becomes increasingly important in the overall strength of the material since other barriers involved in maintaining material integrity (e.g., interplanar tensile strength mentioned previously) are decreasing markedly. This continued until sufficient kerogen-rich material was pyrolyzed (at roughly 149°C) to act as a "lubricant" between the beds which thereafter substantially decreased the frictional effects of relative sliding. This explanation is somewhat justified since the 45° orientation tests exhibited the lowest failure strengths at temperatures around 204°C (Table V).

Organic breakdown (kerogen pyrolysis) and release as a vapor was detectable by smell at temperatures above 93°C in all orientations. This was subsequently confirmed by a miniscule weight loss determined in some of the tests.

C. Compression Stress Cycling and Stress Relief Tests.

Some compressive load cycling and stress relief experiments were performed on the nominal 30 gpt shale to determine whether stress-induced anisotropies could be introduced into the shale. These anisotropies, if readily apparent, would then have to be incorporated into any representative analytical characterization of the shale

(e.g., constitutive modeling). High temperature tests to 204°C were done on cores cut parallel, normal and at 45° to the bedding planes.

The initial phase of the experiments involved repetitive cycling to approximately 90% of failure stress at ambient temperature (21°C). Responses for longitudinal and transverse strains are illustrated in Figs. 13, 14 (a,b) and 15 (a,b) for tests normal, parallel and $\theta=\pi/4$ to bedding, respectively. Representative curves for loading and unloading response for the first, second, and tenth cycles are presented.

The largest hysteresis in response was detected in samples cored normal to the beds, while the least occurred in samples at $\theta=\pi/4$. This suggests that most of the shale's irreversible deformation occurred in the kerogen-rich laminae between the beds and that these organic strata were prone to greater "plastic" strain than the inorganic zones. For tests normal to the bedding planes, the material unloaded to roughly 89% of total failure strain plots after one cycle. After ten cycles, the unloading response for the axial strain was to 97% of total strain. Similarly, smaller strain losses were calculated for tests parallel and at 45° to bedding (Figs. 14-15). It was observed throughout all the runs, though, that stress-induced hysteresis was

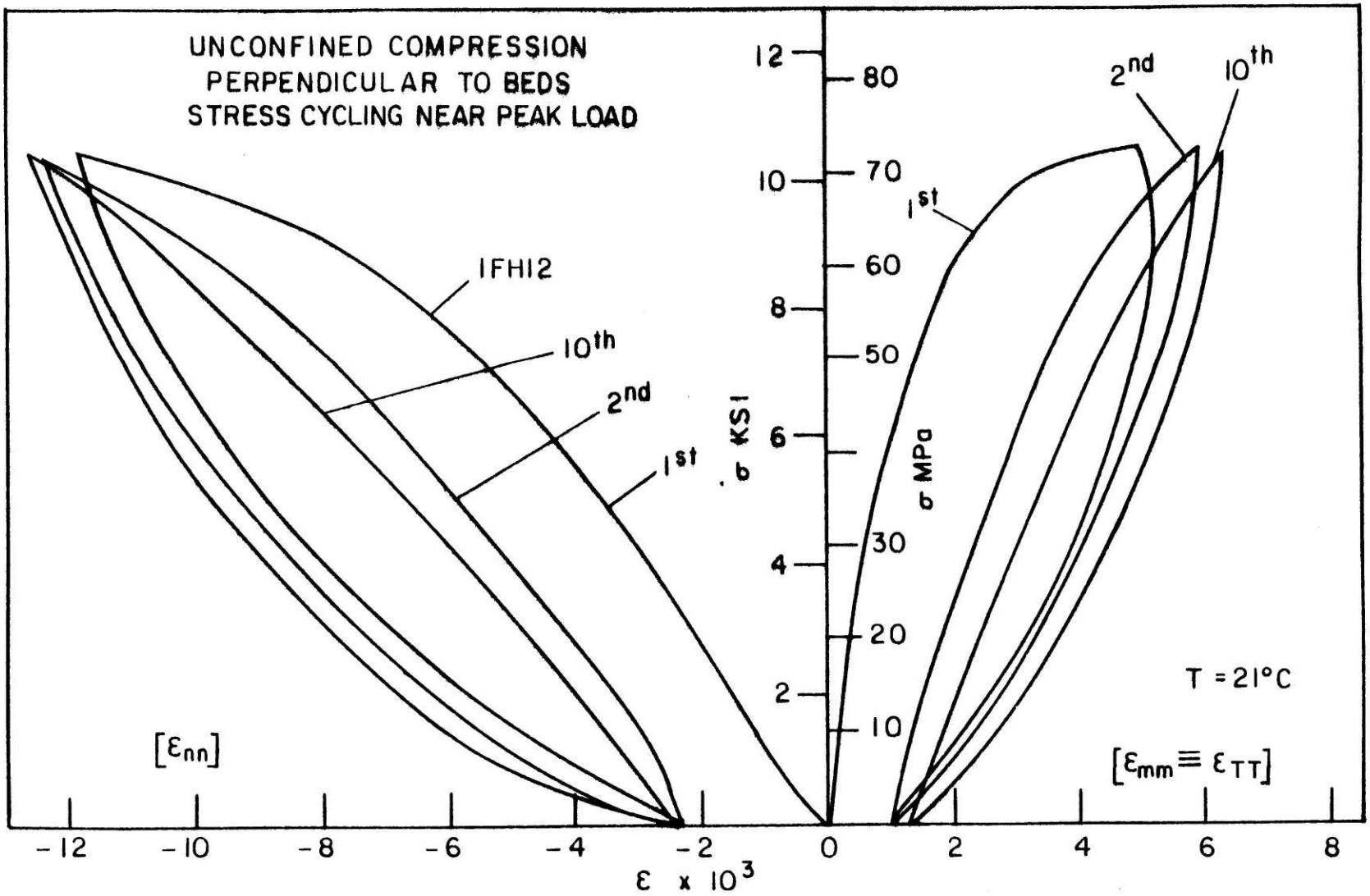

Figure 13: Axial stress vs. axial and transverse strains for unconfined compression perpendicular to bedding for nominal 30 gpt shale. 1st, 2nd, and 10th designate the first, second and tenth cycles, respectively. Compressive stress taken as positive.

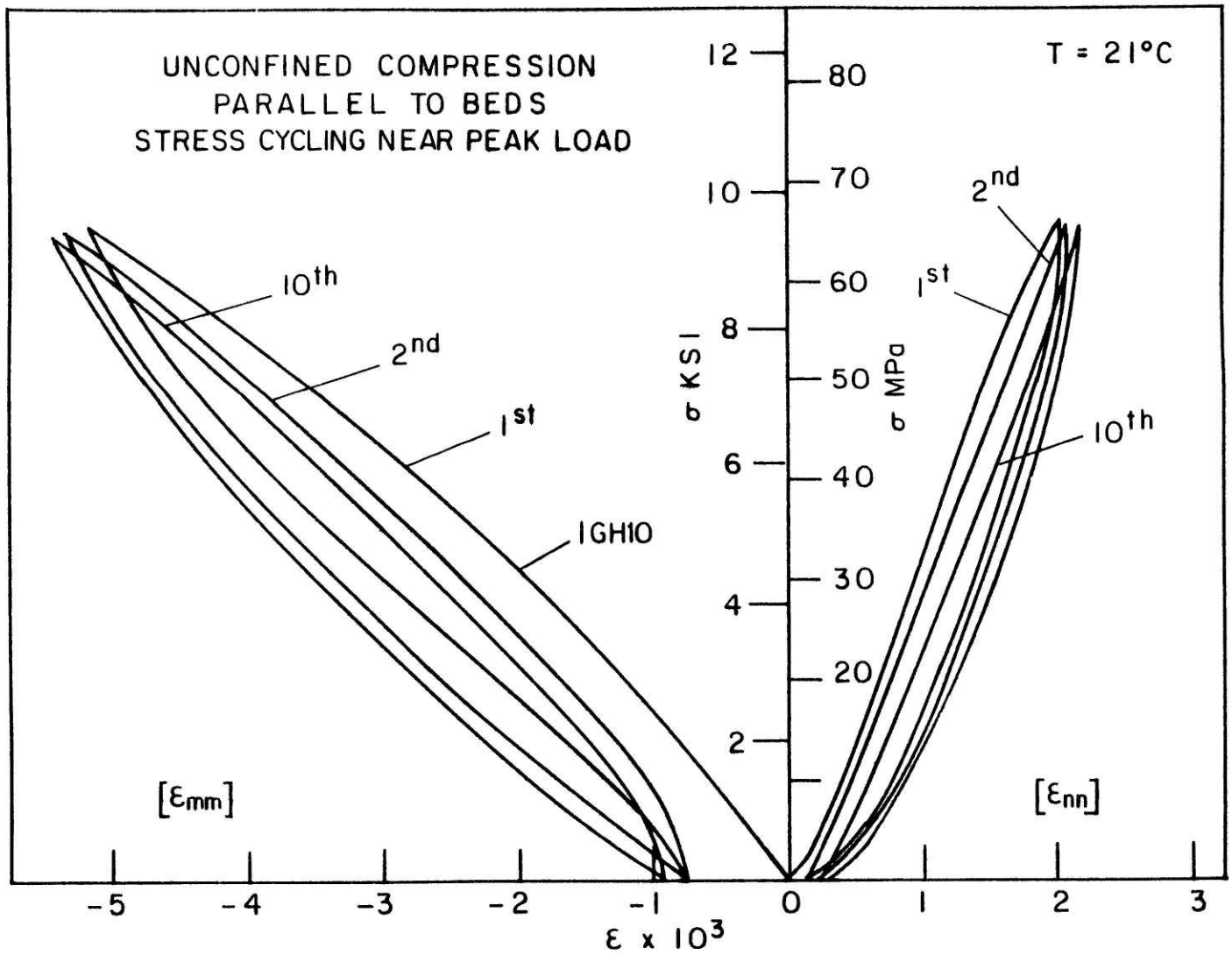

Figure 14a: Axial stress vs. axial and transverse strains for unconfined compression parallel to bedding at 21°C for nominal 30 gpt shale. Transverse strain, ε_{nn}, measured perpendicular to bedding. Compressive stress taken as positive.

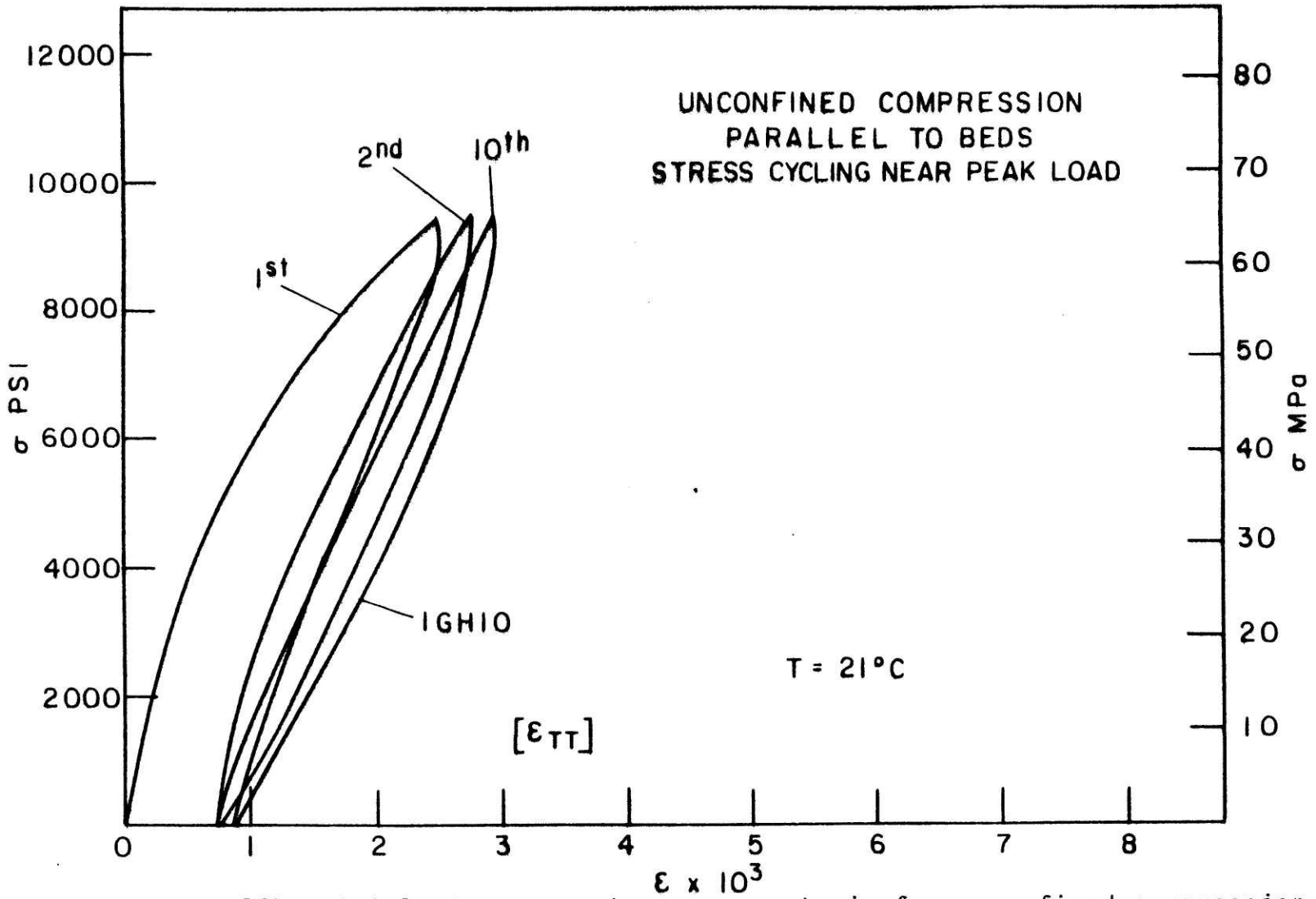

Figure 14b: Axial stress vs. transverse strain for unconfined compression parallel to bedding at 21°C for nominal 30 gpt shale. Transverse strain measured parallel to bedding. Compressive stress taken as positive.

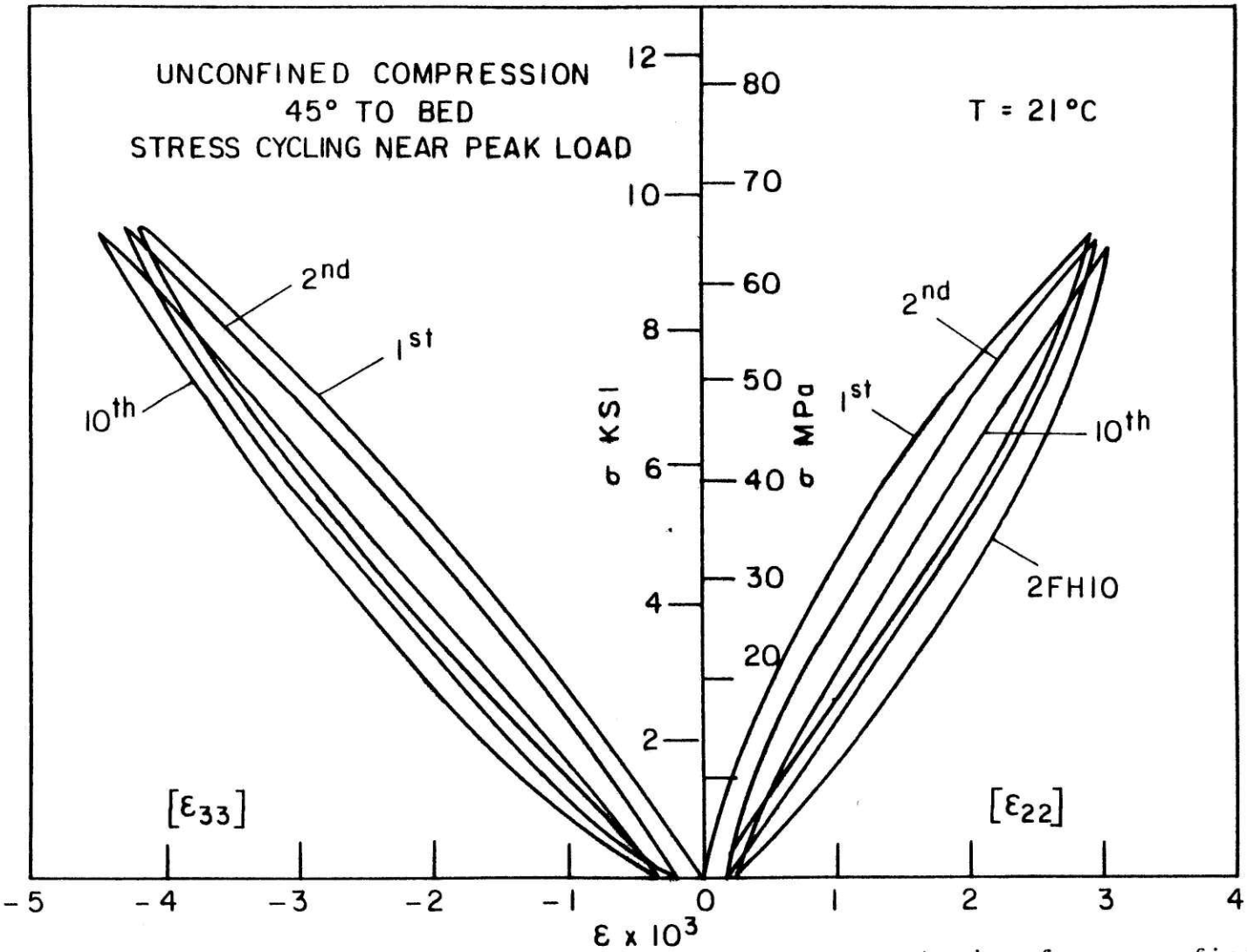

FIGURE 15a: Axial stress vs. axial and transverse strains for unconfined compression 45° to bedding at 21°C for nominal 30 gpt shale. Transverse strain measured in $\underset{\sim}{e}_2$ direction. Compressive stress taken as positive.

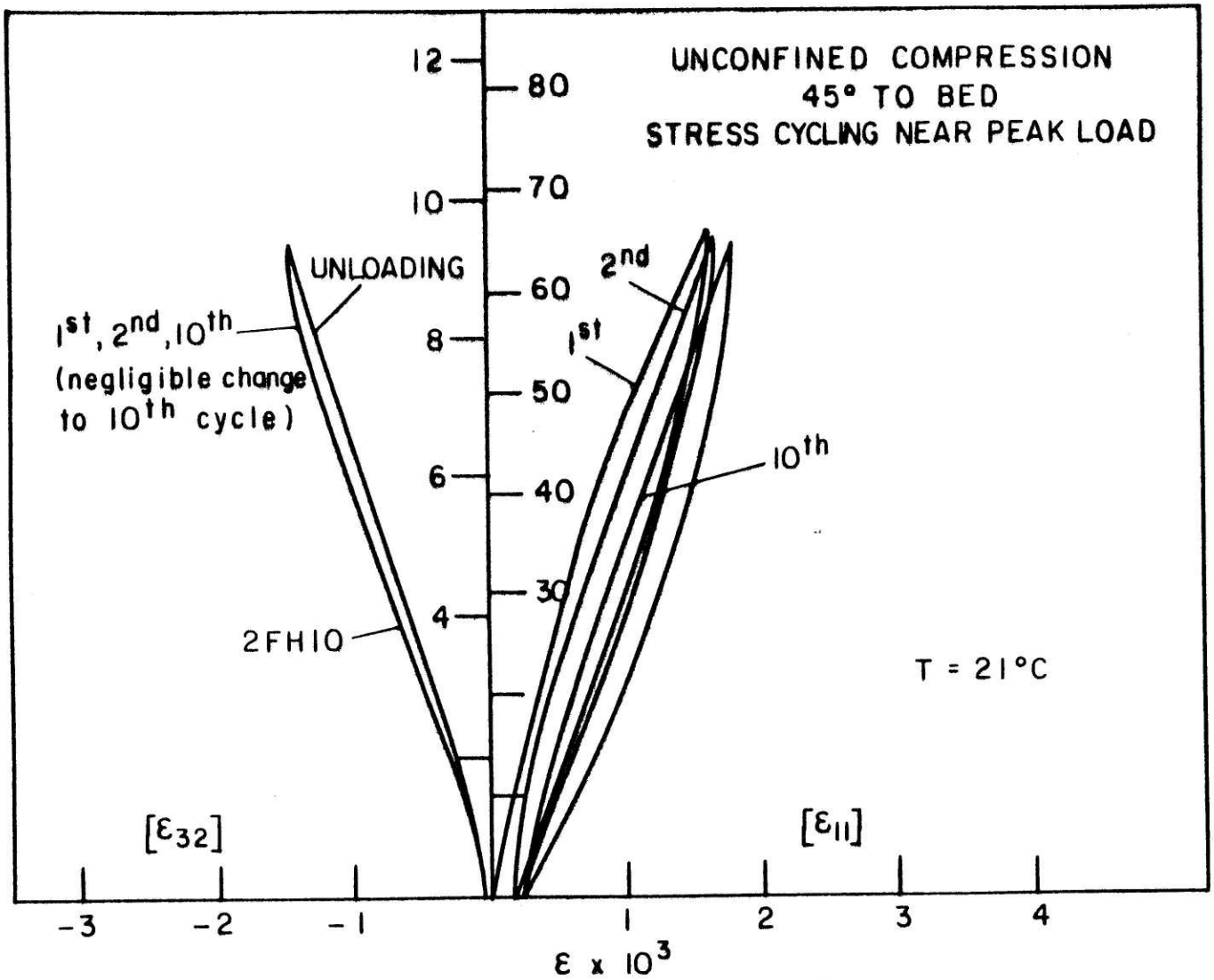

Figure 15b: Axial stress vs. transverse strains for unconfined compression 45° to bedding at 21°C for nominal 30 gpt shale. ε_{32} and ε_{11} strains measured in $\underline{e}_1$ and n directions, respectively. Compressive stress taken as positive.

greatest after one cycle, but that further stress cycling produced minimal hysteresis or work loss.

Additional single cyclings were performed at temperatures of 21°C, 93°C, and 204°C with specimens normal, parallel and 45° to bedding. These experiments, at the various temperatures, included cycling roughly at 20%, 40%, 60% and 80% and failure load; loading was then carried to approximately 90% of total failure strength, held for 30 minutes to monitor stress relief in the core, then released. The results, showing relevant longitudinal and transverse strain responses, are plotted in Figures 16 (a,b,c),17(a,b,c,d), and 18(a,b,c,d) for tests run normal, parallel, and at 45° to the bedding planes, respectively.

Substantial stress relief in the cores was observed in all orientations,even at 21°C. For compression normal to the bedding planes at 21°C, axial stress/strain relief/ increase of approximately 5%/15% of total failure stress/ strain was detected after 30 minutes. These values increased to roughly 20% and 22% for stress and strain, respectively, at 204°C. The transverse strain measurement showed slightly larger increases over temperature. Hysteresis on unloading at 21°C was not detected until 60% of the total failure load was attained, decreasing to about 40% of failure load at 204°C. Similar results were observed for tests parallel and at 45° to bedding. The

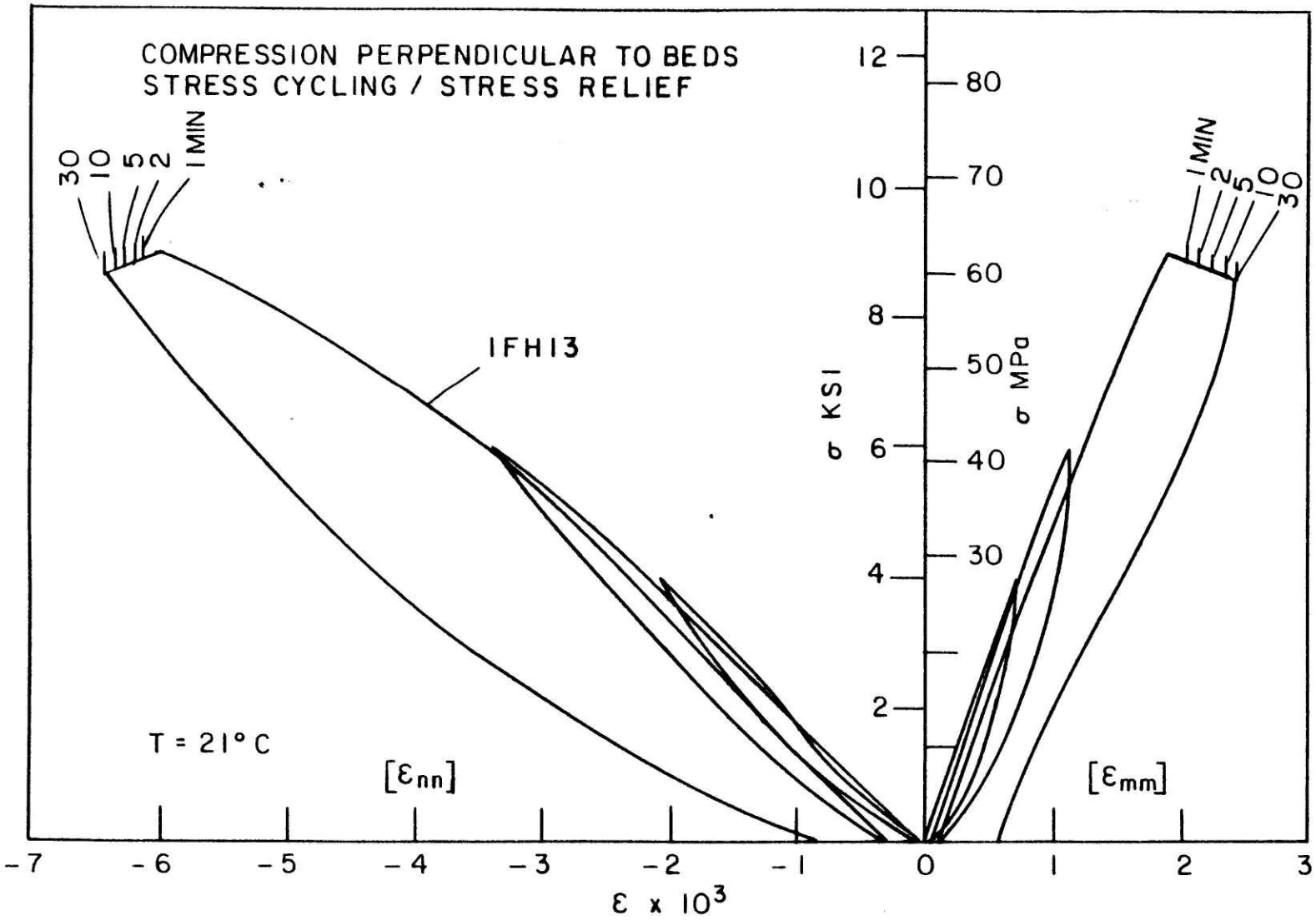

Figure 16a: Axial stress vs. axial and transverse strains at 21°C for cycling and stress relief for unconfined compression normal to bedding. Stress relief at 80% of failure load with one, two, five, ten, and thirty minute increments shown for the nominal 30 gpt shale. Compressive stress taken as positive.

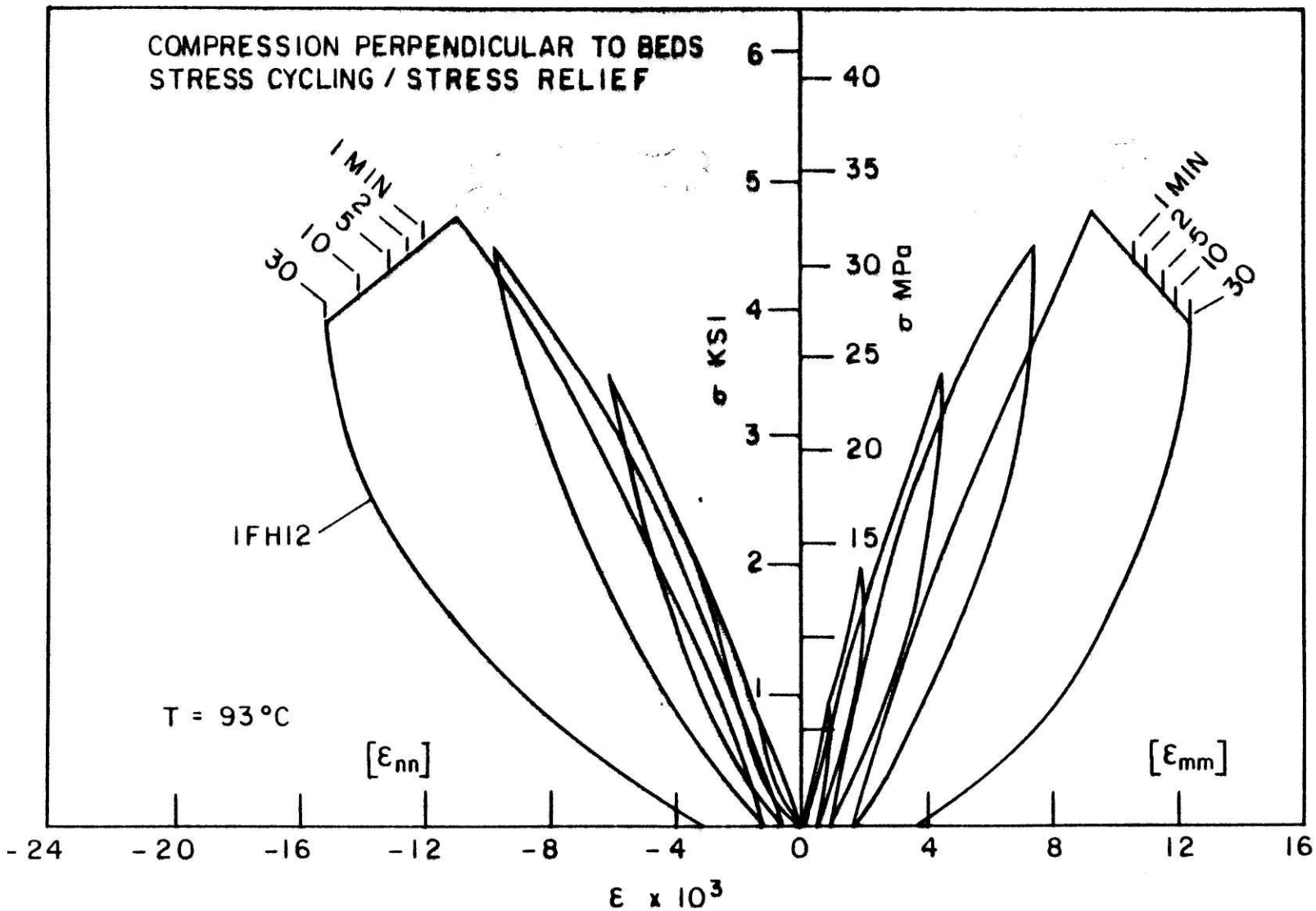

Figure 16b: Axial stress vs. axial and transverse strains at 93°C for stress cycling and relief for unconfined compression normal to bedding. One, two, five, ten, and thirty minute increments shown for nominal 30 gpt shale. Compressive stress taken as positive.

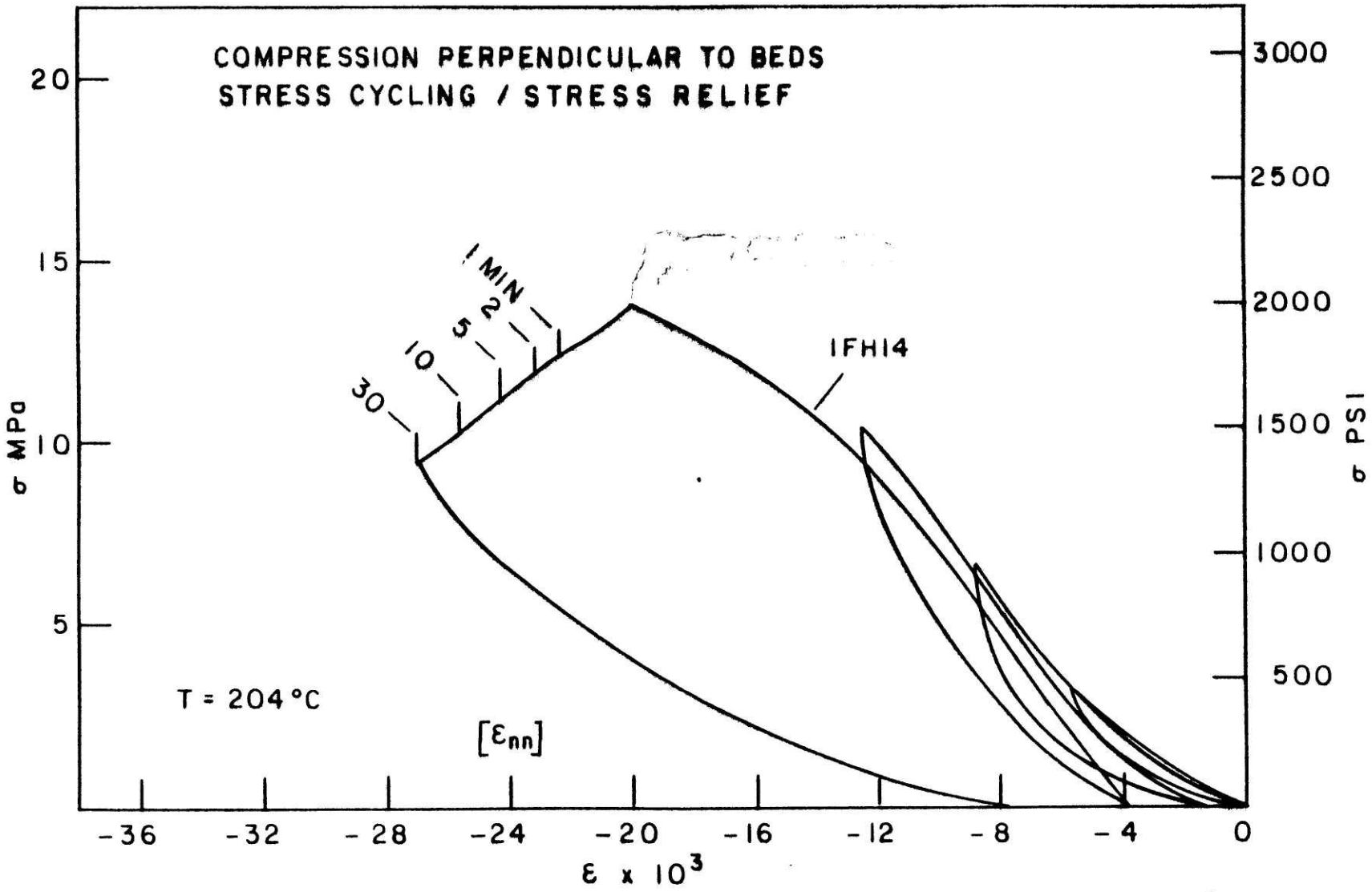

Figure 16c: Axial stress vs. axial strain at 204°C for stress cycling and relief for unconfined compression normal to bedding. One, two, five, ten, and thirty minute increments shown for nominal 30 gpt shale. Compressive stress taken as positive.

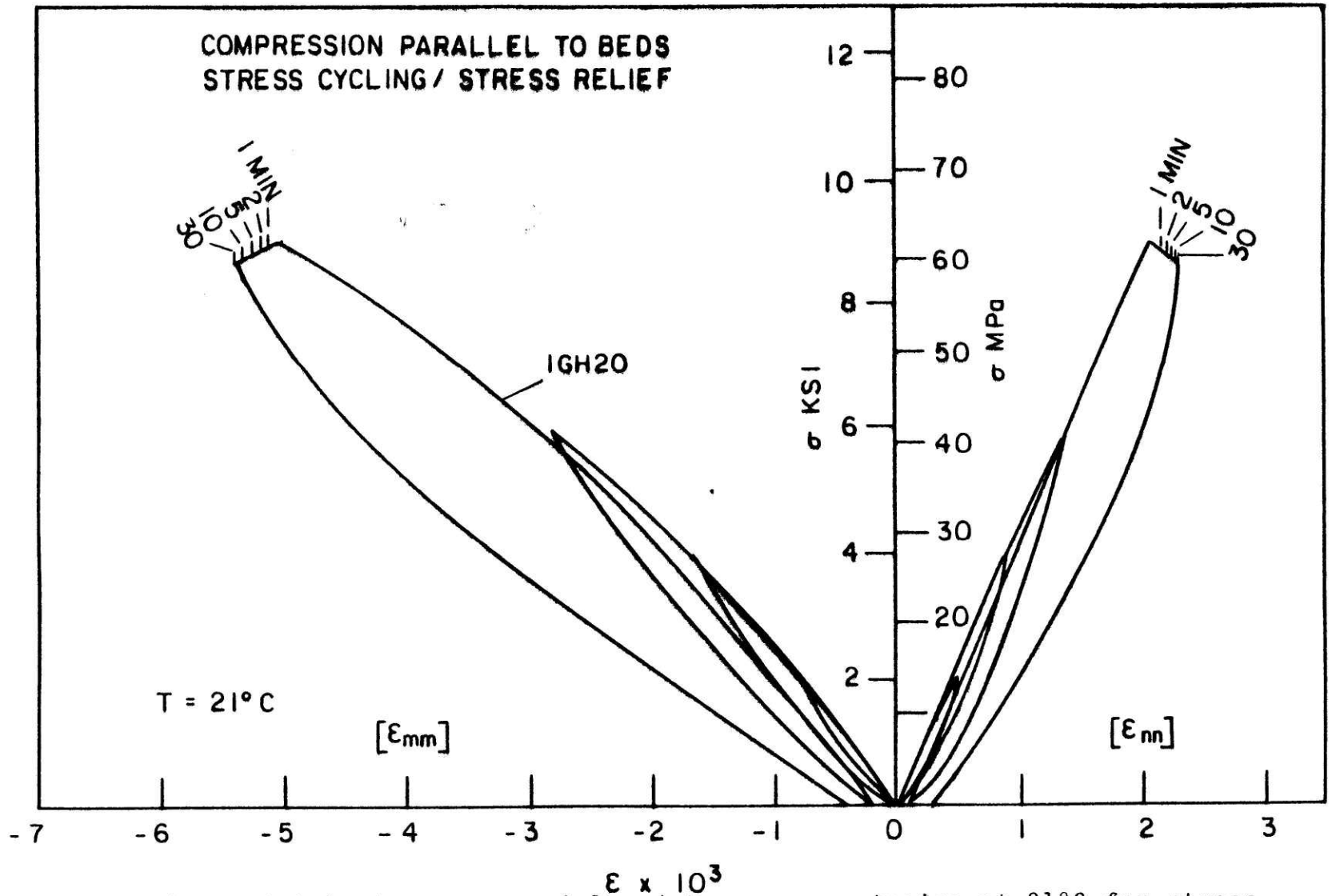

Figure 17a: Axial stress vs. axial and transverse strains at 21°C for stress cycling and relief for unconfined compression parallel to bedding. Transverse strain measured normal to bedding. One, two, five, ten, and thirty minute increments shown for nominal 30 gpt shale. Compressive stress taken as positive.

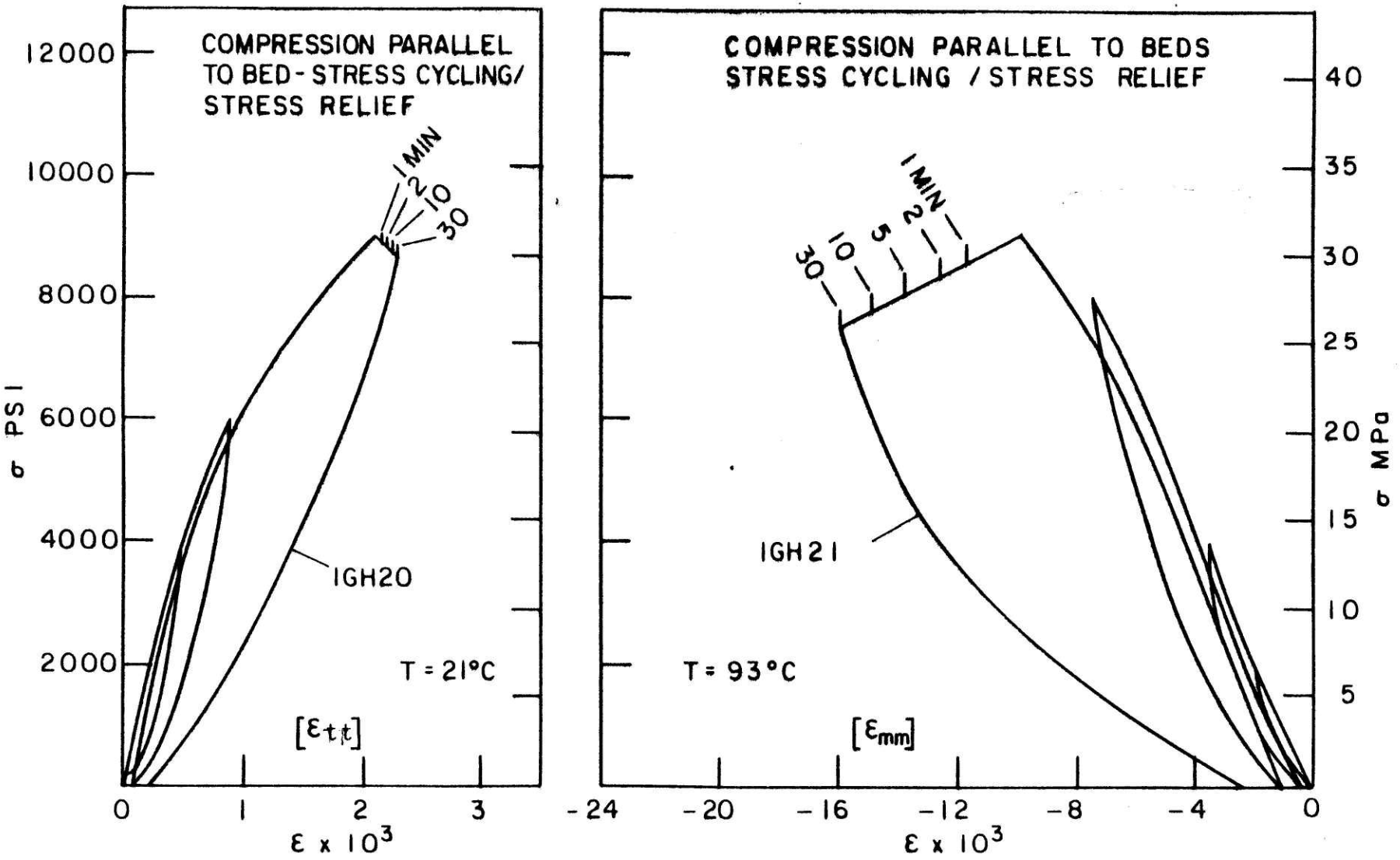

Figure 17b: Axial stress vs. axial (T=93°) and transverse (T=21°) strains for stress cycling and relief for unconfined compression parallel to bedding. Transverse strain measured parallel to bedding for nominal 30 gpt shale. Compressive stress taken as positive.

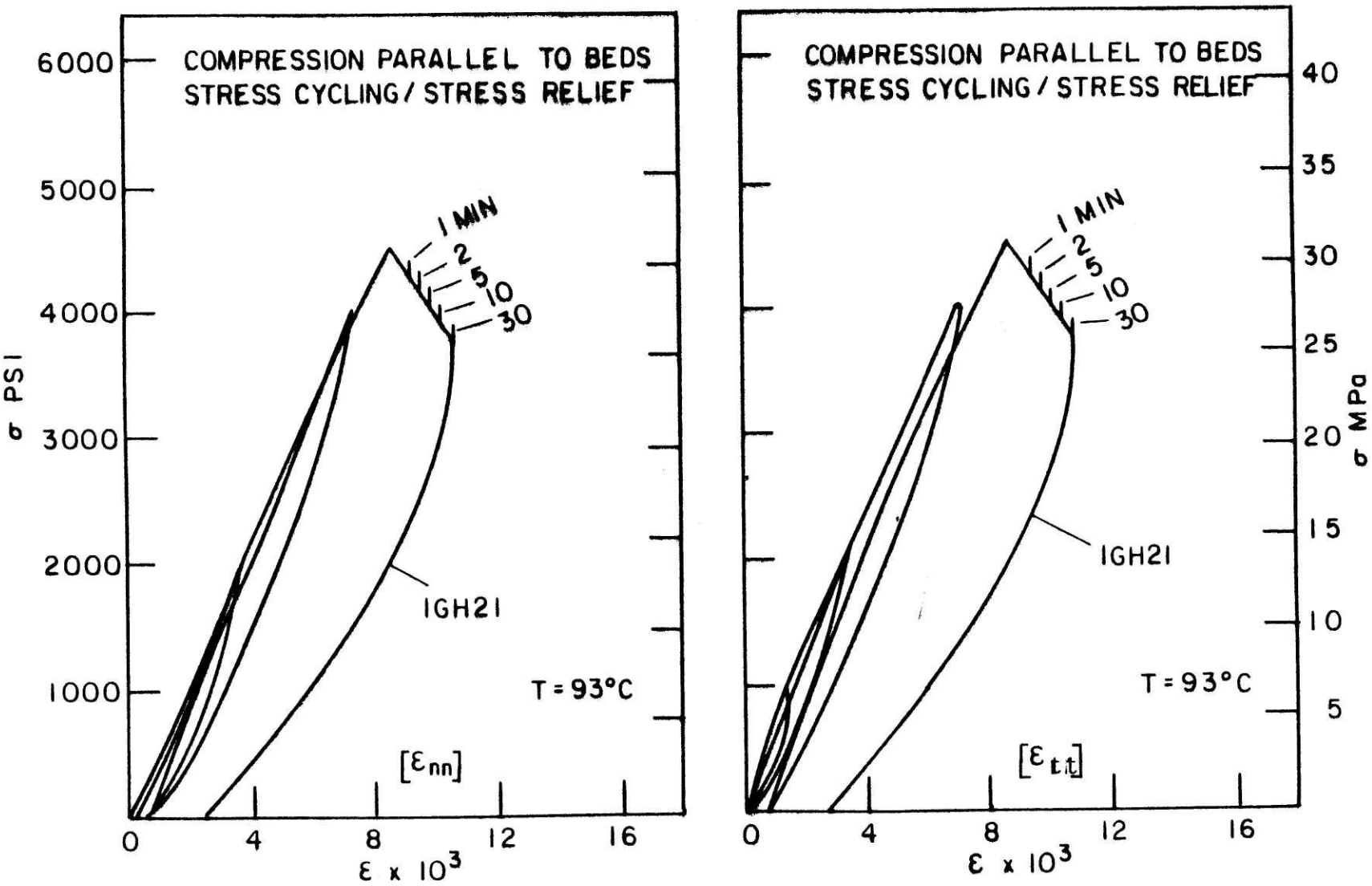

Figure 17c: Axial stress vs. transverse strains at 93°C for stress cycling and relief for unconfined compression parallel to bedding. ε_{nn} and ε_{tt} represent transverse strains normal and parallel to bedding, respectively, for nominal 30 gpt shale. Compressive stress taken as positive.

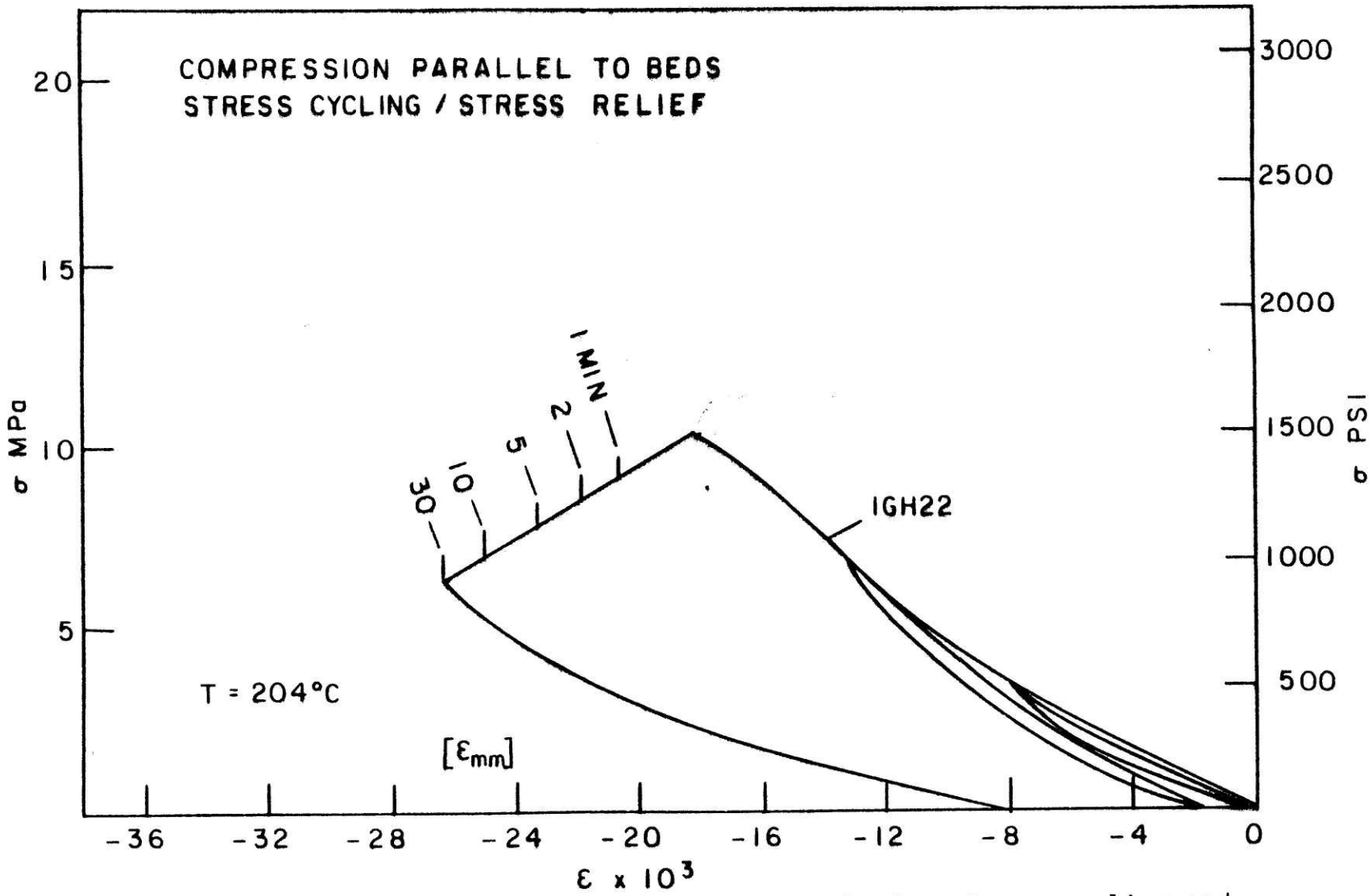

Figure 17d: Axial stress vs. axial strain at 204°C for stress cycling and relief for unconfined compression parallel to bedding. One, two, five, ten, and thirty minute increments shown for nominal 30 gpt shale. Compressive stress taken as positive.

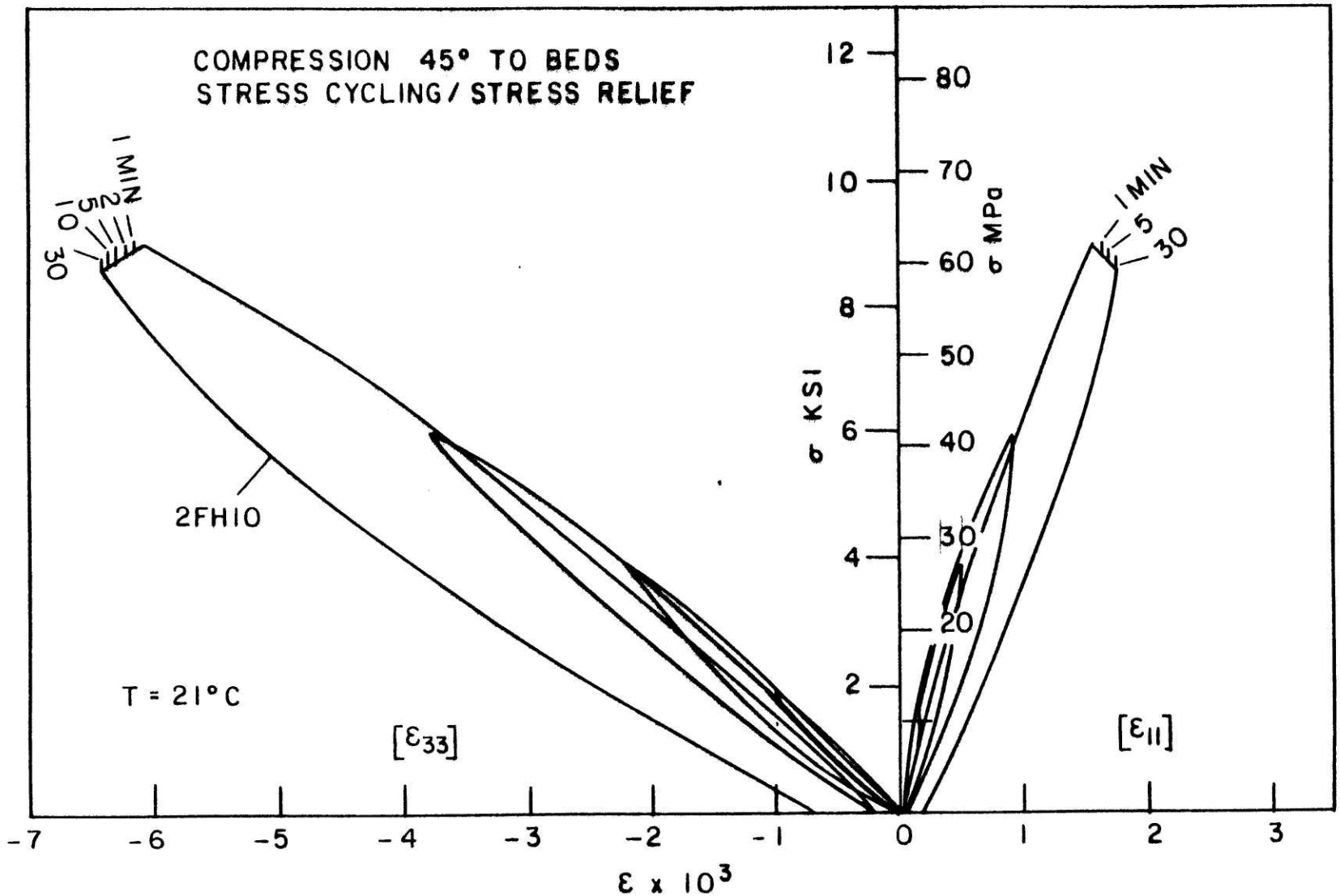

Figure 18a: Axial stress vs. axial and transverse strains at 21°C for stress cycling and relief for unconfined compression at 45° to bedding. Transverse strain $\tilde{\varepsilon}_{11}$, measured in e_1 direction for nominal 30 gpt shale. Compressive stress taken as positive.

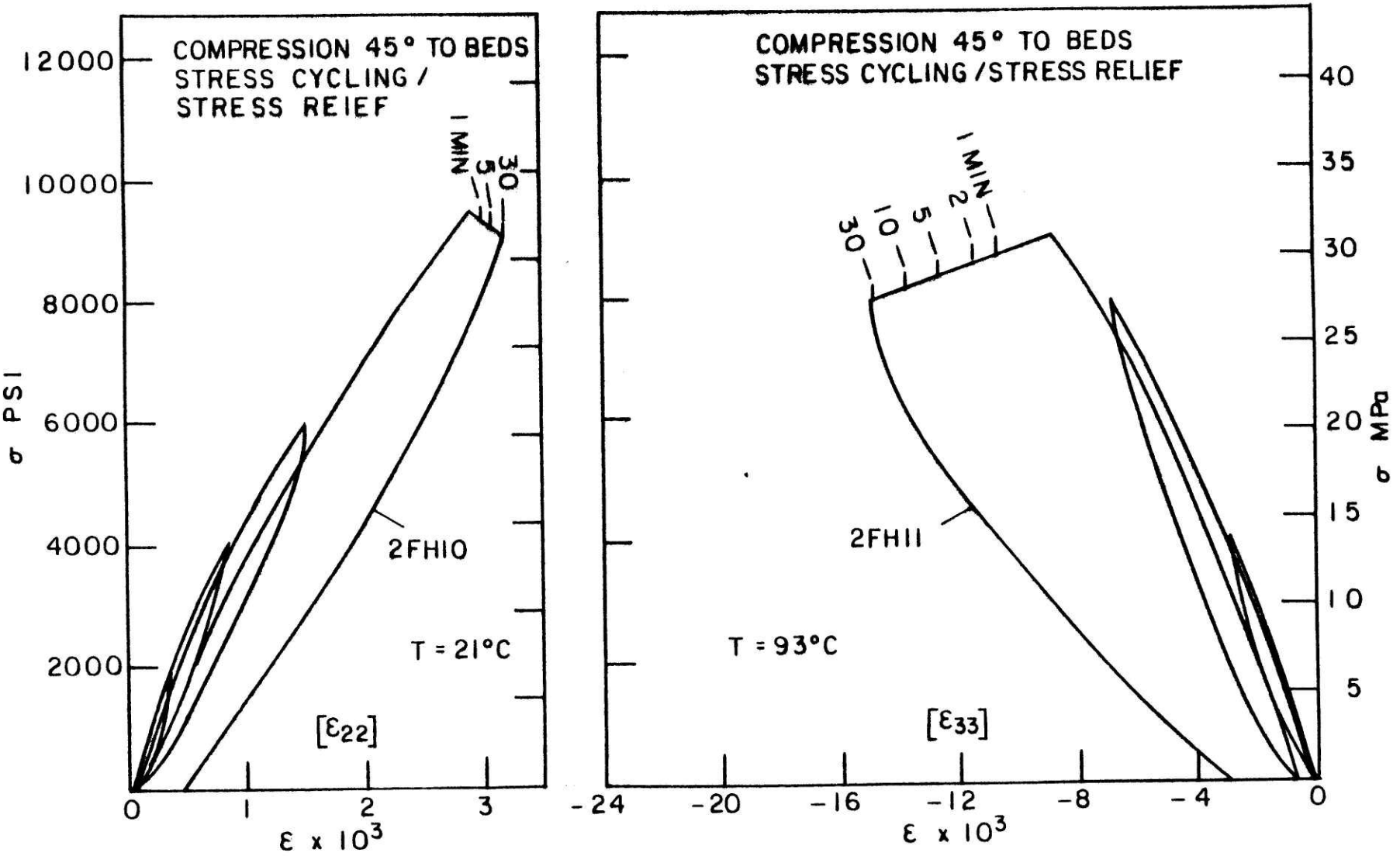

Figure 18b: Axial stress vs. axial (T=93°C) and transverse (T=21°C) strains for stress cycling and relief for unconfined compression 45° to bedding. Transverse strain, ε_{22}, measured in e_2 direction for nominal 30 gpt shale. Compressive stress taken as positive.

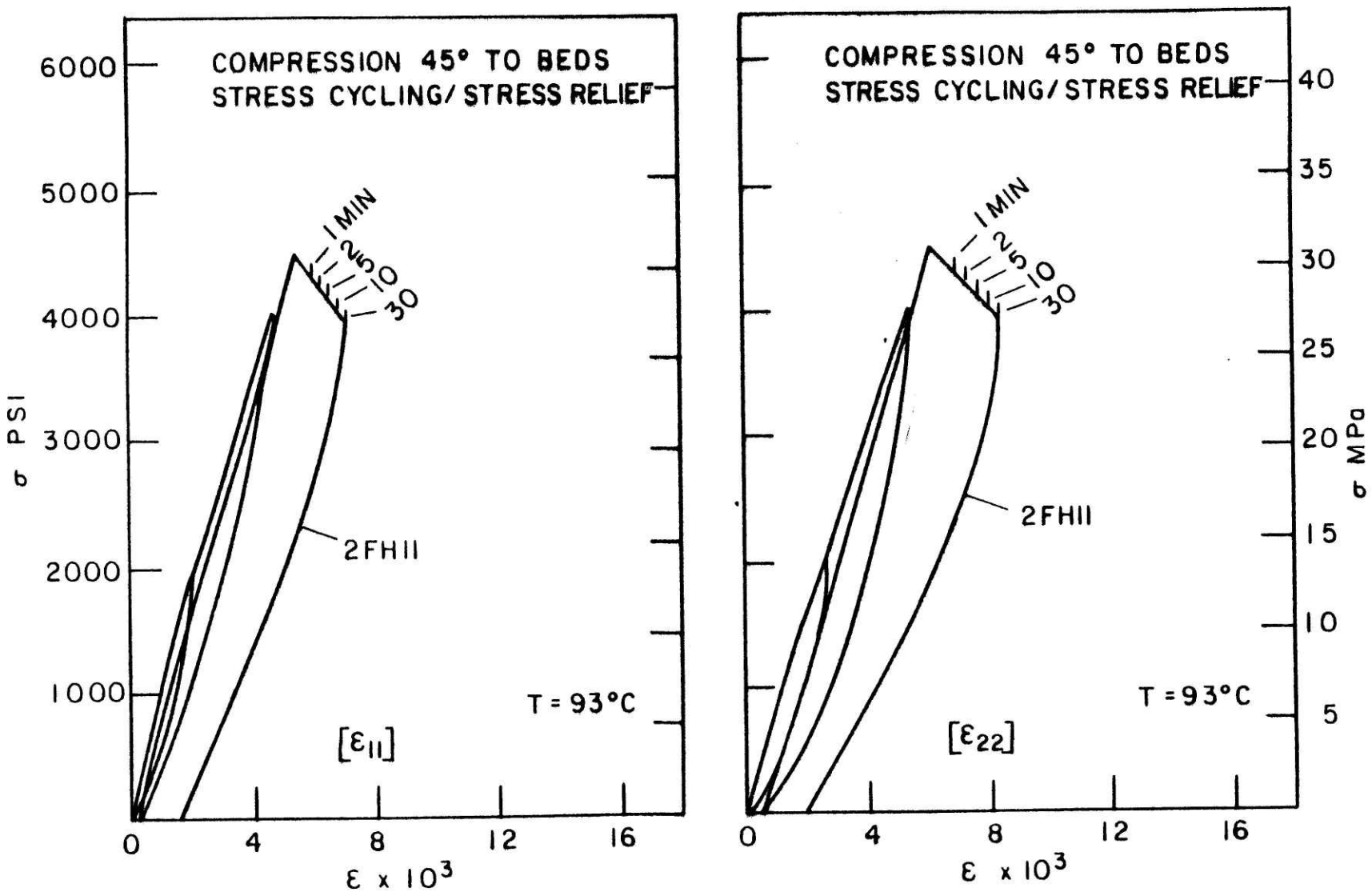

Figure 18c: Axial stress vs. transverse strains at 93°C for stress cycling and relief for unconfined compression 45° to bedding. ε_{11} and ε_{22} represent transverse strains measured in $\underset{\sim}{e}_1$ and $\underset{\sim}{e}_2$ directions, respectively, for nominal 30 gpt shale. Compressive stress taken as positive.

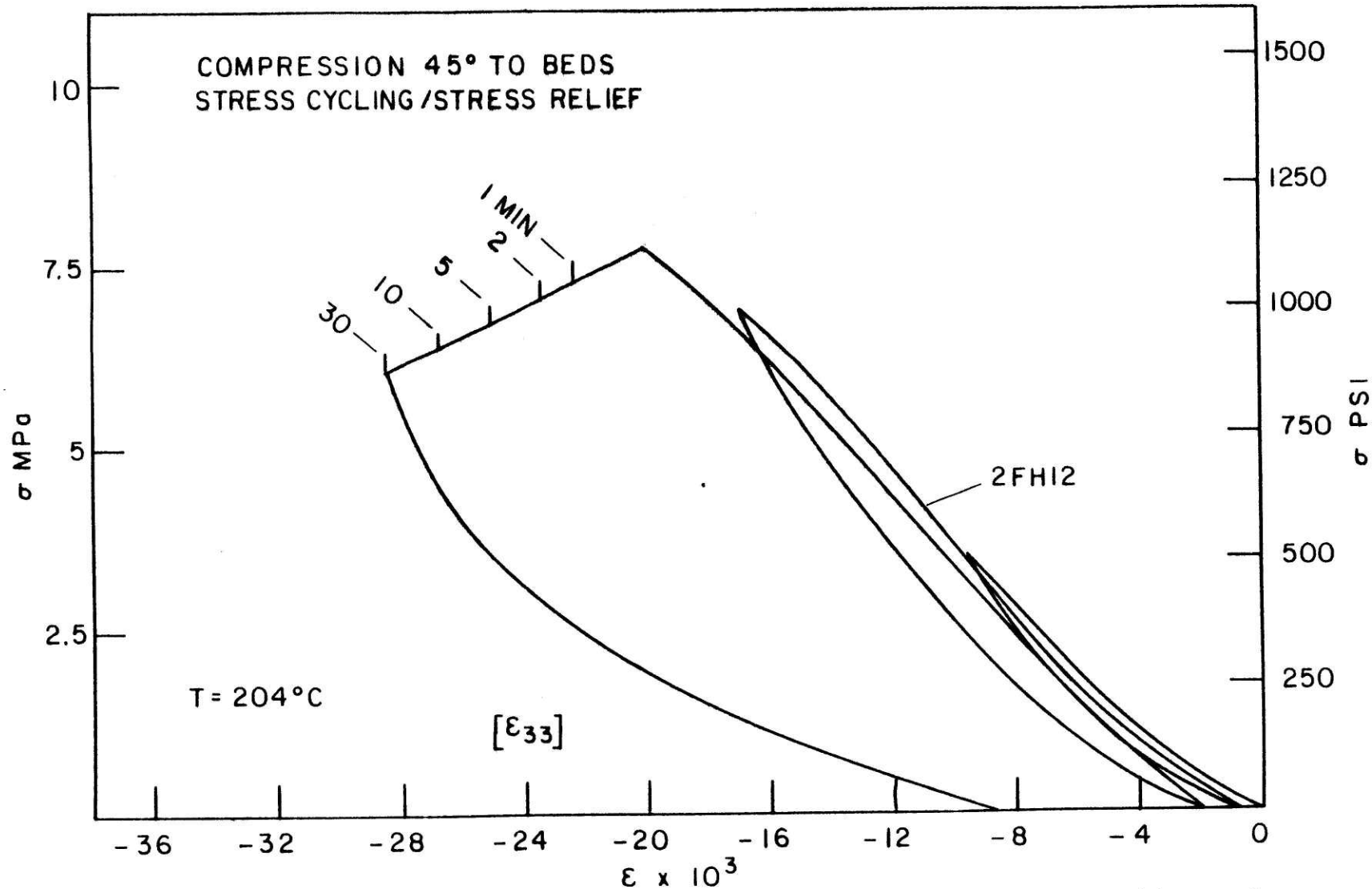

Figure 18d: Axial stress vs. axial strainat 204°C for stress cycling and relief for unconfined compression 45° to bedding. One, two, five, ten and thirty minute increments shown for nominal 30 gpt shale. Compressive stress taken as positive.

greatest hysteresis during cycling at room temperature was again found in samples normal to the bedding planes, with tests at $\theta = \pi/4$ exhibiting the least hysteresis on unloading. However, as temperatures increased (to 204°C), tests in the 45° orientation were observed to have the largest hysteresis on unloading, indicating not only increased inelastic deformation due to organic breakdown, but also an additional inelastic sliding component found in this orientation. This argument pertains also to stress relief in the tests; 45° cores displayed the least stress relief at 21°C, probably due to an additional frictional restraint between the beds which prevented crack growth in this direction, while exhibiting the most relief at 204°C, due to the above reasoning.

These results-multiple stress cycling near peak load, intermediate stress cycling, and stress relief near peak load - all suggest substantial stress-induced anisotropies in the oil shale. The effects of the kerogen on material response, particularly at higher temperatures, reveals the very complex nature of the shale. Further tests are warranted introducing confinement, with temperature, to more closely simulate underground conditions during in situ retorting.

D. Triaxial Tests. Triaxial testing was performed, in a fashion described more fully in Appendix VI, to determine the effect of confining pressure on initial moduli, strength and strain data, and fracture mechanisms. The results, for triaxial tests normal and parallel to the bedding are presented in Figures 19 and 20, respectively. Strain was measured in the axial direction only because the specimens were jacketed with vinyl tubing prior to testing (see Appendix VI). All experiments were run at room temperature. Further triaxial experiments at higher temperatures using larger cores with appropriate strain measurements are planned in later research.

Specific results for failure strengths/strains and initial tangent moduli are listed in Table VI. Three-fold increases in failure strengths were found for tests in both principal directions over the range of applied confining pressure (0 MPa to 69 MPa). Initial tangent moduli at zero confining pressure were comparable to those presented previously in this study, again revealing crack closure response at load initiation. However, since confining pressure was applied first before axial loading, this initial response had already occurred for tests with confinement greater than atmospheric pressure. Consequently, tangent moduli values were generally twice the magnitude

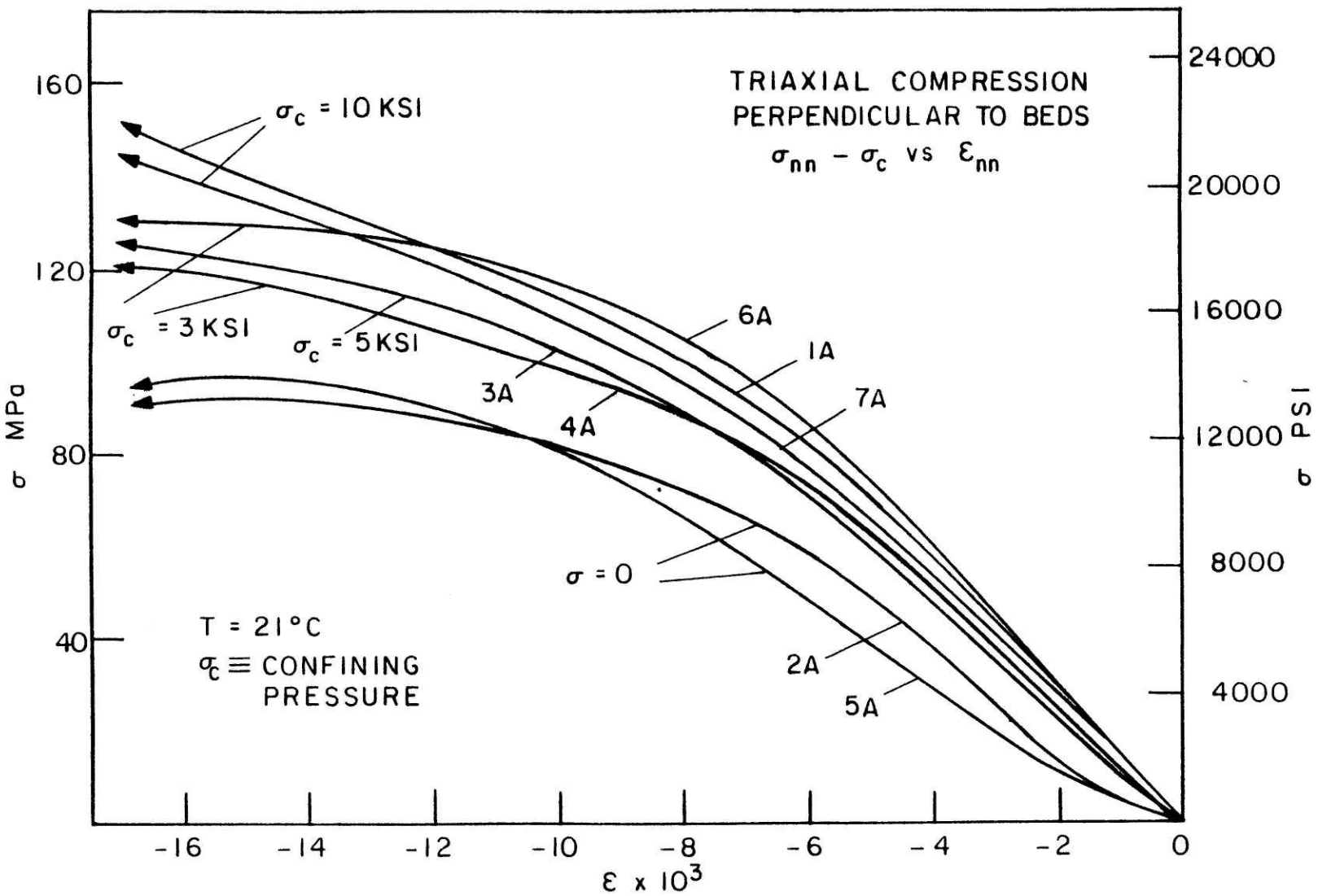

Figure 19: Deviatoric stress vs. axial strain for triaxial compression perpendicular to bedding at 21°C for nominal 30 gpt shale. Plots are 0, 3 ksi, 5 ksi and 10 ksi confining pressure are shown. Compressive stress taken as positive.

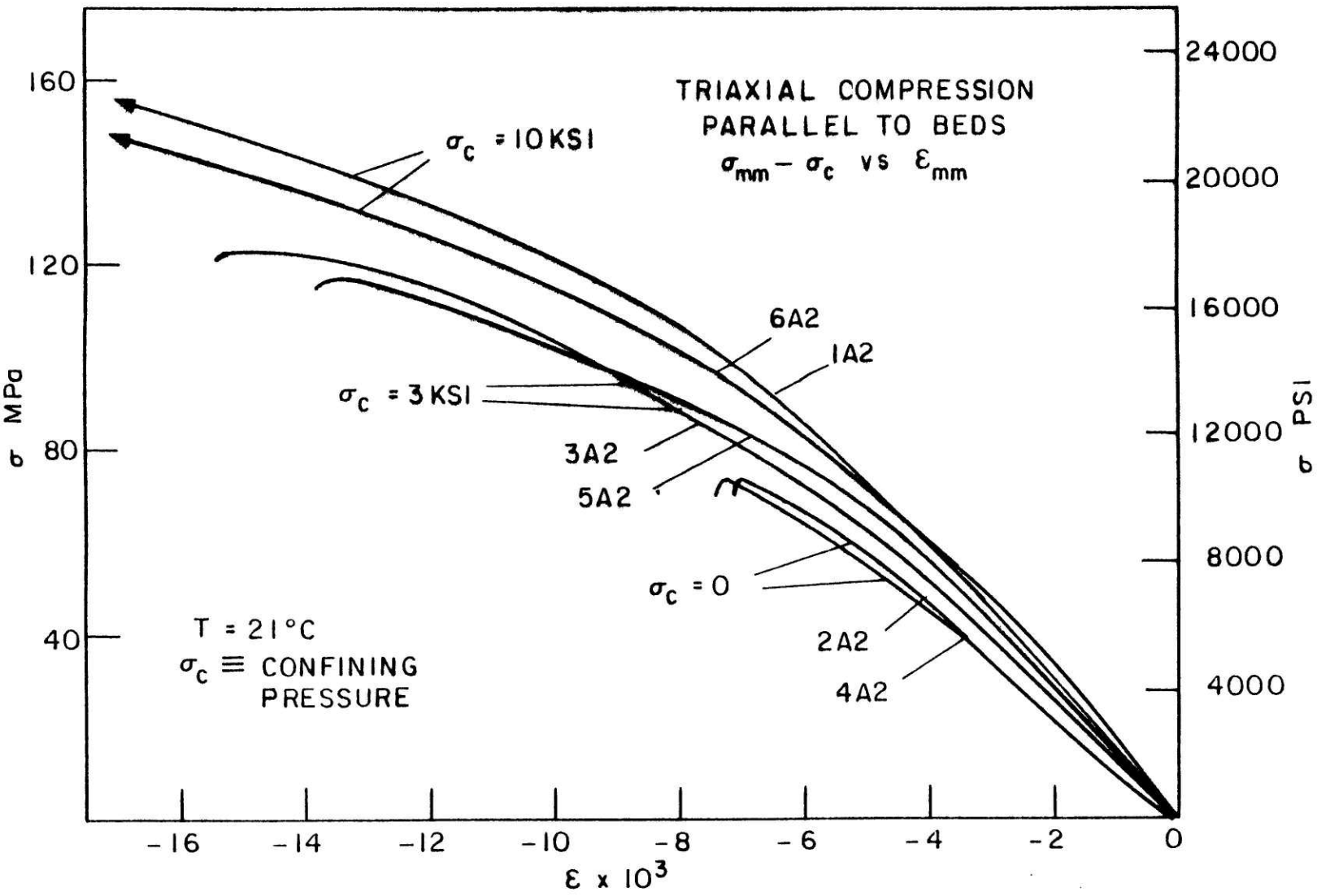

Figure 20: Deviatoric stress vs. axial strain for triaxial compression parallel to bedding at 21°C for nominal 30 gpt shale. Plots for 0, 3 ksi, and 10 ksi confining pressure are shown. Compressive stress taken as positive.

TABLE VI

INITIAL TANGENT MODULI AND FAILURE STRENGTHS AND STRAINS VERSUS CONFINING STRESS FOR NOMINAL 30 GPT SHALE AT AMBIENT TEMPERATURE

# Tests	Core Orientation	Confining Stress - MPa (psi)		Modulus E_{nn} GPa (psi)		Failure σ_A^* MPa(psi)		ε_{nn} me
2	⊥	0.1	(15)	6.3	(9.2×10^5)	94.5	(13700)	18
2	⊥	20.7	(3000)	13.8	(2.0×10^6)	147	(21300)	20
2	⊥	34.5	(5000)	11.0	(1.6×10^6)	179	(26000)	64
2	⊥	69.0	(10000)	15.9	(2.3×10^6)	257	(37200)	>125
				E_{mm}				ε_{mm}
2	//	0.1	(15)	7.6	(1.1×10^6)	73.8	(10700)	71
2	//	20.7	(3000)	14.5	(2.1×10^6)	141	(20400)	15
2	//	69.0	(10000)	17.9	(2.6×10^6)	233	(33800)	>110

*σ_A ≡ total applied axial stress

of those at zero confining stress. The moduli remained essentially constant then, for increase of confining pressure, up to 69 MPa (10,000 psi), suggesting a flaw-free character in the bedding planes. The substantial increases in strength and overall deformation to failure at confining stresses of just 20 MPa indicate a very high inherent toughness in oil shale. This toughness or resistance to failure suggest that high energy expenditures may be required for sufficient zone preparation (e.g., excavation access, fracturing) and maintenance during the retort stage. Similar tests at higher temperatures (to be performed in future work), are, therefore, quite important and should give much needed information.

1. Fracture Characterization. Several failed triaxial samples in both principal directions, with respect to bedding, are pictured in Figure 21. For tests parallel to the bedding planes, the failure behavior at confining stresses up to 2.07 MPa (3000 psi) was similar to that detailed for uniaxial compression testing, i.e., wedge-shape diagonal fractures traversing the specimens from top to bottom, with minimal associated barrelling. Some delamination cracking was detected near the top and bottom edges of the larger primary fracture (Figure 21). At 69 MPa (10,000 psi) pressure, severe barrelling and extremely large axial and lateral deformations were

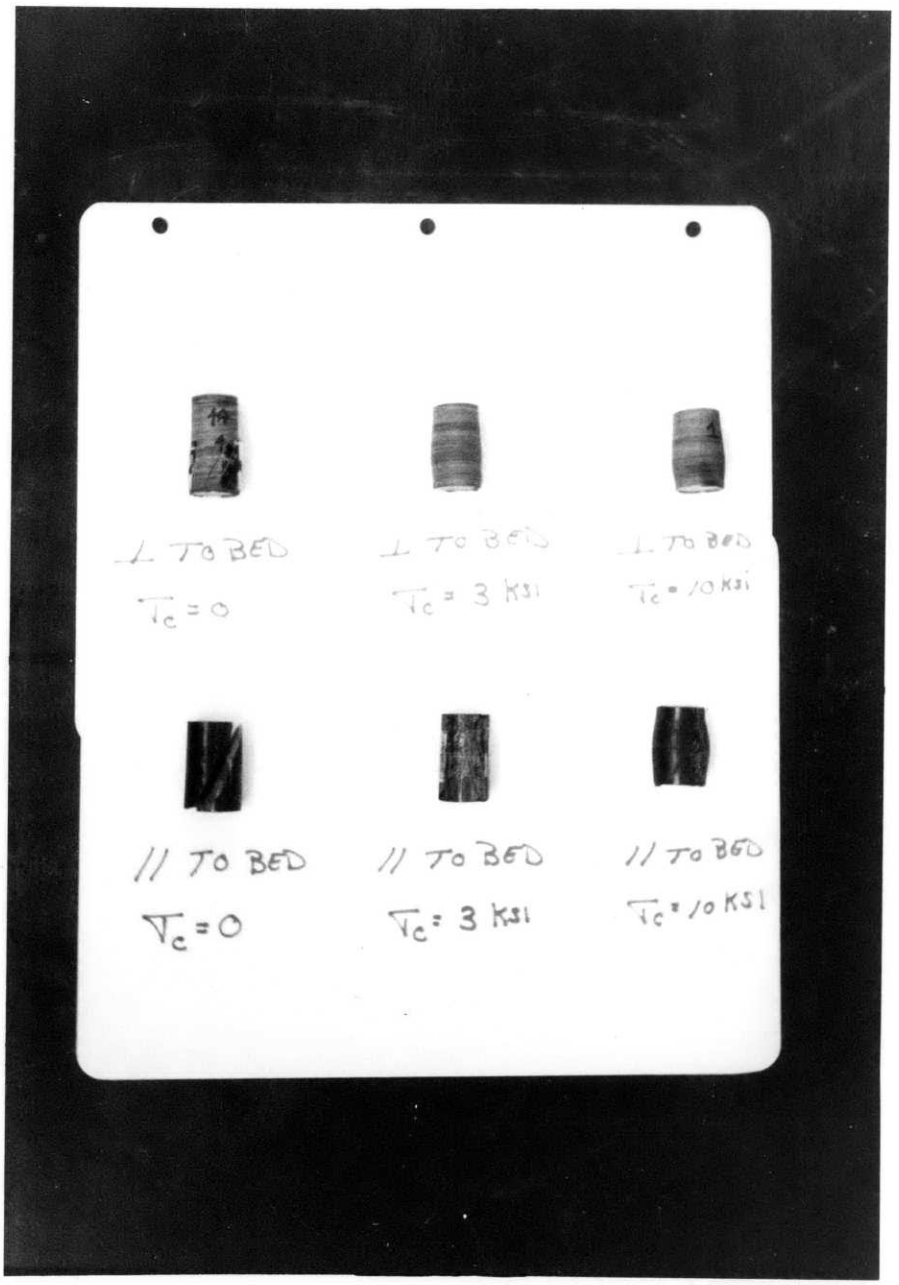

Figure 21: Nominal 30 gpt specimens failed in triaxial compression at 21°C. // and ⊥ refer to tests parallel and normal to beds, respectively.

observed. The high confinement produced a dual-wedge or x-shape failure pattern in the shale. Full failure of these particular specimens was actually not attained due to an equipment limitation (maximum ram travel), but total axial deformations to complete failure of 20-25% of original core length were indicated.

Analogous results were found for triaxial tests on cores cut normal to the beds. To 20 MPa (3000 psi), cone-like end failures (due to triaxiality) were observed, again similar to uniaxial tests. However, for runs at confining stresses greater than 20 MPa (up to 69 MPa), these cone-like fractures were accompanied by extreme barrelling and lateral straining (Figure 21). The resultant axial deformations (estimated at strains of .25 to failure) were due to high circumferential stresses and very high end frictional stresses produced by applied stresses greater than 250 MPa (37000 psi).

E. High Temperature Fracture Toughness Measurements

1. Preparatory descriptions. A fracture criterion which could accurately predict failure of cracked bodies would be an extremely useful engineering tool, with immeasurable value to the areas of mechanics and materials science (e.g., for evaluation of structural integrity, selection of

materials, mining technology, etc.). In particular, a clear understanding of the mechanics of fracture processes in oil shale is critical from an engineering standpoint if one is to predict and therefore optimize the preparatory and retorting techniques of the in situ process. As discussed earlier in Section 1, sufficient permeability for efficient pyrolysis of the kerogen must be established (e.g. hydraulically, explosively or chemically) and maintained for high recovery efficiency throughout the entire procedure. Adequate knowledge is therefore required to the effects of kerogen content, in situ stress state, crack tip environment, and bed orientation on crack initiation and propagation. Optimal procedures could hopefully then be formulated to minimize the overall required energy input and, for instance, thereby reduce the costs or environmental hazards of the system. Thus, an effective toughness criterion would be a valuable measure to quantify the shale's resistance to crack initiation, propagation, and subsequent formation of fractured zones.

Although there exist several methods for determining the fracture toughness of a material*, the J-integral technique (Rice, 1968, Wilkening, 1976) utilizing deeply notched specimens in a "compact tension" geometry (see Figure 1) was employed. Mode I stressing at the specimen front end subjected the remaining uncracked

*Others are discussed in a later section.

ligament to remotely applied in-plane bending. In this geometry, an approximate evaluation of the J-integral was obtained directly from load versus load-point displacement. In this configuration the uncracked load point displacements are negligible by comparison to those caused by presence of the crack. Thus, there is only a single relevant characteristic dimension in the plane (namely, the uncracked ligament width - b), in the limit as a/w approaches unity. Rice, et al. (1973) have shown that the J-integral has the following limiting form:

$$J = \frac{2}{Bb} \int_0^{\delta_c} F \, d\delta \qquad (1)$$

where b is the ligament width, B the specimen thickness, F the applied load, and δ the load point displacement. The energy available for crack propagation at any critical load-point displacement δ_c, is therefore just proportional to the area under the load-displacement curve. A distinct advantage of the J-integral method is that δ_c can be chosen at any critical value observed in the actual experiment. Values of the J-integral were calculated at maximum load and also computed for a point (e.g., Wilkening, 1976) at which the actual load point displacement was 2% higher (as determined graphically) than predicted from a power law which precisely fitted the initial portion of the P-δ curve.

This power law has the form:

$$\delta = C_0 F + K(C_0 F)^m \qquad (2)$$

where C_0 is the zero load compliance, and K and m are empirical constants resulting from the specimen geometry and constitutive behavior of the shale*. As mentioned by Wilkening (1976), the method chosen to ascertain δ_c is arbitrary, especially for curves without obvious deviations from smooth response. Limitations on this method and its applicability for oil shale at high temperature will be discussed later.

2. <u>High Temperature Results and Discussion.</u> Test specimens were nominally 12 cm x 12 cm with an average a/w ratio of .6. All tests were run on the nominal 30 gpt shale, stabilized at temperature for one hour, and loaded at roughly 80 newtons (18 lbs) per minute (lower at higher temperatures). Load-displacement curves for the three relevant orientations (divider, short transverse, arrester) are presented in Figures 22, 23, and 24. Point A in the figures was the point of significant departure

*The procedure for calculating C_0, K, and m values from the P-δ plots is discussed in Appendix V.

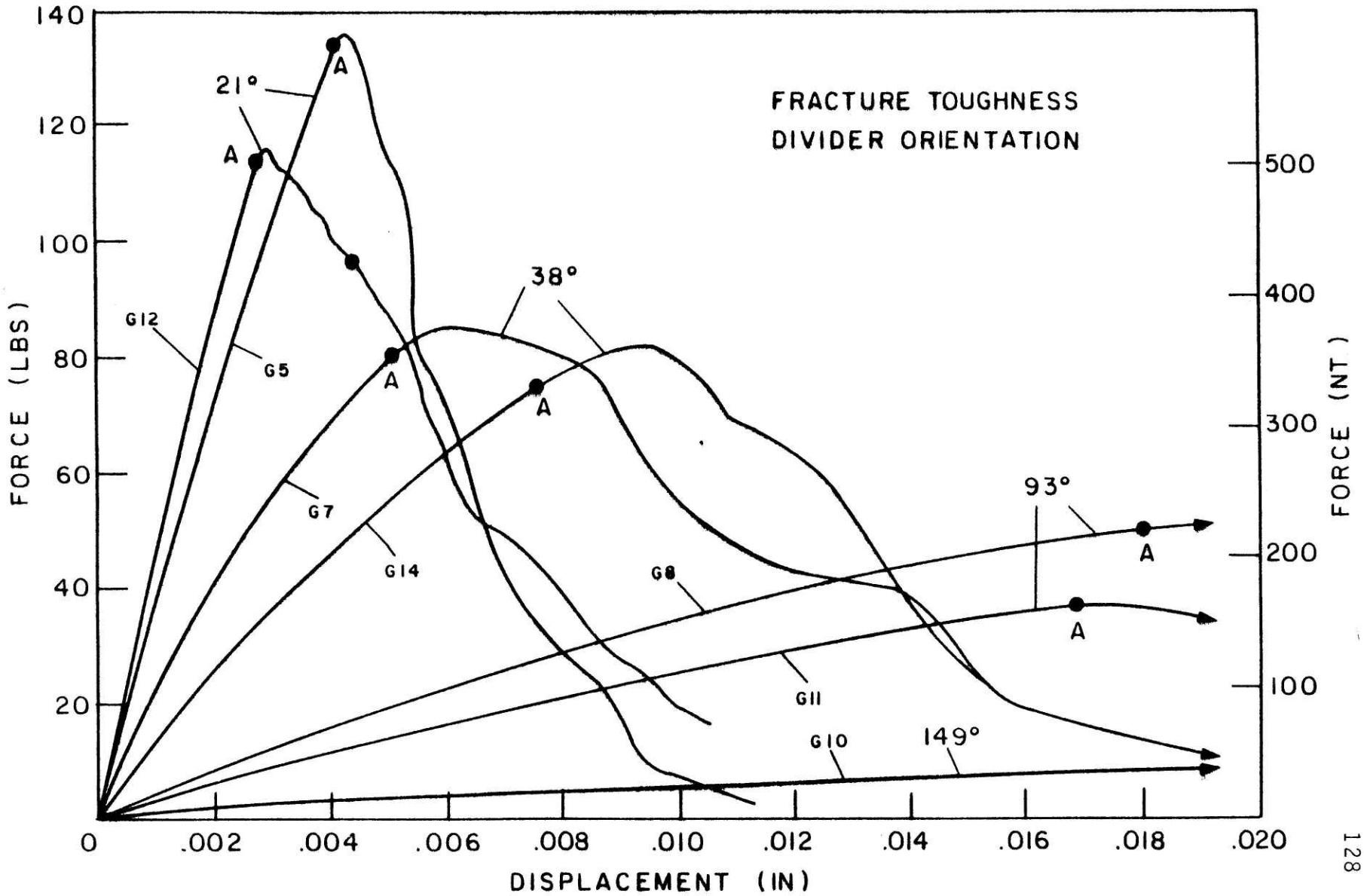

Figure 22: Load vs. load-point displacement plot for compact tension specimen in the divider orientation. Pt. A refers to point of 2% deviation from power law for nominal 30 gpt shale at various temperatures.

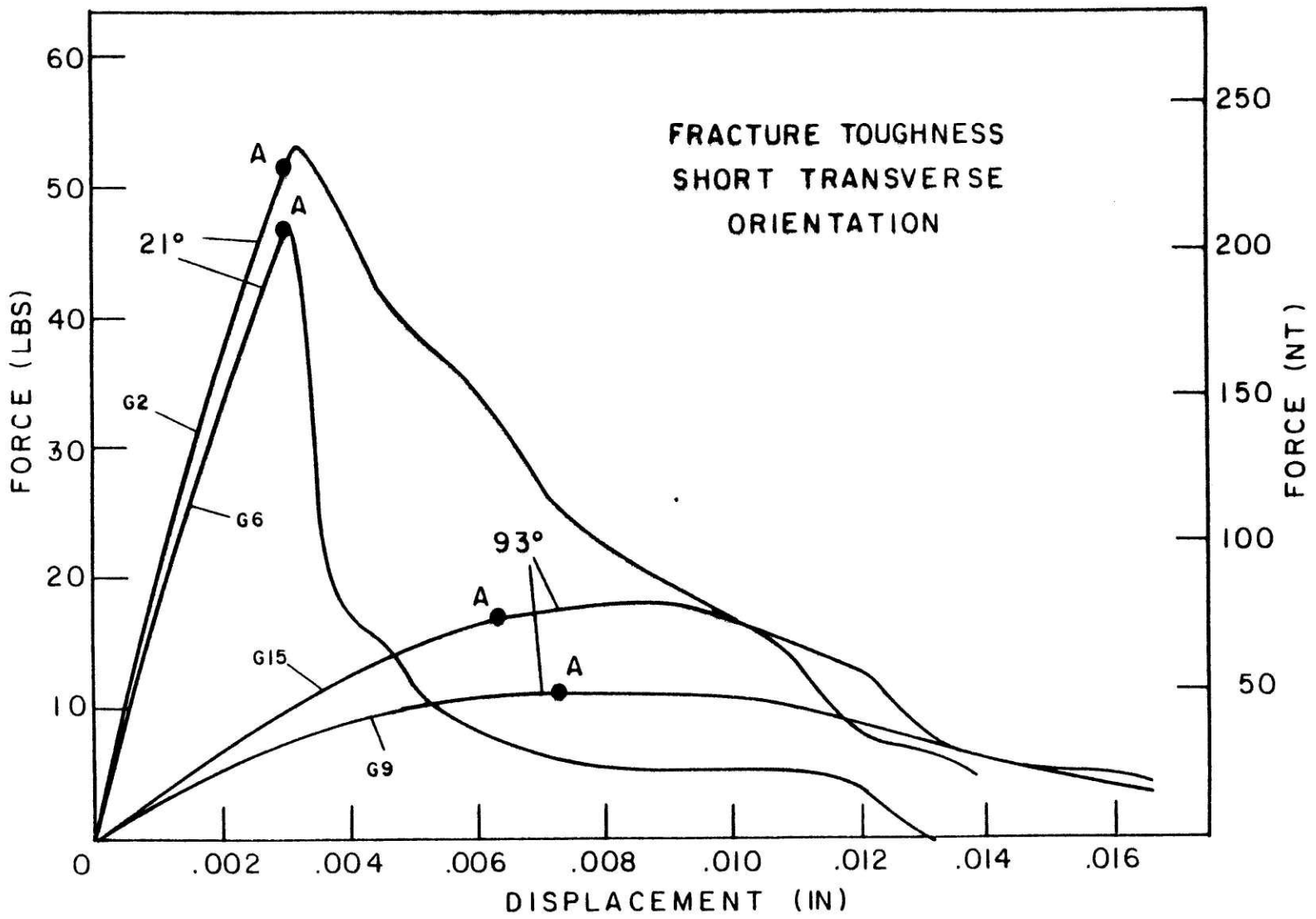

Figure 23: Load vs. load-point displacement plot for compact tension specimens in the short transverse orientation. Pt. A refers to point of 2% deviation from power law for nominal 30 gpt shale at various temperatures.

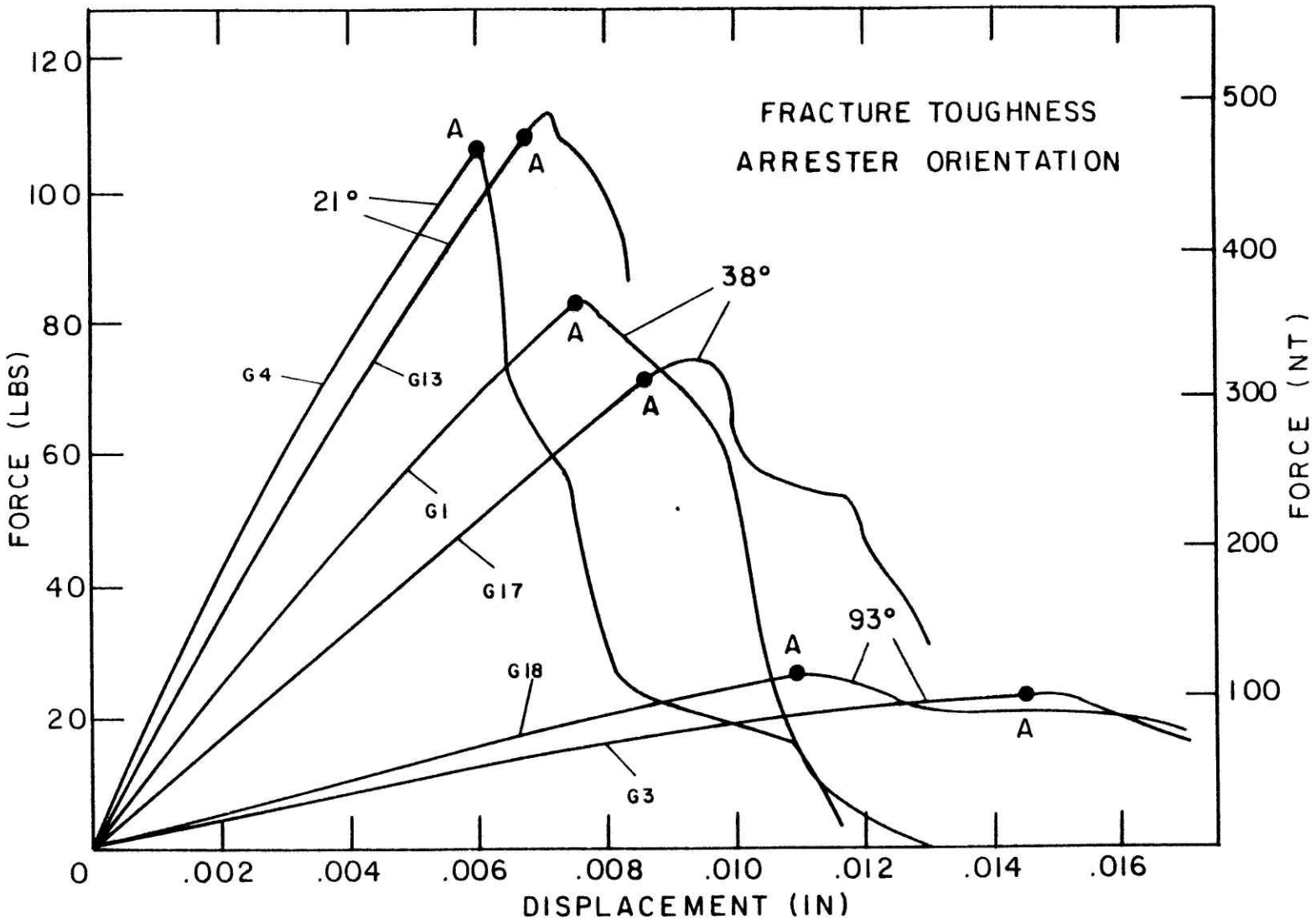

Figure 24: Load vs. load-point displacement plot for compact tension specimens in the arrester orientation. Pt. A refers to point of 2% deviation from power law for nominal 30 gpt shale at various temperatures.

(i.e., 2% deviation) from the power law in Eqn. (2) and was assumed to be indicative of crack initiation at the notch tip. Since C_0 and K were both strong functions of notch depth, any notch depth increase produced significant deviations from the power law. Visible determination at higher temperatures of minute cracks protruding into the ligament area, as described by Hangen (1977), was impossible because of specimen enclosure in the environmental chamber.

To eliminate crack branching into the weak vertical planes in the arrester orientation, a precompression device (to which the compact tension geometry lends itself very readily) was employed to apply a simulated overburden stress condition. The results are plotted in Figure 25.

The results indicated that the divider orientation was toughest at maximum load over the temperature range (21°C to 149°C), but it was comparable to the arrester (unconfined) at the onset of crack growth, up to 38°C (100°F). The short transverse tests exhibited the lowest toughness values in both instances (up to 93°C), as anticipated. Vertical failure along a weak plane normal to the crack front was prevalent in the arrester tests, resulting in particularly low toughnesses as the temperature was increased. In this orientation, a marked decrease in toughness, from 38°C to 93°C suggested a gross lowering

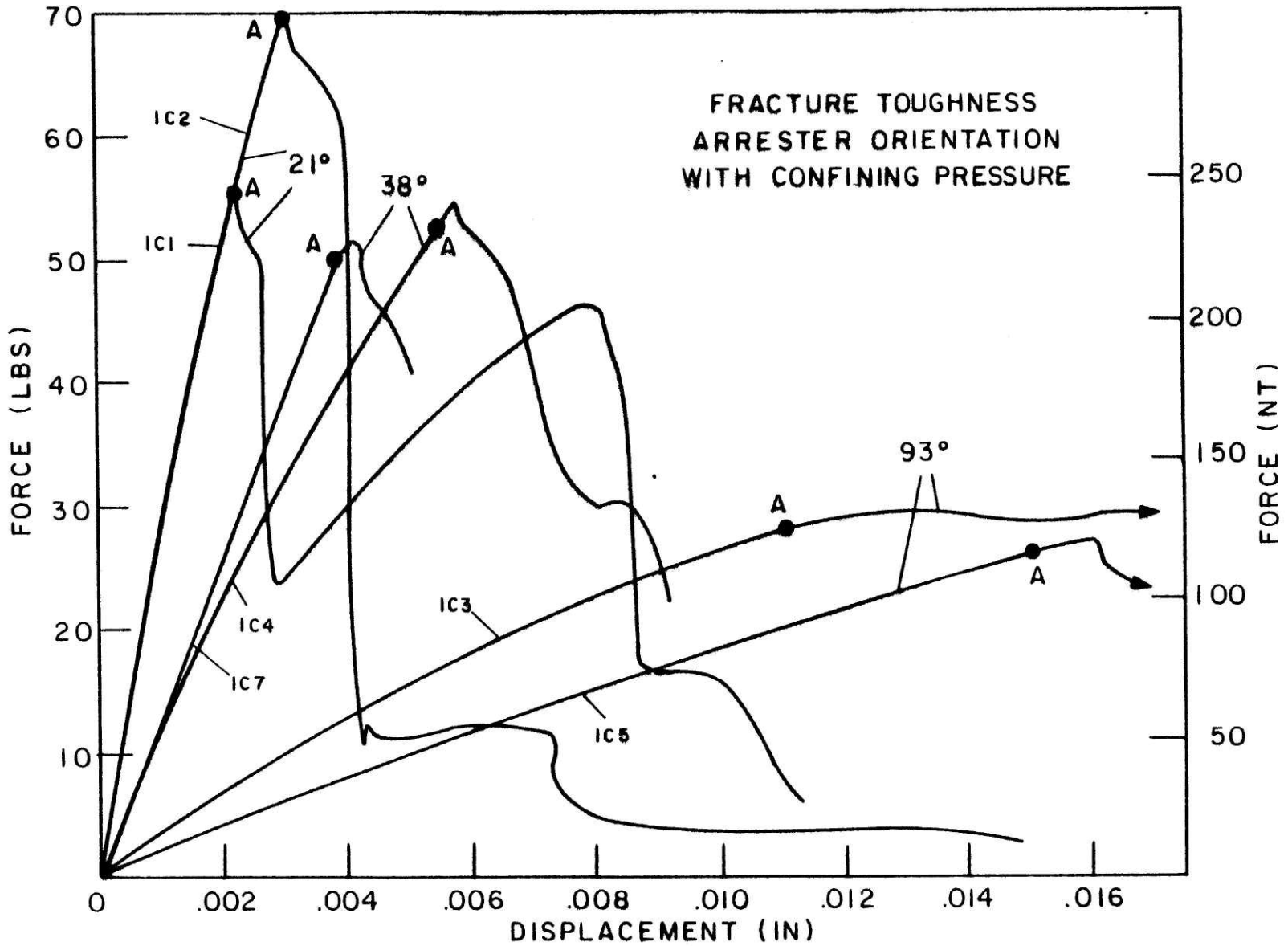

Figure 25: Load vs. load-point displacement plot for compact tension specimens in the arrester orientation with confinement. Pt. A refers to point of 2% deviation from power law for nominal 30 gpt shale at various temperatures.

of inter-bed strength. Without confinement, the loading channelled the stress into the narrow region between the nearest weak plane and the crack tip: the tensile stresses which would be induced across the vertical weak planes cannot be carried beyond the limited tensile strength, which was shown earlier to drastically decrease over the above temperature range, due to initial organic breakdown. With confinement, this failure mechanism was eliminated; indeed, arrester toughness increased two-fold from 21°C to 93°C. However, the absolute values below 38°C were much lower, relative to tests without confining pressure. This suggests that subcritical crack growth in the process zone around the crack tip (e.g. Hoagland, et. al, 1973) was minimized in the confined tests, and that most of the energy put into the rock was consumed in the propagation of the major fracture through the ligament area.

Other calculations showed that maximum loads decreased approximately three-fold from 21°C to 93°C, for all geometries (including confined arrester) and that toughness values calculated at maximum load indicated increase by factures of four, three and 1.5 for the divider, arrester and short transverse geometries, respectively. The increases were a result of dramatic increases in the shale's compliance and strains to crack initiation around the crack tip. Specific results are listed in Table VII.

TABLE VII

HIGH TEMPERATURE FRACTURE TOUGHNESS DATA

# Tests	Orientation	Temp. °C (°F)	Maximum Load kN (lbs)	Max. Load per Ligament area MN/m^2	J. (Joules/m^2) 2% dev.	J. (Joules/m^2) Max. Load
2	Divider	21 (70)	.556 (125)	.431	52.1	55.6
2	Divider	38 (100)	.374 (84)	.272	49.2	64.2
2	Divider	93 (200)	.200 (45)	.157	82.4	107.3
2	Divider	149 (300)	.102 (23)	.075	-	≈150
2	Short	21 (70)	.214 (48)	.189	16.0	16.0
2	Transverse	93 (200)	.062 (14)	.052	14.2	24.5
2	Arrester	21 (70)	.485 (109)	.354	53.5	54.1
2	Arrester	38 (100)	.347 (78)	.252	54.0	55.4
2	Arrester	93 (200)	.102 (23)	.079	31.0	32.5
[with confining stress]						
2	Arrester	21 (70)	.285 (64)	.224	19.0	19.0
2	Arrester	38 (100)	.249 (56)	.181	26.5	28.9
2	Arrester	93 (200)	.120 (27)	.093	38.6	49.2

The scatter among samples was minimal, particularly at higher temperatures, suggesting (as in uniaxial tests) a decreasing dependence of shale response on material inhomogeneities, as temperature is increased. Scatter was most pronounced for tests in the arrester geometry, as might be expected from the complex interaction between the crack tip and bedding laminae. Similar reasoning might have pertained to the short transverse geometry; however, little scatter was observed in these tests -- probably due to the low loads needed to initiate crack growth. Unstable fracturing to failure was detected for most specimens very soon after initiation for temperatures less than 38°C (100°F). However, the confined arrester samples exhibited additional toughness (Figure 25) after fracture initiation due to crack arrest at a particularly strong bedding plane. In order to overcome the high tensile strength of the shale in the plane parallel to the crack front at these points, for further propagation, an added force had to be applied to that particular region.

Some thermal cracking between the bedding planes was detected in tests of all geometries at temperatures of 93° or above. Determination of the combined effect of temperature and overall confinement (due to pre-existing stress state or induced underground pressurization during bed fracturing) on material toughness and the growth of

thermal cracks (during retorting) is particularly important. Relevant experiments are planned in future work.

Evidence on the effects of crack length (e.g. Schmidt, 1977) and confining pressure (e.g. Abou-Sayed, 1977) on fracture toughness is well documented; however, they illustrate an important and potentially crucial difficulty in the determination of the toughness parameter J for the compact tension geometry employed in the previous tests. The problem arises from the limitations on the specimen dimensions. While one restriction on the appropriate application of the J-integral method and Eqn. 1 is the limit of $a/w \to 1$ (thereby necessitating a crack length comparable to specimen length), a contradictory restriction exists in satisfying the dominance of the relevant crack tip singularity or characteristic stress field (e.g., Hutchinson, Rice and Rosengren, 1968). The stress-strain environment within some "process zone" should be dominated solely by conditions local to the crack tip leading edge, being insensitive to specimen geometry (crack size, net ligament, thickness, etc.), and other sundry factors (e.g., Begley and Landes, 1971). When combinations of these factors destroy this dominance, the applicability of J is limited. Equation (1) is useful as a toughness measurement, but it should be noted that the character of the fracture process may be influenced by geometry and confining stress. Our

particular problem is related, for instance, to a stress-free curved surface ahead of the crack tip (roughly a distance b/2 away), resulting from bending of the remaining ligament. This condition (discussed more thoroughly by Cleary, 1978b) may violate the above crack tip singularity state, depending on the size of the aforementioned process zone, and consequently limits the minimum allowable ligament length. A more careful characterization (e.g., by finite element analysis) is presently being conducted (Miller, 1978) to eliminate this problem and likewise to account for any anisotropic and nonlinear effects.

3. Cycling of Crack Loading: The Effect of Crack Radius. Unloading tests were performed to determine the effects of the finite notch-tip radius, which is expected to influence the conditions for crack initiation. Representative specimens in the three relevant geometries were loaded until fracture initiation was guaranteed (at a point arbitrarily chosen just after maximum load was attained); load was then cycled several times before total failure. The plots are shown in Figs. 26-28 for the arrester, divider, and short transverse geometries, respectively.

The importance of determining the energy release rates for both finite notch tip radii (e.g., in machine excavation) and shart natural cracks (e.g., in hydrofracturing)

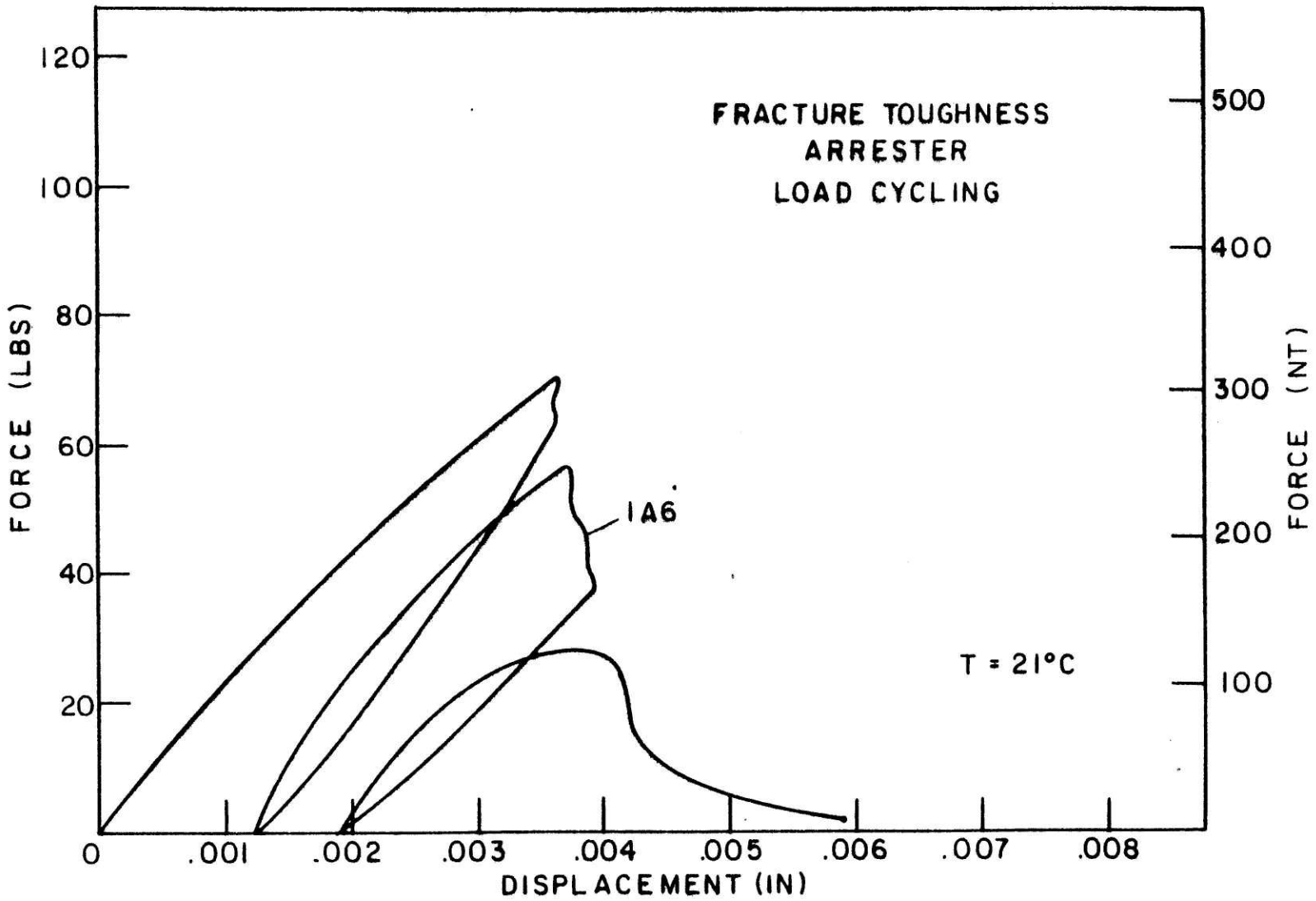

Figure 26: Load vs. load-point displacement plot for compact tension specimen in the arrester orientation with cycling. Test at 21°C for nominal 30 gpt shale.

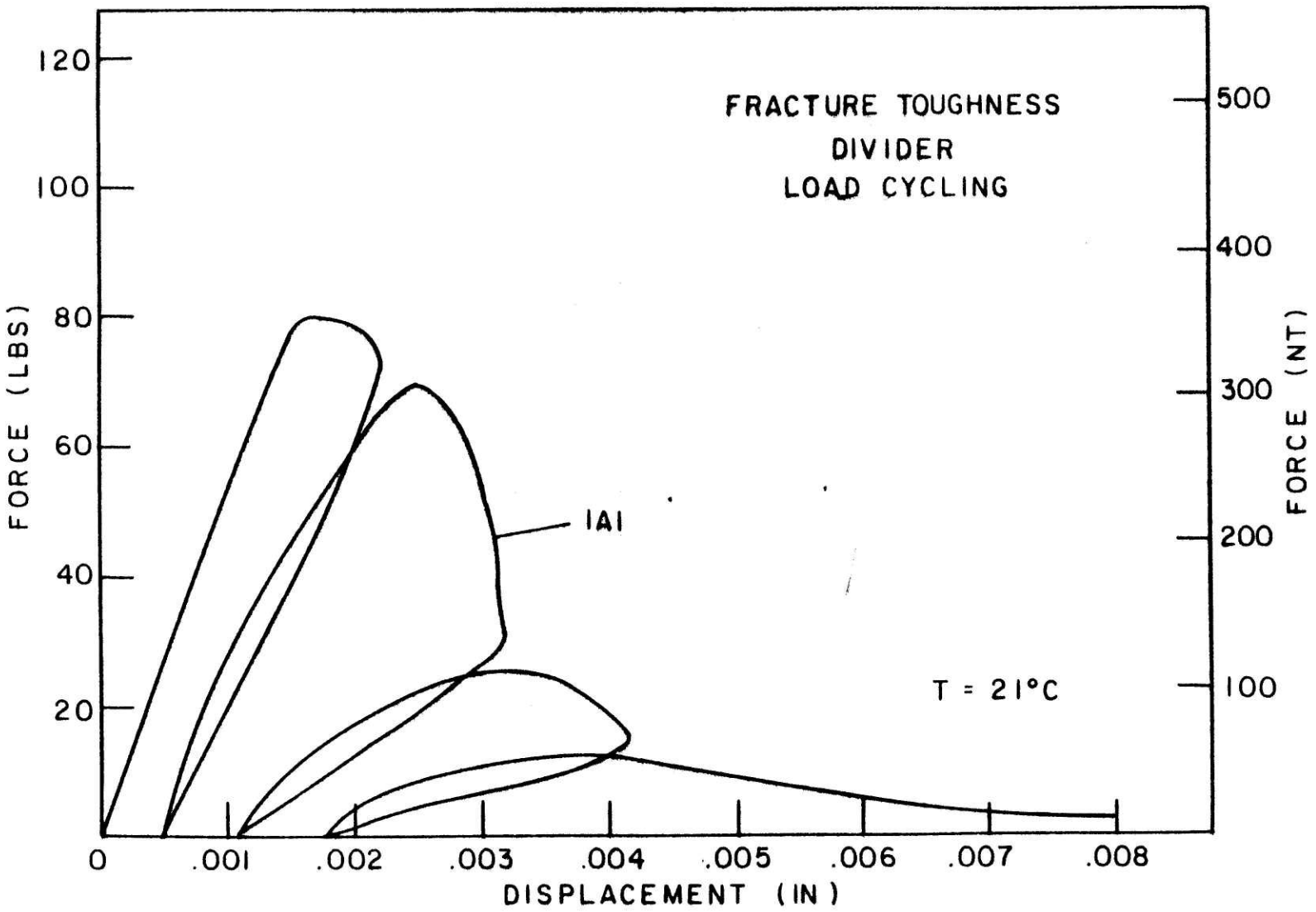

Figure 27: Load vs. load-point displacement plot for compact tension specimen in the divider orientation with cycling. Test at 21°C for nominal 30 gpt shale.

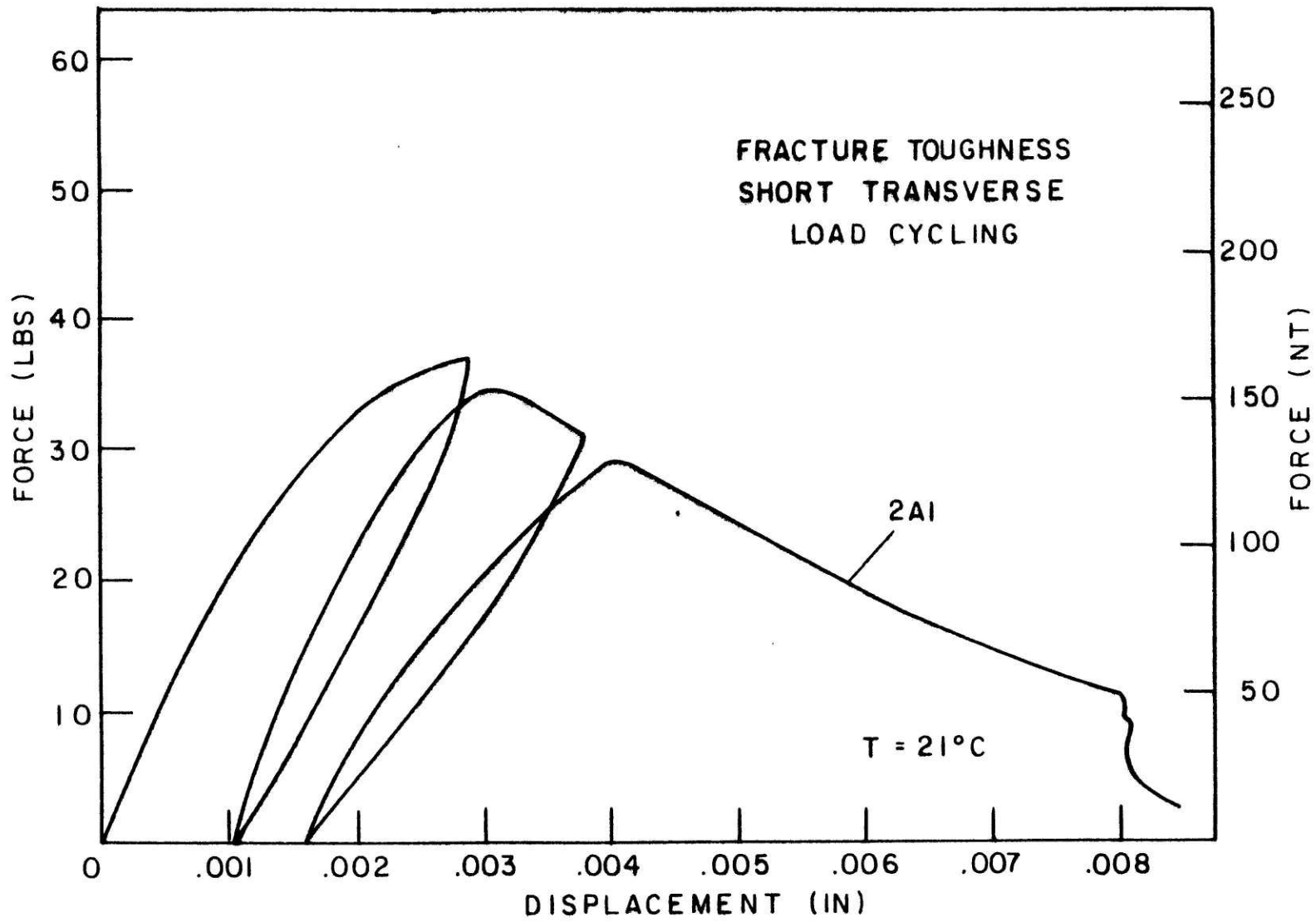

Figure 28: Load vs. load-point displacement plot for compact tension specimen in the short transverse orientation with cycling. Test at 21° for nominal 30 gpt shale.

is apparent. The finite radius is known to concentrate stress less than a sharp crack, so that increased values of the J-integral for initiation are expected. Although the ligament length was smaller following crack initiation from the finite notch tip, thereby changing the calculation for the J-integral, analysis of the plots shows that a moderate loss of toughness was generated for all geometries, as a result of having a sharp natural crack. J-toughness values derived at maximum load for finite notch tip/sharp natural crack were: divider-52.4/30.2; arrester-48.6/29.3; and short transverse-28.4/15.2. A comparison of the J-toughness values at maximum load from notched tips with those for reinitiation from natural fractures reveals about a 40% loss in toughness for all specimen geometries. These tests indicate a definite loss of material toughness for crack initiation in oil shale, when that initiation is from a natural fracture in the rock. Further tests are certainly warranted to account for thermal and confining stress effects.

4. Comparison with Other Techniques and Data. A number of fracture toughness experiments have been conducted on oil shale, in particular by Schmidt (1975, 1977). However, no high temperature fracture toughness results

were found in the literature and it is believed that little, if any, high temperature testing has been done previously.

Schmidt employed three-point-band specimens and an ASTM standardized testing procedure (for metals), i.e., insertion of a sharp fatigue crack. The toughness values reported by Schmidt (1977) were in the form of K_I, derived from linear elastic fracture mechanics, which quantifies the energy required for crack initiation and propagation through a material, for the case where the crack tip is in a state of plane strain. The critical value (K_I value at onset of crack-growth) has been shown (e.g., Schmidt, 1975) to be a material constant for a vast number of metal alloys, ceramics, polymers, and even some organic materials (e.g., wood, rubber); of course the specimens used for measurement must satisfy the appropriate geometric criteria. Its application to characterize oil shale, however, may be limited unless anisotropic and nonlinear effects are included in the calculations. The relationship between the J-integral (e.g., Rice, 1968) and the stress intensity factor K, for small-scale yielding is rather straight-forward, namely, (Cleary, 1978b):

$$J \simeq \alpha_1 K_1^2 + \alpha_2 K_2^2 + \alpha_3 K_3^2 \qquad (3)$$

where K_1, K_2, K_3 represent modes of opening, in-plane shearing, and out-of-plane shearing, respectively. The constants α_K have a form associated with the characteristic equation between moduli; in the isotropic case, for instance, $\alpha_1 = (1-\nu^2)/E$. Therefore, the familiar form for the isotropic version of equation (3) under a pure opening mode is:

$$J \simeq \frac{(1-\nu^2)}{E} K_1^2 \quad . \tag{4}$$

This equation was used for a comparison of data from the paper of Schmidt (1977) to the 21°C data in Table VII for toughnesses calculated both from a finite notch tip (Figures 22-24) and a sharp natural crack (Figure 25). The results are illustrated in Table VIII.

As shown, the Schmidt data reveals toughness values larger than those reported herein for all three crack orientations. A comparison between his data and that measured from the cycling tests of this report - both of which measured shale toughnesses from a sharp crack - shows a discrepancy of about 100% using an average value between his 20 and 40 gpt data. This discrepancy points out the need for a toughness measurement in oil shale which accounts for anisotropic and nonlinear effects. Schmidt's use of a fatigue crack and the LEFM stress

TABLE VIII

COMPARISON OF SHALE TOUGHNESS DATA AT 21°C

Orientation	J@2% dev. from Power Law ($\frac{Joules}{m^2}$) 30 gpt	J@ Max. Load ($\frac{Joules}{m^2}$) 30 gpt	J@ Max. Load Cycling Data ($\frac{Joules}{m^2}$) 30 gpt	Schmidt Data: $J = (\frac{Joules}{m^2})$ 20 gpt	40 gpt
Divider	52.1	55.6	30.2	50	100
Arrester	53.5	54.1	29.3	40	80
Short Transverse	16.0	24.5	15.2	(25)	20

intensity factor may have grossly overstated the shale's actual toughness.

In fairness, it should also be pointed out that the J-integral method is based on a model with elastic deformation, or monotonic stress paths; thus, unloading, as in the cases of Schmidt (1977) and the previous cycling tests, may invalidate its use. The J-integral essentially represents the rate of decrease of potential energy with respect to notch length (e.g., Rice, 1968) and it must inevitably vary with changing crack length. Additionally, some local unloading behind the tip of the crack may occur during crack advances (e.g. Amazigo and Hutchinson, 1976). However, an argument for more realism toward practical applications in the field (i.e. hydraulic fracturing underground) can be made with our methodology, even though significantly more analysis must be applied to Schmidt's procedure.

A critical distinction is also emphasized in experiments between those criteria for crack growth initiation (e.g., Schmidt, 1977; Figure 1) as against those for establishment of steady propagation (e.g., Clifton, et. al, 1976). The cracked annular specimens used by Clifton, et. al. (1976) allow substantial crack growth before onset of instability, while the specimens used herein and by Schmidt (particularly the divider and

arrester geometries) lead to instability almost immediately after crack initiation. Local crack-tip conditions underground, during actual field experiments, point to a more practical use of the cracked annular-type specimens for good laboratory simulation.

Since hydraulic fracturing from a borehole will generally be one means of bed preparation and/or containment for an in situ process, these annular tests could be used approximately to more closely simulate confinement around that borehole. The differentiation between initiation and steady propagation, which has been quantified in metallic alloys (e.g., Amazigo and Hutchinson, 1976), certainly warrants further analyses in rock materials. Considerable work is still required to increase our limited expertise with near-tip stress states and their effect on crack growth.

Other advantages of using cracked annular specimens for a good representation of the toughness of oil shale include: 1) the stress intensity at fracture need not be determined by the size of the crack at initial crack extension (as is necessary in compact tension specimens, 2) the value of the stress intensity factor is obtainable from accurate measurements of pressure and crack length at fracture, and 3) the annular-type specimens lend themselves to more sophisticated analyses. These

cracked annular specimens will be used much more in future work, in particular for experiments at various confining pressures and temperatures.

The use of eqn.(4) and isotropic K_I, even in the presence of severe anisotropy (i.e., Table V), is questionable in light of the plane anisotropic elastic fracture solutions at our disposal for bounded geometries (e.g. Bowie and Freese, 1972; Gandhi , 1972). It is possible (e.g.Table V) that a typical ratio of about 3 in principal axes modulimay exist in the oil shale at 21°C. Not surprisingly, Gandhi (1972) has shown,by an analysis of an inclined crack centrally.placed in an orthotropic rectangular plate, an effective difference of upwards from 25% between isotropic and anisotropic toughness data, depending on the orientation of the pre-existing crack relative to principal axes moduli. His mode I and mode II stress intensity values were calculated using a material with a ratio of about 2 in principal moduli. Even greater ratios (to 4 or 5) in principal moduli may be expected for oil shale in the field. Relevant comparisons, therefore, of experimental results to accuracies approaching 10% are absurd, due to the preceding argument. Additional analysis is necessary before a more accurate assessment can be made for toughness measurement in oil shale using laboratory-size specimens. The entire

discussion, however, points to the need for more detailed plane anisotropic elastic fracture solutions (Miller, 1979).

E. Comparative Uniaxial and Toughness Tests on a Kirkwood Sandstone.

Any oil shale extraction method, whether ex-situ (requiring conventional mining) or in-situ (incorporating fracturing and retorting in place) will necessitate an understanding of the surrounding strata and its response to various stress and thermal conditions. The effects are particularly important for any proposed in-situ process because of the need for adequate containment, both uring bed preparation and retorting, and for attaining good recovery efficiency. This knowledge of interface effects and material response must be evaluated (e.g., Cleary, 1978d) for the myriad of rock types which may border on the shale zones. The work presented here examines one particular rock, namely, a sandstone, for deformability and toughness characteristics. Other reports can be consulted for examinations of granite (e.g., Wilkening 1976), limestone (e.g., Abou-Sayed, 1977) and other sandstone and shales (e.g., Clifton, et al., 1976).

1. Uniaxial Tests. Unconfined tension and compression tests were performed on a Kirkwood sandstone to observe initial tangent moduli, Poisson ratios, and failure strengths and strains. The specimens were prepared and tested in a manner analogous to that for the shale samples (see Appendix I), using the same equipment throughout. All tests were performed at ambient temperature, e.g., corresponding to bed preparation conditions. Higher temperature tests did not seem warranted since it was felt (e.g., Lama and Vutukuri, 1978) that thermal effects would have little influence on the sandstone response (unlike the organic-bearing shale); however, further confined triaxial experiments are necessary for adequate underground simulation and should be done in future work.

The data for unconfined tension and compression tests, showing longitudinal and transverse strains, are presented in Figures 29 and 30, respectively. Specific results for moduli, Poisson ratios, and strengths are illustrated in Table IX.

Average values were calculated to be as follows: tangent moduli ≈ 11.6 GPa (1.7×10^6 psi), Poisson ratio ≈ 0.13, failure strengths ≈ 2.23 MPa (320 psi) in tension and 51.2 MPa (7400 psi) in compression, and failure strains ≈ .53 $m\varepsilon$ tension and ≈ 3.4 $m\varepsilon$ compression. A

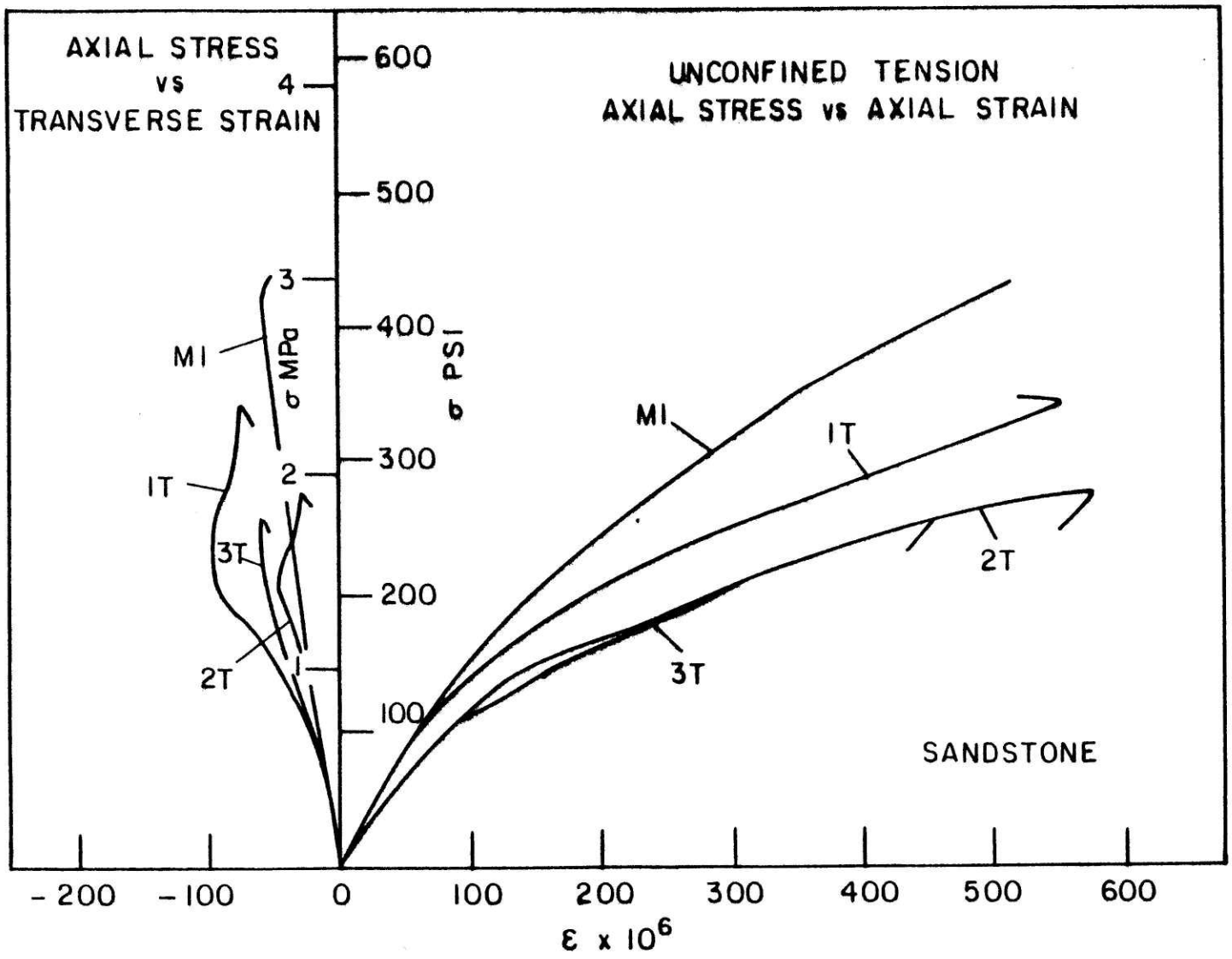

Figure 29: Axial stress vs. axial and transverse strains for uniaxial tension for a Kirkwood sandstone.

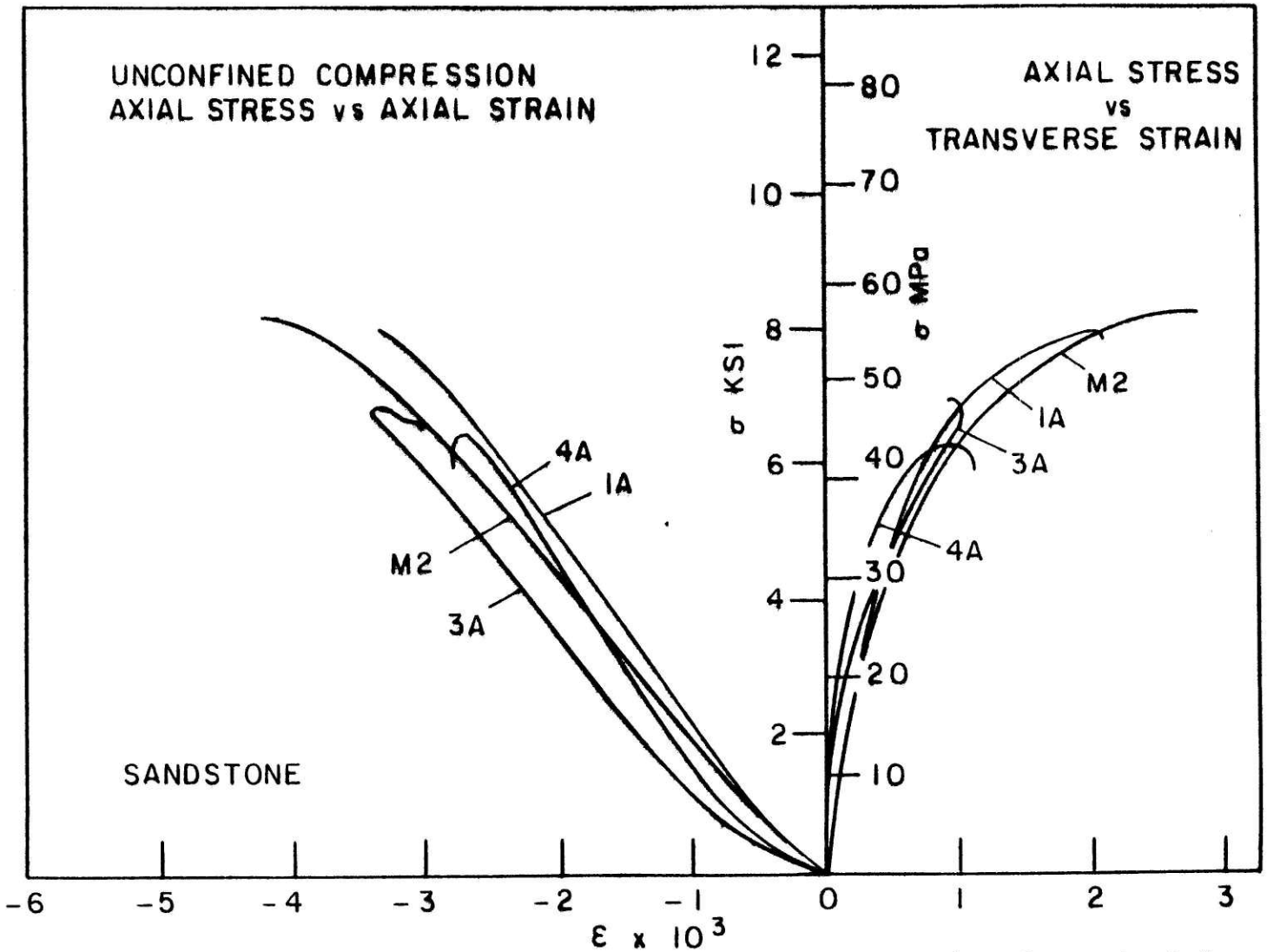

Figure 30: Axial stress vs. axial and transverse strains for uniaxial compression for a Kirkwood sandstone. Compressive stress taken as positive.

TABLE IX

UNIAXIAL RESULTS FOR A KIRKWOOD SANDSTONE

Specimen	Test	Eo GPa (psi)	ν_o	Failure Strength MPa (psi)	Strain mε
IT	Tension	13.2 (1.9×10^6)	.17	2.34 (340)	.56
2T	Tension	10.6 (1.5×10^6)	.07	1.90 (275)	.58
3T	Tension	9.1 (1.3×10^6)	.09	1.72 (250)	.46
MI	Tension	13.2 (1.9×10^6)	.12	2.96 (430)	.53
1A	Compression	19.4 (2.8×10^6)	.14	55.2 (8000)	-3.3
3A	Compression	7.2 (1.0×10^6)	.14	47.6 (6900)	-3.4
4A	Compression	8.3 (1.2×10^6)	.12	44.8 (6500)	-2.8
M2	Compression	12.4 (1.8×10^6)	.13	56.5 (8200)	-4.2

comparison to the shale data presented in Tables IV and V reveals a strong similarity in tangent moduli and failure strengths to ambient tests on cores normal to the bedding planes. The sandstone samples, however, exhibited much lower ductility and less resiliency on loading, as evident from the smaller initial lateral strains (i.e., Poisson ratios) and from the overall axial strains to failure. The sandstone also displayed the initial non-linear response to compressive loading which is characteristic of other rocks and rock-like materials (e.g., Jaegar and Cook, 1975), and often ascribed to crack closure.

2. Compact-Tension Fracture Toughness Results. Fracture toughness tests, employing specimens in the compact-tension geometry (see Figure 1), were also performed on the Kirkwood sandstone. The samples -- nominal 40 cm x 10 cm x 2.5 cm--were smaller than the corresponding shale samples due to the dimensions of the original disc-sahped blocks. The uncracked ligament length, b , was therefore shortened to 3.8 cm (1.5 in) to get a/w=.60. Procedures used were similar to those in Appendix V, without the compressive gig.

The curves of load versus load-point displacements are plotted in Figure 31, and calculations of maximum load per ligament area and J-toughness (as determined by Eqn. 1) are illustrated in Table X. An average J-toughness value of 37 Joules/m^2, at an average maximum load of 260 N (58 lbs) were derived. In comparison to oil shale data (Table VII) at ambient temperature, this toughness measurement falls roughly midway between the divider and short transverse toughness values. Although one-half the value of the unconfined shale tests in the arrester geometry, the sandstone was approximately twice as tough as the confined arrester tests at 21°C. These sandstone characterization tests also revealed a slow propagation to failure following crack initiation from the finite notch tip (oddly analogous to the higher temperature shale tests).

A more quantitative, or even qualitative, implementation of the shale and sandstone deformation and toughness data cannot be justified until further tests are done. These tests should more accurately simulate the desired underground conditions at potential shale-sandstone interfaces, and the effects of crack propagation in their vicinity (e.g., Cleary, 1978d).

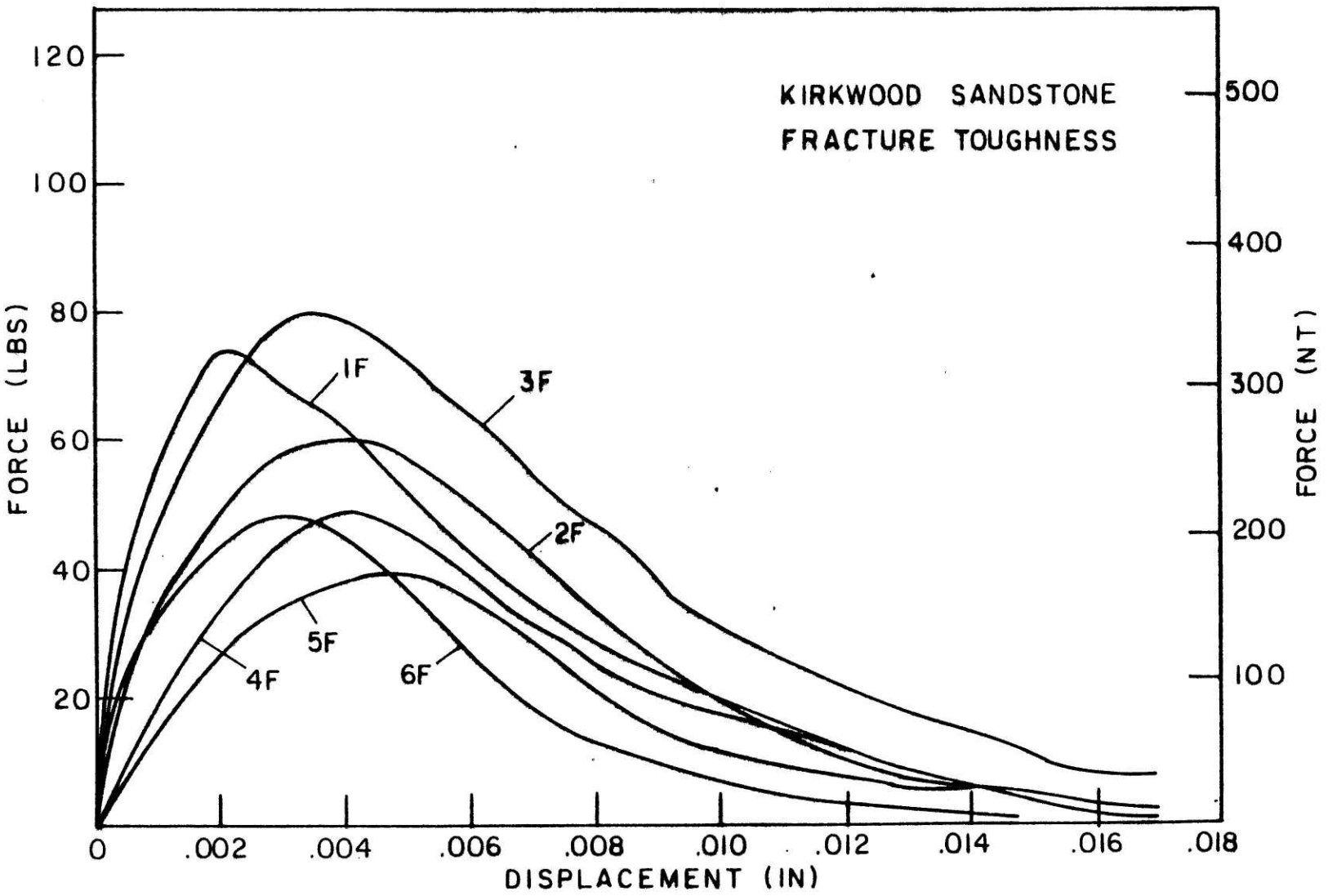

Figure 31: Load vs. load-point displacement plot for compact tension specimens for a Kirkwood sandstone.

TABLE X

KIRKWOOD SANDSTONE FRACTURE TOUGHNESS DATA

Specimen	F_{max} N. (lbs)	Max. load per Ligament Area MN/m^2	J@ F_{max} J/m^2
1F	328 (74)	.450	37.9
2F	256 (60)	.266	40.5
3F	355 (80)	.365	46.6
4F	217 (49)	.210	27.4
5F	173 (39)	.232	39.4
6F	208 (47)	.312	38.2

IV CONCLUSIONS

A. Observed Behavior

Significant nonlinear straining was detected in both uniaxial and triaxial tests on oil shale, with high hysteresis on unloading. This hysteresis response and consequent energy loss on unloading increased directly with increasing temperature. An increase in temperature from ambient to 200°C reduced the Young's modulus by roughly two orders of magnitude and strength by a factor of order five; additionally, strains to failure were increased about five-fold over this temperature range. The need to reach the failure strength of the shale is emphasized, particularly with the extreme hysteresis and large strains exhibited by oil shale at the higher temperatures, in order to point out the large amounts of energy and machinery which might be needed to produce suitable fractured retort zones.

Tensile strength normal to the bedding planes in the shale was observed to decrease twice as rapidly, with increasing temperature, as that parallel to the beds. This observation revealed the intensifying role (with increasing temperature) of the organic matter in overall shale response. Failures, and any thermal-induced cracking, generally occurred between the bedding planes with

increasing irregularity as temperatures rose. Thermal cracking was detected at temperatures above 100°C, but substantial cracking was not seen in any of the tests to over 200°C.

Stressing at an angle of $\pi/4$ to the bedding planes produced consistent failures along the beds; however, increased strength in the moderate temperature range (~50°C - 200°C) was observed, suggesting dominance of a frictional component due to restraint of sliding. This constraint would be eliminated once sufficient kerogen was pyrolyzed between the beds. Sliding along the beds would actually promote increased crack link-up and earlier failure in the shale; this deduction was supported by data at higher temperatures.

Stress cycling and relief produced marked hysteresis in the oil shale and revealed significant stress-induced anisotropic properties. These tests again pointed to the necessity of attaining the full failure stress in the shale if sufficient fracturing is to be achieved.

Triaxial confinement to 70 MPa ($\sim$ 10,000 psi) increased the shale modulus more than two-fold, strength to failure three-fold, and total strains about ten-fold. Although the interdependence of both confinement and temperature on shale response was not examined in this research (and indeed it seems to be very complex due to

the nature of oil shale), their combined effect (at σ_c = 70 MPa and T = 200°C) might be such that, although strength should decrease by a factor of two, strain to failure could potentially increase by fifty-fold. The overall energy of failure could, therefore, increase by about twenty-five-fold.

This suggestion also agrees with the fracture toughness experiments performed herein. Toughness values in the arrester geometry increased by more than a factor of three over a temperature rise of just 60°C, with added confinement of only 1.5 MPa (200 psi). Fracture toughness values varied noticeably with crack orientation and temperature, with the divider and short transverse geometries exhibiting the highest and lowest toughnesses at maximum load, respectively. The unconfined arrester and divider tests were comparable up to 38°C when measured at the onset of crack growth. Although the divider and short transverse geometries were not tested under confinement, their toughnesses generally increased two-fold in going to 100°C. Additionally, toughness values decreased about 40% when crack growth was initiated from a sharp natural crack, rather than from a finite notch tip.

Coefficients of thermal expansion equaling roughly 1.1×10^{-5}/°C (6.1×10^{-6}/°F) and 2.8×10^{-5}/°C (1.5×10^{-5}/°F), parallel and perpendicular to bedding, respectively, were calculated for the nominal 30 gpt shale in going from 21°C to 204°C. Average volumetric expansion in the cores was about 0.5% at 93°C, increasing to about 1.0% at 204°C. Although thermal diffusivity or thermal conductivity was not measured directly in the characterization tests, an approximate value was derived for diffusivity from the above expansion tests. Diffusivity is related to conductivity by the following relation (Shewman, 1963):

$$D = k/(\rho \times C_p) \qquad (5)$$

where $D(cm^2/sec)$ is the diffusivity, $k(Joules/cm \cdot sec \cdot °F)$ the conductivity, C_p (Joules/g·°F) the heat capacity, and $\rho(g/cm^3)$ the density of the material. An approximate diffusivity value of $4 \times 10^{-3} cm^2/sec$ was calculated from an observed expansion stabilization after 30 minutes in a 3.7 cm diameter core. Kerogen excretions were detected at 200°C in tests normal to bedding, and seemed to be purely thermally-induced. The liquid had a consistency comparable to a thick oil.

B. Relevance to In Situ Extraction.

A start has been made towards a rigorous thermo-mechanical characterization of deformation and fracture in oil shale. Data has been given for initially quantifying the role of temperature in shale response; in particular, for an assessment of strength, moduli, and stress-induced anisotropic variations (cycling). A notable phase transition in the kerogen was detected, between 40°C and 90°C, resulting in marked changes in shale response. Further tests at temperatures greater than 204°C (approaching 450°C) are required to more effectively evaluate the porous media regime of the shale, and the corresponding fracture stabilization mechanisms.

The results from early field tests (e.g., Thomas, et al., 1972), employing hydraulic fracturing for zone access and preparations were not promising. However, we feel that primary access to the in situ retort zone can be better achieved from a network of controlled hydraulic fractures. It will be necessary for economic feasibility, though, that multiple controlled cracks from a single borehole be obtained; techniques to accomplish this need to be developed. Additionally, the above process will require assistance from a secondary thermal cracking mechanism for the successful attainment of adequate, homogeneous permeability in the process zone. This mechanism

is needed to provide sufficient diffusivity for the vaporizing kerogen.

The data herein indicated that thermal cracking could be induced in representative samples of oil shale at temperatures above roughly 100°C. However, this cracking occurred almost solely in the kerogen-rich layers between the beds, and further experiments at even greater temperatures with confinement are necessary. Initial high temperature fracture toughness tests revealed a general increase in shale toughness with increasing temperature, while also showing that thermal cracks are formed (again along the bedding) with 2 MPa confinement.

The production of large-scale controlled fractures in the shale strata underground has been a major goal of many researchers for years. Explosive attempts (e.g., Murri, et al., 1977; Schmidt, 1975) have tended to produce a distribution of particle sizes, with the consequent potential for clogging of passageways. More sophisticated procedures utilizing quasi-static techniques (e.g., hydraulic, chemical) are needed to eliminate such near-borehole pulverization.

Further research by our group will center on establishing the role of temperature, confinement, and strain

rate on material response: we are currently engaged on homogeneous, high temperature triaxial tests and on a variety of innovations for evaluating fracture response at various pressures and temperatures, in numerous geometries.

The addition of thermal effects in the constitutive relation (Appendix VII) is a first step toward increasing the level of sophistication in modelling procedures.

A heavy financial commitment has recently been made towards the development of our country's oil shale reserves. However, more sophisticated technology must be provided from all sections of society before a viable approach is found to the shale oil extraction problem. Improved access, preparation and retorting procedures may soon make possible a feasible solution to the in situ problem and, comsequently, provide some temporary relief in our present energy dilemma.

APPENDIX I

SPECIMEN PREPARATION

One especially large block of oil shale from Colorado, which was found to be essentially crack-free, provided the bulk of the material for the tests. The block was assayed by National Resources Laboratory, Inc. at an oil content of 26.5 - 34.4 gpt. A 6-inch radius water-cooled diamond saw was used to cut the block into smaller, more manageable slabs which were to be used in designated tests. Water cooled diamond cutters (saws and corers) were used almost exclusively because of their accuracy and general convenience in cutting the shale. Steel bandsaws and drill bits dulled very quickly in cutting the shale, and they proved less accurate and more time-consuming than the diamond-tipped tools.

Cores of various lengths, depending on the particular test, were cut with the bedding planes normal, parallel, and at $\theta = \pi/4$ to the axis of the drill. A 5-inch vertical travel drill press was used for obtaining the desired lengths. Cores of various diameters - nomial 3.8 cm and 2.7 cm for uniaxial tests, 1.9 cm for triaxial tests - were cut at 1100 rpm with the respective diamond coring drills (products of Magwen Diamond, Inc., Framingham,

Mass.). Water was fed in through the drill to both cool the tip and flush away the chips. Care was taken in handling the newly cut cores because of their fragility and affinity to grease and slime.

Tensile Specimens. Those cores designated for tension tests (2.7 cm o.d.) were faced off on the lathe with a blunt tungsten carbide bit to a nomial 10 cm length. Good parallelism of the ends was achieved because of the smooth walls of the cores. Final alignment along the center line of the core was obtained later.

2024 - T4 aluminum alloy end pieces nomially 1 inch long, cut from 1 inch bar stock, were epoxied to the ends of the cores for tensile capability. These aluminum pieces were faced off at both ends for good parallelism.

Although Hangen (1977) had considerable difficulty in achieving an adequate bond between the aluminum and the oil shale, a relatively quick approach was used herein. The following technique proved very successful, even at higher temperatures. After the ends of the tensile core were faced off, a 1/2 inch diameter (1/2 inch deep) hole was cored, again using a diamond-tipped coring drill, in both ends of the specimen. The aluminum end pieces were degreased with methylethylchloride, particularly the face to be contacted with the shale. A

general purpose epoxy adhesive, Eccobond 51*, with a maximum tensile strength of 5000psi up to 177°C (350°F), was then coated on the aluminum end pieces and the oil shale ends. The shale ends were usually heated somewhat so that the half-inch holes could be more easily filled with epoxy. Care was taken to eliminate all bubbles and foreign particles. The shale and aluminum ends were then placed in a gluing fixture with a small spring load to maintain contact pressure at the bond face while they were cured at 66°C for 1 hour.

After bonding was complete, the specimens were turned down on a lathe to a nominal 1 inch diameter with a dull carbide tool bit. Generally, .010 inch deep cuts were taken at a moderate feed to get within .005 inch of the final diameter. The final .005 inch cut was made at a very fine feed - the result was a smooth surface on the oil shale.

Finally, the aluminum end pieces were threaded (14 NF) carefully, using shallow cutting depths of less than .010 inch to minimize any prestressing of the cores.

---

*A product of Emerson and Cuming, Inc., Canton, Mass.

Uniaxial and triaxial compression specimens. The ends of these cores designated for uniaxial compression (3.8 cm dia.) and triaxial compression (1.9 cm dia.) tests were ground down to a nomial length-to-diameter ratio of two. Typically, .025 inch cuts were taken to get within .005 inch of the final length; the final pass under the grinding wheel to remove the .005 inch amount left a very shiny surface on the shale. Both ends were ground similarly, and subsequently were found to be parallel to within an angle of 2'. Again, water was used to flush the particles from the shale and also to minimize dust production.

Compact tension specimens. Compact tension specimens were sliced from the smaller blocks to a nominal 1 inch thickness with the 6-inch radius water-cooled diamond saw. The perimeter of the samples were then more finely cut with the diamond saw to the nominal 5"x5" specification. One-half inch diameter pin holes were drilled using a water-fed diamond corer. The use of the diamond saw and corer generally produced no cracking or breakouts in the shale specimens. After the load pin holes were cored, the notch was cut using a 10 cm o.d., 20 mm thick diamond cutoff wheel. A notch tip was left with an equivalent radius of curvature of .004 inch. Relevant dimensions

of the specimens were as illustrated in Figure I-1.

An inelastic zone around the crack tip is also shown. This is a region of extensive microdamage which proceeds the large fracture through the ligament area. Significant energy can be lost (Table VII) during crack propagation because of this cracking.

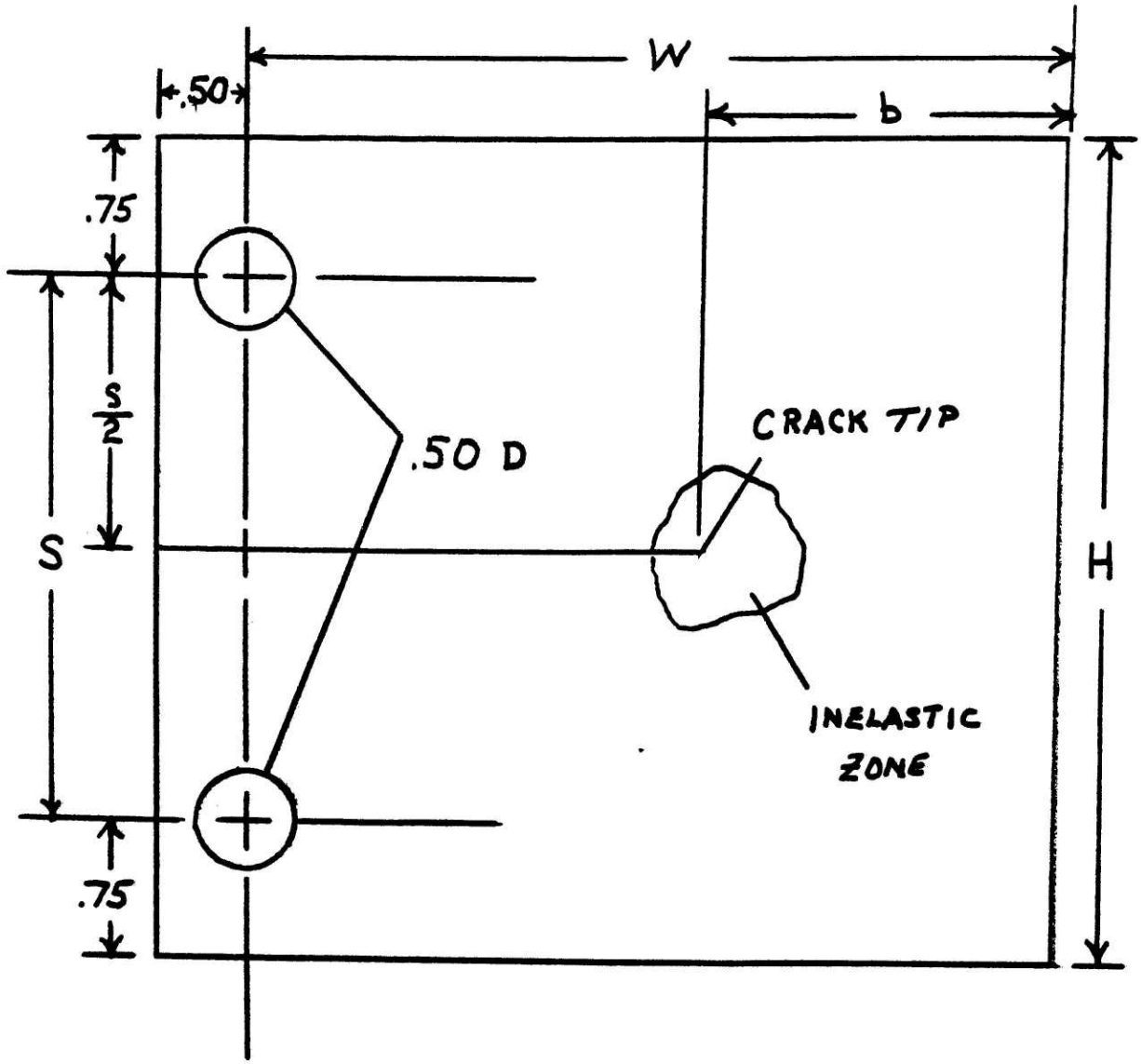

Figure I-1: Compact tension design for measurement of fracture toughness, J, in the shale and sandstone specimens.

APPENDIX II

HIGH TEMPERATURE UNIAXIAL TENSION TESTING PROECURE

All of the tension tests were conducted in an Instron environmental chamber* mounted on a screw-driven Instron Universal Testing Machine. The environmental chamber had a maximum temperature capability of 400° (204°C) with a sensitivity of ±2°F. Heat-up time required was about 10 minutes to 200°F, and about 30 minutes to 400°F. The internal dimensions of the chamber, which heated by convection, were 9 3/4"Wx9"Dx19"H. The load was applied through a universal joint and the specimen grips employed double ball joints with a lubricated brass ball to maintain loading axiality (See Hangen, 1977). Crosshead speed during the testing was .01 inches per minute but much of this deflection was taken up by the machine and grip compliances. The resultant stress/strain rate on the cores was about $\cdot\frac{01\text{Mpa}}{\text{min}} / \frac{10\ m\varepsilon}{\text{min}}$ at 21°C, while generally decreasing with increasing temperature.

*Model #3111, a product of Instron Corp., Canton, MA

Longitudinal and transverse strains were measured with strain gages attached near the center of the specimens, to eliminate end effects. These gages were applied just before the specimens were inserted in the temperature chamber and heated to the required temperature. They were used to 121°C (250°F), after which a bridge circuit extensometer was employed for strain measurement. Further details of strain gage usage at the higher temperatures are discussed in Appendix III.

Axiality of the threads and alignment of grips and the specimen ends was determined, in an initial test on an aluminum bar of similar length and diameter, to produce minimal eccentric loading of the specimens. Bending stresses were found to be less than 1.0% of the nominal axial stress, which, within the accuracy of experimental procedure (i.e., gage application on the core) and the scatter of oil shale data (as much as 50% in cores within the same block) were inconsequential to the final results. This eccentricity and resultant bending stress was determined by subtracting the signals of 2 strain gages separated by 180° on the specimens. However, the instrumentation (see Wilkening, 1976, for details) allowed differential measurement of all three strain components by averaging the signals of 2 strain gages separated by 180°

for cancellation of the remaining bending stress. Since this factor was not important for good readings, single gages for each strain component were employed for the majority of the testing. Figure II-1 shows a tensile test set-up in the environmental chamber prior to heating.

Figure II-1: Tensile specimen, grips and attached strain gages prior to heat-up and testing in the environmental chamber.

APPENDIX III

ELECTRONIC EQUIPMENT FOR LOAD AND STRAIN MEASUREMENTS AND HIGH TEMPERATURE CALIBRATION PROCEDURES

Axial and transverse strains were measured using 6.35 mm strain gages* with a 120.0 ± .2 Ω resistance and 2.05 ± 1% gage factor. They were used in conjunction with a Wheatstone bridge circuit and differential amplifier system designed and built by Wilkening (1976). Briefly, the bridge circuit can be used with either one or two active gages so that signals may be added, to cancel bending, or subtracted, to strictly show the bending component. Voltage was supplied by a 15-volt power source and regulated by four integrated-circuit voltage regulators. The regulators produced a nominal 7-volt reference voltage which was carried to the bridge circuits. The calibration of the voltage was set by adjustments on the recorder to 10 cm ± 1%. The calibration resistor (5730 Ω) produced a 1% strain signal in conjunction with the 2.05 gage factor.

At times,increased sensitivity was required for an accurate measurement of strain response. Three dif-

*Type FAE-25-12-S6L; a product of BLH Electronics, Waltham, Mass. Price: $3.00 each.

ferential amplifiers were utilized to increase the total gain available from the system to 1000. An accuracy of $5x10^{-6}$ was attainable before background noise predominated. Further details and schematics are not given, but may be found in Hangen (1977) and Wilkening (1976). The electronics and recorders were conveniently mounted on a cart, as pictured in Figure III-1.

The high temperature use of the strain gages and equipment required an additional calibration stage prior to testing. To test for thermal effects on the gages, adhesive, solders, and wires in the temperature chamber, an initial test was performed on a similar size piece of 1018 carbon steel. Strain gages were mounted on the steel using the Eastman 910* adhesive using a standard gage application procedure. The steel specimens were then heated to temperature in the chamber, and allowed to stabilize for one hour. The specimens were tested, both in tension and compression, to the stress levels obtained from the initial shale characterization experiments. Thermally induced strains of 120 με at 93°C and 175 με at 204°C were recorded for the sytem after subtracting

*Product of Eastman Chemical Products, Inc., Kingsport, Tenn.

Figure III-1: Cart with electronic equipment and X-Y recorders for data acquisition.

thermal expansion for the steel* itself. These strains were reached within five minutes after the desired temperature was attained in the Instron chamber. There was also no detectable increase with stress, again once stabilization had occurred.

Following these tests, another strain calibration procedure was done to check for thermal expansion in the oil shale specimens. Strain gages were applied similarly to representative tensile and compressive shale cores of nominal 30 gpt. The specimens were then carefully placed in the chamber and heated to various temperatures. Once the temperature was reached, the cores were allowed to stabilize for one hour, the normal stabilization time for all the tests. Overall stabilization typically occurred roughly 1/2 hour after the desired temperature was established in the chamber. After subtracting the thermally induced strains from the gages and epoxy, maximum longitudinal and transverse strains of 1 $m\varepsilon$ and 2 $m\varepsilon$ were observed after 1/2 hour at 93°C (200°F). At 204°C, these strains increased to roughly 1.4 $m\varepsilon$ and 2.5 $m\varepsilon$, respectively. This data indicated approximately .5% and 1.0% volumetric expansions of the oil shale at

---

*Coefficient of thermal expansion for 1018 cold drawn steel $\equiv 8.4 \times 10^{6}/°F$

93°C and 204°C, respectively, after 1/2 hour at temperature.

At temperatures greater than 121°C, strains were measured using an Instron extensometer* and the calibration system in the Instron machine. Specifications of the extensometer included a 1 inch gage length and a maximum strain of 10%,with a sensitivity of ± .25%. However, the sensitivity of the Instron system itself, at about ± .50%, was the limiting factor in the overall system. At temperatures greater than 121°C, though, the strain recorded on the shale were all generally in the 5-50 mε range.

For the compact tension fracture experiments, linear variable differential transformers (LVDT's) were used to record load-point displacement. An accuracy of 10^{-4} inches was measured by a micrometer over the linear range of the LVDT's. The load-point displacements were measured differentially by 2 LVDT's, one on each side of the specimen, to account for any Mode III motion resulting from pin hole misalignment. Additional details of these electronics are described by Wilkening (1976) and Hangen (1977).

*Model #2630 - 001.

APPENDIX IV

HIGH TEMPERATURE UNAXIAL COMPRESSION TESTING PROCEDURES

Compression tests of the nominal 30 gpt shale were conducted over a range of temperatures from 21°C to 204°C on the Instron environmental chamber. A compression cage, designed to accommodate specimens of nominal 1.50 inch diameter and 3.5 inch length in the chamber, was used for direct platen loading in the tests. The cage was constructed of a high-strength, high alloy steel * and designed to meet a maximum 80,000 lb. load specification. Strain gages were used, as described in Appendix III, to 121°C. The 204°C tests were performed using the Instron bridge circuit extensometer. Figure IV-1 illustrates a typical experimental set-up, with the compression cage for axial loading in the Instron chamber.

*Carpenter steel type 883; AISI Type H13

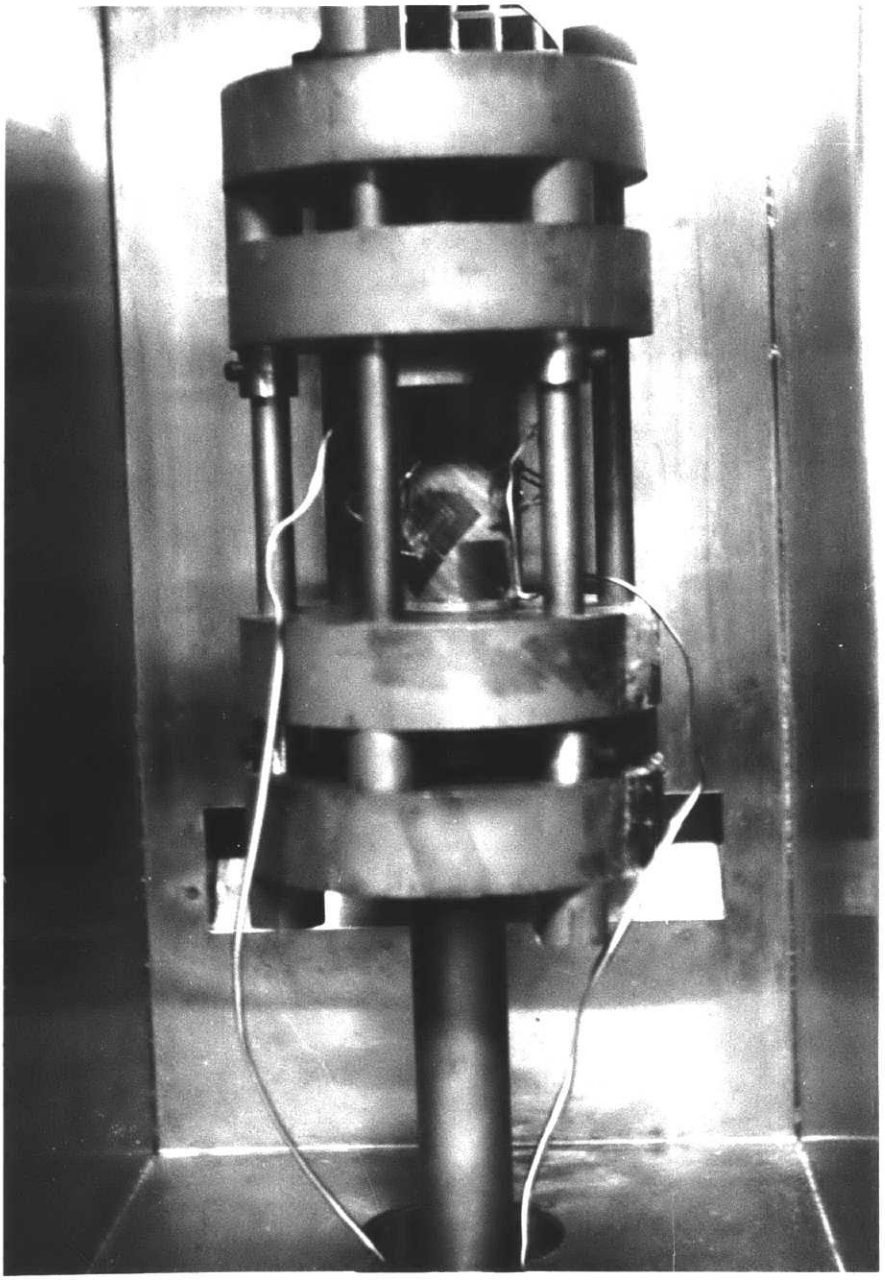

Figure IV-1: Compression specimen, gages and compression cage prior to heat-up and testing in the environmental chamber.

APPENDIX V

HIGH TEMPERATURE FRACTURE TOUGHNESS TESTING PROCEDURES

The fracture toughness of the nominal 30 gpt oil shale was measured to 93°C, for the three relevant geometries (Figure 1), by the J-integral method for deeply notched specimens loaded in bending. The integral of the J determination in equation (1) was evaluated graphically by measuring the area under the F-δ curve. Mode III shear loading, which was possible due to any misalignment of the loading pin holes, was eliminated by differentially measuring the load point displacements with an LVDT positioned on both sides of the specimen. The LVDT's were mounted on aluminum plates cemented to the top and bottom of the specimen with Eastman 910 adhesive. The centerlines of the LVDT's aligned in the plane of the loading pin centerlines, thus measuring the load point displacements directly. A compression gig was used to add $\sim$ 200 psi confinement normal to bedding in a few of the arrestor geometry tests. This apparatus was attached before the LVDT plates were secured to the specimens. A typical compact tension-testing arrangement-- in the arrester orientation with confinement -- is shown in Figure V-I.

The fracture toughness, J, was evaluated both graphically and by a quasi-analytic procedure. For each curve in Figures 22-25, J was computed at maximum load

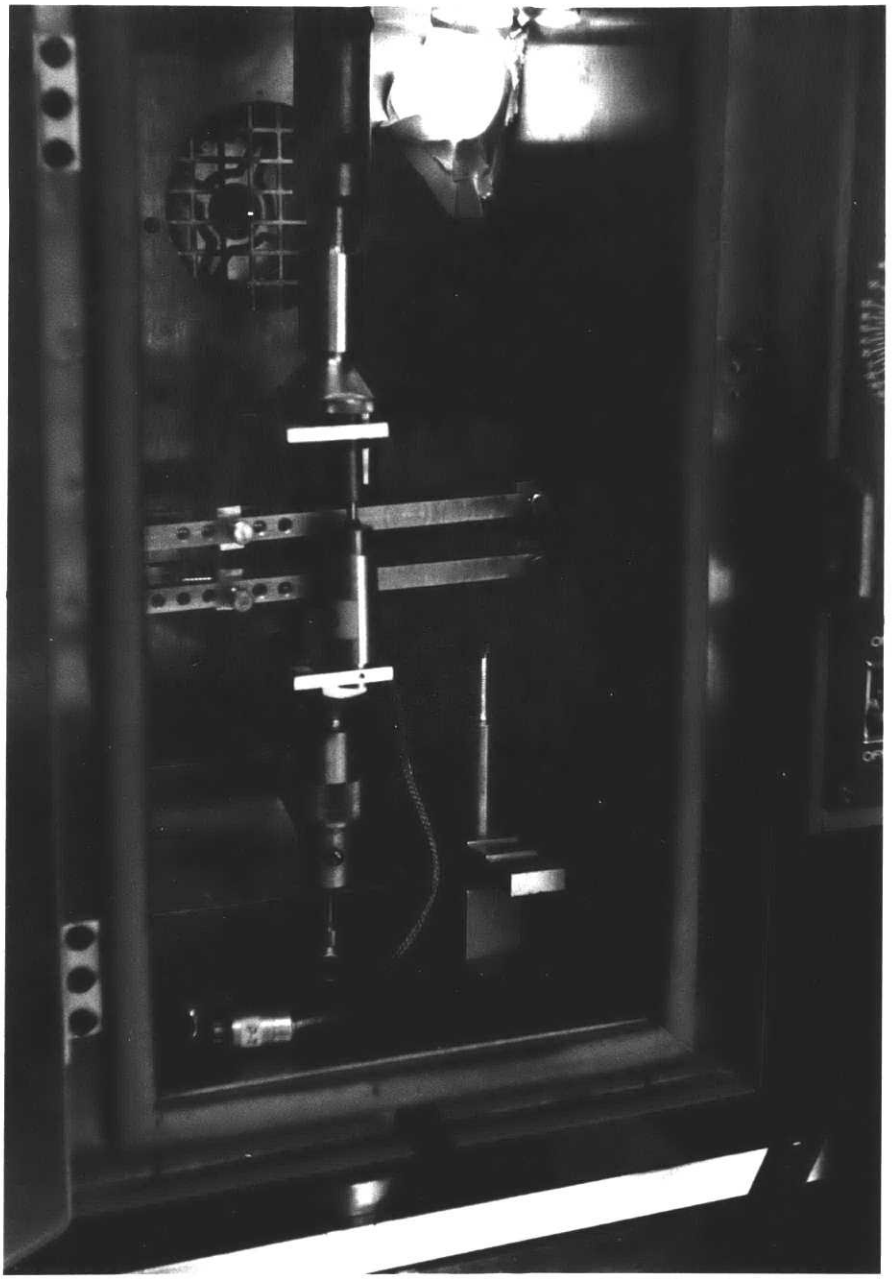

Figure V-1: Compact tension arrangement, with the compression gig, LVDT's and grips in the Instron chamber.

and at a displacement which was assumed to be the point of crack initiation. For those plots which did not have an obvious deviation from a smooth curve, which would clearly indicate crack initiation, the data was fitted to a power law of the form

$$\delta = C_0 F + K(C_0 F)^m \qquad (V\text{-}1)$$

over the initial portion of the curve. The critical displacement, δ_c used in Equation (1), was then arbitrarily chosen to be the point where actual displacement was 2% greater than that predicted by the power law. The initial compliance, C_o of the F-δ curve was measured directly from the plots. Representative (δ,F) points from the initial portion of the curve was used to plot $\ln(\delta - C_o F)$ vs. $\ln(C_o F)$. The slope of that curve gave m; plugging in the values into Eqn. (V-1) gave the value of K. Following these calculations, C_o was set equal to 1.02 C_o (2% greater) and new values of δ and F were derived using the above dimensionless K and m numbers in Eq. (V-1). The new values, δ' and F', were plotted alongside the original values -- and the intercept of the two curves gave the critical displacement, δ_c, for the determination of the toughness parameter, J.

Average values of C_o for all these orientations increased from 5.0×10^{-5} in/lb at 21°C to about 3.0×10^{-4} in/lb at 93°C. Typical values for m ranged between 2.0 and 3.6 and for K between 200 and 2000, without any noticeable dependences with either temperature or a particular specimen geometry. Graphically determining the 2% deviation from the power law invoked an uncertainty in $\Delta\delta$ of about 10%.

APPENDIX VI

TRIAXIAL TESTING PROCEDURES

Confined compression tests of the nominal 30 gpt shale were performed at room temperature in a very rigid, displacement-controlled triaxial machine. The interior dimensions of the test cell and the size of the bottom platen dictated the specimen size to be a nominal 1.9 cm diameter by 3.3 cm length. The triaxial machine had a loading capacity of 50 tons, a maximum ram travel of 3.0 cm, and a pressurization capability to 2 kilobars (30,000 psi). The cell was pressurized with a petroleum ether reagent* (boiling point ≡ 30°C).

To prevent the confining fluid from contacting the shale cores, the specimens were wrapped with an .125 in. thick, impermeable vinyl jacket** prior to insertion in the test cell. The system was pressurized slowly to the desired confinement stress before axial loading was applied by the top platen. Axial strain was recorded by an LVDT arrangement outside the cell. Calibration was provided for the LVDT by accompanying calibration curves. Both the LVDT and the load signals were fed into an

---

*Product of McKindolt, Inc., Norwood, Mass.

**Product of the Green Rubber Co., Cambridge, Mass.

X-Y recorder to obtain the desired plots. The screw driven upper platen was set at a speed of 4.2×10^{-4} in/min -- corresponding to stress and strain rates of 20 MPa/min and 2 $m\varepsilon$/min, respectively. The cell was drained thoroughly after each test, and each failed shale specimen was adroitly removed from its plastic membrane.

Further tests are under way in a 7-inch i.d. triaxial rockcell with a 69 MPa (10000 psi) confining pressure capability. An internal heating arrangement has been built so that tests to about $500^{o}F$ can be performed on cores of nominal 4-inch diameter and 6-inch length. The cell and associated pressurization system also have a separate internal borehole pressurization capability for experiments employing cores in the annular configuration. A computer data acquisition system is also being added to the overall setup for a more accurate and efficient means of gathering and assessing the data.

APPENDIX VII

GENERALIZED CONSTITUTIVE RELATION AND CURVE FITS*

In seeking constitutive equations for a transversely-isotropic material, we consider theoretical restrictions on the form as exemplified by Wineman and Pipkin (1964).

The stress tensor $\underset{\sim}{\sigma}$ is a function of the tensors defining the physical situation: $\underset{\sim}{\varepsilon}$, the strain tensor, and $\underset{\sim\sim}{nn}$ the material axis tensor ($\underset{\sim}{n}$ is unit vector perpendicular to the planes of isotropy -- Figure 4).

In lab coordinates:

$$\underset{\sim}{\varepsilon} = \begin{bmatrix} \varepsilon_{11} & \varepsilon_{12} & \varepsilon_{13} \\ \varepsilon_{21} & \varepsilon_{22} & \varepsilon_{23} \\ \varepsilon_{31} & \varepsilon_{32} & \varepsilon_{33} \end{bmatrix} \qquad \text{(VII-1)}$$

$$\underset{\sim}{n} = \underset{\sim}{e}_2 \sin\theta + \underset{\sim}{e}_3 \cos\theta \quad \text{(where } \underset{\sim}{e}_2, \underset{\sim}{e}_3 \text{ are basis vectors).} \qquad \text{(VII-2)}$$

Stress will have the form,

$$\underset{\sim}{\sigma} = \sum_k f_k \underset{\sim}{T}_k \qquad \text{(VII-3)}$$

where the $\underset{\sim}{T}_k$ are second order tensors with component polynomials in terms of $\underset{\sim\sim}{nn}$ and $\underset{\sim}{\varepsilon}$, and f_k are scalar

---

* This section was contributed by J. Papodopoulos.

functions of the invariants (numbers which define the physical situation, e.g., magnitudes and relative angles).

One method for finding the tensors $\underset{\sim}{T}_k$ (priv. comm. with Cleary, 1977-79) is to form all possible distinct second order tensorial products of $\underset{\sim}{\varepsilon}$, $\underset{\sim\sim}{nn}$, $\underset{\sim}{\delta}$ (identity tensor) and $\underset{\sim}{P}$ (alternating tensor), and require symmetry:

$$\underset{\sim}{\delta},\ \underset{\sim\sim}{nn},\ \underset{\sim}{\varepsilon},\ \underset{\sim}{\varepsilon}\cdot\underset{\sim\sim}{nn}+\underset{\sim\sim}{nn}\cdot\underset{\sim}{\varepsilon},\ \underset{\sim}{e}\cdot\underset{\sim}{e},\ \ \underset{\sim}{e}\cdot\underset{\sim\sim}{nn}\cdot\underset{\sim}{e},$$

$$\underset{\sim\sim}{nn}\cdot\underset{\sim}{\varepsilon}\cdot\underset{\sim}{\varepsilon}+\underset{\sim}{\varepsilon}\cdot\underset{\sim}{\varepsilon}\cdot\underset{\sim\sim}{nn},\ \ \underset{\sim}{\varepsilon}\cdot\underset{\sim}{\varepsilon}\cdot\underset{\sim}{\varepsilon},\ \ \underset{\sim}{\varepsilon}\cdot\underset{\sim\sim}{nn}\cdot\underset{\sim}{\varepsilon}\cdot\underset{\sim}{\varepsilon}+\underset{\sim}{\varepsilon}\cdot\underset{\sim}{\varepsilon}\cdot\underset{\sim\sim}{nn}\cdot\underset{\sim}{\varepsilon},\ \text{etc.}$$

These contain independent $\underset{\sim}{T}_k$ among them as a subset. Wineman and Pipkin (1964) implies that there are only six $\underset{\sim}{T}_k$. By visualizing each symmetric tensor as a 6-D vector, the first six are easily shown to be independent; the others have been demonstrated dependent.

Thus, equation (VII-3) becomes

$$\underset{\sim}{\sigma} = f_a\underset{\sim}{\delta} + f_b\underset{\sim\sim}{nn} + f_c\underset{\sim}{\varepsilon} + f_d[\underset{\sim}{\varepsilon}\cdot\underset{\sim\sim}{nn}+\underset{\sim\sim}{nn}\cdot\underset{\sim}{\varepsilon}] +$$

$$f_e\underset{\sim}{\varepsilon}\cdot\underset{\sim}{\varepsilon} + f_g\underset{\sim}{\varepsilon}\cdot\underset{\sim\sim}{nn}\cdot\underset{\sim}{\varepsilon} \qquad \text{(VII-4)}$$

where the f_k are functions of a set of independent invariants. There are five of the latter: in principal strain axes, we need only specify the three principal strains and two direction cosines for the material axis. The simpler invariants we actually employ are:

$$J_1 = \underset{\sim}{\delta}:\underset{\sim}{\varepsilon} = \varepsilon_{11}+\varepsilon_{22}+\varepsilon_{33} \qquad \text{(VII-5)}$$

$$J_{01} = \underset{\sim}{nn}:\varepsilon = \varepsilon_{22}\sin^2\theta+2\varepsilon_{23}\sin\theta\cos\theta+\varepsilon_{33}\cos^2\theta$$

$$J_2 = \underset{\sim}{\varepsilon}:\underset{\sim}{\varepsilon} = \varepsilon_{11}^2+\varepsilon_{22}^2+\varepsilon_{33}^2+2(\varepsilon_{12}^2+\varepsilon_{23}^2+\varepsilon_{13}^2)$$

$$J_{02} = \underset{\sim}{nn}:\underset{\sim}{\varepsilon}\cdot\underset{\sim}{\varepsilon} = \sin^2\theta\ (\varepsilon_{12}^2+\varepsilon_{22}^2+\varepsilon_{23}^2) + 2\sin\theta\ \cos\theta(\varepsilon_{12}\varepsilon_{13}+\varepsilon_{22}\varepsilon_{23}+\varepsilon_{23}\varepsilon_{33})+\cos^2\theta(\varepsilon_{13}^2+\varepsilon_{23}^2+\varepsilon_{33}^2)$$

$$J_3 = \underset{\sim}{\varepsilon}\cdot\underset{\sim}{\varepsilon}:\underset{\sim}{\varepsilon} = \varepsilon_{11}(\varepsilon_{11}^2+\varepsilon_{12}^2+\varepsilon_{13}^2)+\varepsilon_{22}(\varepsilon_{12}^2+\varepsilon_{22}^2+\varepsilon_{23}^2) + \varepsilon_{33}(\varepsilon_{13}^2+\varepsilon_{23}^2+\varepsilon_{33}^2)+2[\varepsilon_{12}(\varepsilon_{11}\varepsilon_{12}+\varepsilon_{12}\varepsilon_{22}+\varepsilon_{13}\varepsilon_{23})+\varepsilon_{13}(\varepsilon_{11}\varepsilon_{13}+\varepsilon_{12}\varepsilon_{23}+\varepsilon_{13}\varepsilon_{33}) + \varepsilon_{23}(\varepsilon_{12}\varepsilon_{13}+\varepsilon_{22}\varepsilon_{23}+\varepsilon_{23}\varepsilon_{33})] .$$

Each function f_k of the invariants is expanded as a polynomial in increasing powers of strain components, for future convenience:

$$f_k = k_0 + k_1 J_1 + k_2 J_{01} + k_3 J_1^2 + k_4 J_0^2 + k_5 J_1 J_{01} + k_6 J_2$$

$$+ k_7 J_{02} + k_8 J_1 J_2 + k_9 J_1 J_{02} + k_{10} J_{01} J_2 + k_{11} J_{01} J_{02}$$

$$+ k_{12} J_3 + k_{13} J_1^3 + k_{14} J_{01}^3 + k_{15} J_1^2 J_{01} + k_{16} J_1 J_{01}^2 +$$

$$+ \text{4th order} + \cdots \quad . \qquad \text{(VII-6)}$$

We can truncate this expression, either in the spirit of a Taylor Series (for local accuracy about zero strain), or for definiteness and simplicity in curve fitting to some appropriate global accuracy.

For reference, we now write the stress components in terms of the f_k and the components of the six tensors:

$$\sigma_{11} = f_a + f_c \varepsilon_{11} + f_e(\varepsilon_{11}^2 + \varepsilon_{12}^2 + \varepsilon_{13}^2) + f_g(\varepsilon_{12}\sin^2\theta + \varepsilon_{13}\cos\theta)^2$$

$$\sigma_{22} = f_a + f_b \sin^2\theta + f_c \varepsilon_{22} + 2f_d(\sin^2\theta\ \varepsilon_{22} + \sin\theta\ \cos\theta\ \varepsilon_{23}) +$$

$$f_e(\varepsilon_{12}^2 + \varepsilon_{22}^2 + \varepsilon_{23}^2) + f_g(\varepsilon_{22}\sin\theta + \varepsilon_{23}\cos\theta)^2 \qquad \text{(VII-7)}$$

$$\sigma_{33} = f_a + f_b \cos^2\theta + f_c \varepsilon_{33} + 2f_d(\cos\theta\ \sin\theta\ \varepsilon_{32} + \cos^2\theta\ \varepsilon_{33})] +$$

$$f_e(\varepsilon_{13}^2 + \varepsilon_{23}^2 + \varepsilon_{30}^2) + f_g(\varepsilon_{23}\sin\theta + \varepsilon_{33}\cos\theta)^2$$

$$\sigma_{23} = f_b \sin\theta\ \cos\theta + f_c \varepsilon_{23} + f_d[\varepsilon_{23} + \cos\theta\ \sin\theta(\varepsilon_{22} + \varepsilon_{33})] +$$

$$f_e(\varepsilon_{12}\varepsilon_{13} + \varepsilon_{22}\varepsilon_{23} + \varepsilon_{23}\varepsilon_{33}) + f_g(\varepsilon_{22}\sin\theta + \varepsilon_{23}\cos\theta)(\varepsilon_{23}\sin\theta +$$

$$\varepsilon_{33}\cos\theta)$$

$$\sigma_{13} = f_c \varepsilon_{13} + f_d(\varepsilon_{12}\cos\theta\sin\theta + \varepsilon_{13}\cos^2\theta) + f_e(\varepsilon_{11}\varepsilon_{13} + \varepsilon_{12}\varepsilon_{23} + \varepsilon_{13}\varepsilon_{33}) +$$

$$f_g(\varepsilon_{12}\sin\theta + \varepsilon_{13}\cos\theta)(\varepsilon_{32}\sin\theta + \varepsilon_{33}\cos\theta)$$

$$\sigma_{12}=f_c\varepsilon_{12}+f_d(\varepsilon_{12}\sin^2\theta+\varepsilon_{13}\sin\theta\cos\theta)+f_e(\varepsilon_{11}\varepsilon_{12}+\varepsilon_{12}\varepsilon_{22}+\varepsilon_{13}\varepsilon_{32})+f_g(\varepsilon_{12}\sin\theta+\varepsilon_{13}\cos\theta)(\varepsilon_{22}\sin\theta+\varepsilon_{23}\cos\theta)\ .$$

The experimental results are in the form of plots of strain components versus applied stress components (usually 1 or 3). These data can be introduced into the model in a number of ways. Cleary (priv. comm. 1979) suggests we seek groups of parameters activated and determined by our experiments, and when these are isolated, investigate whether these groups (or combinations of them) are sufficient to carry out structural calculations of interest. In other words, without specifically seeking to determine the polynomial coefficients in (VII-6) directly, we inquire whether useful groups of them are determined by our experiments.

Some easily determined numbers are the coefficients of simple polynomial curve fitting between each stress and one strain component. These coefficients can be written as combinations of model parameters if all other strain components are represented as polynomials in the first (using cross - plots from the experiment); substitution in the constitutive relation then gives each stress as a polynomial in the one strain. In the cases when $\varepsilon_{12}=\varepsilon_{13}=0$ (as is true by symmetry for all our experiments), σ_{12} and σ_{13} vanish identically; their representations yield no information.

Since the model will be used in truncated form, we must specify precisely the order of representation of each strain in ε_{33} (arbitrarily chosen as the primary

Strain). We propose to employ maximum order without surpassing the truncation.

A truncation to cubic order employs all the invariants and requires representation of strain components to as much as 3rd order in ε_{33}. If the strains should be quite accurately radial, however, the representations will be linear with no constant term: $\varepsilon_{22} = E_{22}\varepsilon_{33}$, $\varepsilon_{23} = E_{23}\varepsilon_{33}$, etc., where E_{ij} are constants. This linearity seemed to hold approximately in our case. Note that such radial response to radial loading could also be incorporated into the model at an earlier stage. The f_k polynomials are truncated at such order that each $f_k T_k$ is cubic at most, then ε_{ij} is everywhere replaced in equations (VII-7 and VII-6) as above, and terms of various order in ε_{33} are collected.

For simplicity, however, we use the quadratic truncation (thus never employing J_3), and acknowledge the absence by symmetry of strain components ε_{13}, ε_{12} in the following simplified notation:

$$\varepsilon_{11} = \bar{E}\varepsilon$$

$$\varepsilon_{22} = \hat{E}\varepsilon \qquad \text{(VII-8)}$$

$$\varepsilon_{23} = \tilde{E}\varepsilon$$

$$\varepsilon_{33} = \varepsilon \quad .$$

(recall that $\bar{E}$, $\hat{E}$, $\tilde{E}$ are experimentally determined).

Substituting eqns.(VII-8) into (VII-5 and VII-6) and these into eqns. (VII-7), yields:

$$\begin{aligned}\sigma_{11} = [a_0] + \varepsilon\{&C_0\bar{E}+a_1(\bar{E}+\hat{E}+1)+a_2(\hat{E}\sin^2\theta+2\tilde{E}\sin\theta\cos\theta+\cos^2\theta\}\\ &+\varepsilon^2\{a_3(\bar{E}+\hat{E}+1)^2+a_4(\hat{E}\sin^2\theta+2\tilde{E}\sin\theta\cos\theta+\cos^2\theta)^2\\ &+a_5(\hat{E}\sin^2\theta+2\tilde{E}\sin\theta\cos\theta+\cos^2\theta)(\bar{E}+\hat{E}+1)\\ &+a_6(\bar{E}^2+\hat{E}^2+1+2\tilde{E}^2)+a_7(\sin^2\theta(\hat{E}^2+\tilde{E}^2)+\\ &2\sin\theta\cos\theta(\hat{E}\tilde{E}+\tilde{E})+\cos^2\theta(\tilde{E}^2+1))+C_1\bar{E}(\bar{E}+\hat{E}+1)\\ &+C_2\bar{E}(\hat{E}\sin^2\theta+2\tilde{E}\sin\theta\cos\theta+\cos^2\theta)+e_0(\bar{E}^2)\}\end{aligned} \qquad \text{(VII-9)}$$

$$\begin{aligned}\sigma_{22} = [a_0 + b_0\sin^2\theta] + \varepsilon\{&(a_1+b_1\sin^2\theta)(\bar{E}+\hat{E}+1)+(a_2+b_2\sin^2\theta)(\hat{E}\\ &\sin^2\theta+2\tilde{E}\sin\theta\cos\theta+\cos^2\theta)+C_0\hat{E}+2d_0(\sin^2\theta\hat{E}+\\ &\sin\theta\cos\theta\,\tilde{E})\}+\varepsilon^2\{(a_3+b_3\sin^2\theta)(\bar{E}+\hat{E}+1)^2+(a_4+b_4\sin^2\theta)\\ &(\hat{E}\sin^2\theta+2\tilde{E}\sin\theta\cos\theta+\cos^2\theta)^2+(a_5+b_5\sin^2\theta)(\hat{E}\sin^2\theta+\\ &2\tilde{E}\cos\theta\sin\theta+\cos^2\theta)(\bar{E}+\hat{E}+1)+(a_6+b_6\sin^2\theta)(\bar{E}^2+\hat{E}^2+\\ &1+2\tilde{E}^2)+(a_7+b_7\sin^2\theta)[\sin^2\theta(\hat{E}^2+\tilde{E}^2)+2\sin\theta\cos\theta\end{aligned}$$

$$(\hat{E}\tilde{E}+\tilde{E})+\cos^2\theta(\tilde{E}^2+1)]+[\hat{E}c_1+2d_1(\sin^2\theta\hat{E}+\sin\theta\cos\tilde{E})]$$

$$(\bar{E}+\hat{E}+1)+(\hat{E}\sin^2\theta+2\tilde{E}\sin\theta\cos\theta+\cos^2\theta)[\hat{E}c_2+2d_2(\sin^2\theta$$

$$\hat{E}+\sin\theta\cos\theta\tilde{E})]+e_0(\hat{E}^2+\tilde{E}^2)+g_0(\hat{E}\sin\theta+\tilde{E}\cos\theta)^2\}$$

$$\sigma_{33} = (a_0+b_0\cos^2\theta)+\varepsilon\{(a_1+b_1\cos^2\theta)(\bar{E}+\hat{E}+1)+(a_2+b_2\cos^2\theta)$$

$$(\hat{E}\sin^2\theta+2\tilde{E}\sin\theta\cos\theta+\cos^2\theta)+c_0+2d_0(\cos\theta\sin\theta\tilde{E}+$$

$$\cos^2\theta)\}$$

$$+\varepsilon^2\{(a_3+b_3\cos^2\theta)(\bar{E}+\hat{E}+1)^2+(a_4+b_4\cos^2\theta)(\hat{E}\sin^2\theta+$$

$$2\tilde{E}\sin\theta\cos\theta+\cos^2\theta)^2+(a_5+b_5\cos^2\theta)(\hat{E}\sin^2\theta+2\tilde{E}\sin\theta$$

$$\cos\theta+\cos^2\theta)(\bar{E}+\hat{E}+1)+(a_6+b_6\cos^2\theta)(\bar{E}^2+\hat{E}^2+1+2\tilde{E}^2)$$

$$+(a_7+b_7\cos^2\theta)[\sin^2\theta(\hat{E}^2+\tilde{E}^2)+2\sin\theta\cos\theta(\hat{E}\tilde{E}+\tilde{E})+$$

$$\cos^2\theta(\tilde{E}^2+1)]+(c_1+2d_1(\cos\theta\sin\theta\tilde{E}+\cos^2\theta))(\bar{E}+\hat{E}+1)$$

$$+[c_2+2d_2(\cos\theta\sin\theta\tilde{E}+\cos^2\theta)](\hat{E}\sin^2\theta+2\tilde{E}\sin\theta\cos\theta+$$

$$\cos^2\theta)$$

$$+e_0(\tilde{E}^2+1)+g_0(\tilde{E}\sin\theta+\cos\theta)^2\}$$

$$\sigma_{23} = [(b_0\sin\theta\cos\theta)]+\varepsilon\{\sin\theta\cos\theta[b_1(\bar{E}+\hat{E}+1)+b_2(\hat{E}\sin^2\theta+$$

$$2\tilde{E}\sin\theta\cos\theta+\cos^2\theta)]+\tilde{E}\,c_0+d_0(\tilde{E}+\cos\theta\sin\theta(\hat{E}+1))\}$$

$$+\varepsilon^2\{\sin\theta\cos\theta[b_3(\bar{E}+\hat{E}+1)^2+b_4(\hat{E}\sin^2\theta+2\tilde{E}\sin\theta\cos\theta+$$

$$\cos^2\theta)^2+b_5(\hat{E}\sin^2\theta+2\tilde{E}\sin\theta\cos\theta+\cos^2\theta)(\bar{E}+\hat{E}+1)+$$

$$b_6(\bar{E}^2+\hat{E}^2+1+2\tilde{E}^2)+b_7(\sin^2\theta(\hat{E}^2+\tilde{E}^2)+2\sin\theta\cos\theta(\hat{E}\tilde{E}+\tilde{E})+\cos^2\theta(\tilde{E}^2+1))]+[\tilde{E}c_1+d_1(\tilde{E}+\cos\theta\sin\theta(\hat{E}+1))](\hat{E}+\bar{E}+1)+[\tilde{E}c_2+d_2(\tilde{E}+\cos\theta\sin\theta(\hat{E}+1))](\hat{E}\sin^2\theta+2\tilde{E}\sin\theta\cos\theta+\cos^2\theta)+e_0(\hat{E}+1)\tilde{E}+g_0(\hat{E}\sin\theta+\tilde{E}\cos\theta)(\tilde{E}\sin\theta+\cos\theta)\}$$

and

$\sigma_{12} = 0$; $\sigma_{13} = 0$; this follows from eqns. VII-7 when $\varepsilon_{12}=\varepsilon_{13}=0$, so these relations yield no information.

Results:

The coefficients in the above quadratic expressions (VII-9) are renamed for simplicity, and the constant terms dropped in deference to experiment:

$\theta = 0°$ $\sigma_{nn} = A_{nn}\,\varepsilon_{nn} + B_{nn}\,\varepsilon_{nn}^2$ (VII-10)

$\sigma_{nn} = A_{nm}\,\varepsilon_{mm} + B_{nm}\,\varepsilon_{mm}^2$, $\varepsilon_{mm}=E_{mm}\,\varepsilon_{nn}$

$\theta = 90°$ $\sigma_{mm} = A_{mm}\,\varepsilon_{mm} + B_{mm}\,\varepsilon_{mm}^2$

$\sigma_{mm} = A_{mn}\,\varepsilon_{nn} + B_{mn}\,\varepsilon_{nn}^2$, $\varepsilon_{nn}=E_{nn}\,\varepsilon_{mm}$

$\sigma_{mm} = A_{mt}\,\varepsilon_{tt} + B_{mt}\,\varepsilon_{tt}^2$, $\varepsilon_{tt}=E_{tt}\,\varepsilon_{mm}$

$\theta = 45°$ $\sigma_{33} = A_{33}\,\varepsilon_{33} + B_{33}\,\varepsilon_{33}^2$

$\sigma_{33} = A_{32}\,\varepsilon_{22} + B_{32}\,\varepsilon_{22}^2$, $\varepsilon_{22}=E_{22}\,\varepsilon_{33}$

$\sigma_{33} = A_{31}\,\varepsilon_{11} + B_{31}\,\varepsilon_{11}^2$, $\varepsilon_{11}=E_{11}\,\varepsilon_{33}$

$\sigma_{33} = A_{3S}\,\varepsilon_{32} + B_{3S}\,\varepsilon_{32}$, $\varepsilon_{32}=E_{32}\,\varepsilon_{33}$

The quadratic curve fits for determination of the relevant coefficients in eqns. (VII-9) at various temperatures are presented in Table XI.

The linear strain fits (i.e., eqns. VII-8), determined from the same plots used for the stress-strain fitting, are shown in Table XII.

The particular specimen plots employed in the curve fitting procedure, along with the range of strain values, are then presented in Table XIII.

TABLE XI

QUADRATIC CURVE FITS

Coefficient	21°	38°	98°	121°	204°
A_{nn}	10.9	3.82	1.02	.621	.362
B_{nn}	.389	1.26	.0121	.00533	-0.72
A_{nm}	-38.2	-27.0	-1.78	-1.60	-
B_{nm}	4.81	-41.4	.0365	.0385	-
A_{mm}	16.4	3.68	2.57	.994	.192
B_{mm}	.839	.450	.0493	-.0129	- .00602
A_{mn}	-24.1	-8.45	-1.45	-1.29	-
B_{mn}	-1.40	-27.2	- .0896	- .0297	-
A_{mt}	-55.6	-11.4	-2.23	-1.73	-
B_{mt}	12.3	-4.77	.0155	.00740	-
A_{33}	17.9	8.26	5.45	1.10	.248
B_{33}	.805	1.44	.162	- .0105	- .00912
A_{32}	-35.2	-22.5	-3.28	2.84	-
B_{32}	4.25	10.6	.0124	.0750	-
A_{31}	-51.1	-28.0	-4.36	2.87	-
B_{31}	6.78	36.1	.0779	.0522	-
A_{3S}	37.8	-	21°C only	-	-
B_{3S}	-2.90				-

TABLE XII

LINEAR STRAIN FITS

Core Orientation	Coefficient	Temperature (°C) 21°	38°	93°	121°
θ=0°	$\bar{E}=\hat{E}$	- .37	- .18	- .59	- .63
θ=45°	$\bar{E}$	- .34	- .42	- .99	- .53
	$\hat{E}$	- .64	- .37	-1.14	- .71
	$\tilde{E}$	..25	(21°C only)		
θ=90°	$\hat{E}$	- .42	- .52	- .91	- .77
	$\bar{E}$	- .53	- .37	- .97	- .74

TABLE XIII

INDIVIDUAL SPECIMEN PLOTS AND RANGE OF STRAIN VALUES EMPLOYED IN CURVE FITS

Core Orientation	Temp.(°C)	Specimens Used	Range of strain values for curve fits ($m\varepsilon$)
θ=0°	21°	1FH8/1F3	$\bar{e}_{nn}$: .20 to -12
			$\bar{e}_{mm}$: .24 to - 4.8
	38°	1F6	$\bar{e}_{nn}$: .50 to 0
			$\bar{e}_{mm}$: .095 to 0
	93°	1FH2/1F4	$\bar{e}_{nn}$: .40 to -57
			$\bar{e}_{mm}$: .31 to -35
	121°	1FH3/1F8	$\bar{e}_{nn}$: .77 to -45
			$\bar{e}_{mm}$: .26 to -28
	204°	1FH5	$\bar{e}_{nn}$: 0 to -24
θ=45°	21°	2FH6/2F2	$\bar{e}_{33}$: .38 to - 6.0
			$\bar{e}_{22}$: .24 to - 3.9
			$\bar{e}_{11}$: .15 to - 2.0
			$\bar{e}_{32}$: 0 to - 1.5
	38°C	2F3	$\bar{e}_{33}$: .80 to 0
			$\bar{e}_{22}$: .30 to 0
			$\bar{e}_{11}$: .35 to 0
	93°C	2FH3/2F5	$\bar{e}_{33}$: .30 to -15
			$\bar{e}_{22}$: .14 to -20
			$\bar{e}_{11}$: .20 to -15
	121°	2F44	$\bar{e}_{33}$: 0 to -20.
			$\bar{e}_{22}$: 0 to -13
			$\bar{e}_{11}$: 0 to -14
	204°	2FH8	$\bar{e}_{33}$: 0 to -22

APPENDIX VIII

STRENGTH ENVELOPES DERIVATION

The following characterization of the shale strength to various loading parameters, i.e., using strength envelopes, was derived from the following equation (Cleary-priv. comm., 1979):

$$F(\sigma_{ij}) = 0 \quad . \tag{VIII-1}$$

As in the derivation of the generalized constitutive relation for the macroscopic transverse isotropy in oil shale, the scalar invariants (this time in stress) are, to second order:

$$J_1 = \underset{\sim}{\delta}:\underset{\sim}{\sigma} = \sigma_{11} + \sigma_{22} + \sigma_{33} \tag{VIII-2}$$

$$J_{01} = \underset{\sim}{nn}:\underset{\sim}{\sigma} = \sigma_{22}\sin^2\theta + 2\sigma_{23}\sin\theta\cos\theta + \sigma_{33}\cos^2\delta$$

$$J_2 = \underset{\sim}{\sigma}:\underset{\sim}{\sigma} = \sigma_{11}^2 + \sigma_{22}^2 + \sigma_{33}^2 + 2(\sigma_{12}^2+\sigma_{23}^2+\sigma_{13}^2)$$

$$J_{02} = \underset{\sim}{nn}:\underset{\sim}{\sigma}\cdot\underset{\sim}{\sigma} = \sin^2\theta(\sigma_{12}^2\sigma_{22}^2\sigma_{23}^2) + 2\sin\theta\cos\theta(\sigma_{12}\sigma_{13} + \sigma_{22}\sigma_{23} + \sigma_{23}\sigma_{33}) + \cos^2\theta(\sigma_{13}^2+\sigma_{23}^2+\sigma_{33}^2)$$

From eqn. VIII-1, the combinations of scalar invariants take the form, to 2nd order:

$$F = 0 \equiv f_0 + f_1 J_1 + f_2 J_{01} + f_3 J_1^2 + f_4 J_{01}^2 + f_5 J_1 J_{01}$$

$$+ f_6 J_2 + f_7 J_{02} + \cdots\cdots \qquad \text{(VIII-3)}$$

Substituting eqn. VIII-2 into eqn. VIII-3 yields, after simplification:

$$F = 0 = f_0 + f_1(\sigma_{11}+\sigma_{22}+\sigma_{33}) + f_2(\sigma_{22}\sin^2\theta + 2\sigma_{23}\sin\theta\cos\theta +$$

$$\sigma_{33}\cos^2\theta) + f_3(\sigma_{11}^2+\sigma_{22}^2+\sigma_{33}^2) + 2(\sigma_{11}\sigma_{22}+\sigma_{11}\sigma_{33}+\sigma_{22}\sigma_{33})) +$$

$$f_4[\sigma_{22}^2\sin^4\theta + 4\sigma_{23}^2\sin^2\theta\cos^2\theta + \sigma_{33}^2\cos^4\theta +$$

$$2(2\sigma_{22}\sigma_{23}\sin^3\theta\cos\theta +$$

$$\sigma_{22}\sigma_{33}\sin^2\theta\cos^2\theta + 2\sigma_{23}\sigma_{33}\sin\theta\cos^3\theta)2 +$$

$$f_5[(\sigma_{11}+\sigma_{22}+\sigma_{33})(\sigma_{22}\sin^2\theta + 2\sigma_{23}\sin\theta\cos\theta + \sigma_{33}\cos^2\theta)] +$$

$$f_6[\sigma_{11}^2+\sigma_{22}^2+\sigma_{33}^2+2(\sigma_{12}^2+\sigma_{23}^2+\sigma_{13}^2)] +$$

$$f_7[\sin^2\theta(\sigma_{12}^2+\sigma_{22}^2+\sigma_{23}^2)+2\sin\theta\cos\theta(\sigma_{12}\sigma_{13}+\sigma_{22}\sigma_{23} +$$

$$\sigma_{23}\sigma_{33})+\cos^2\theta(\sigma_{13}^2+\sigma_{23}^2+\sigma_{33}^2)] + \cdots \qquad \text{(VIII-4)}$$

Solution of equation VIII-4 was initiated from the failure strengths of oil shale at various values of θ and confining stresses (uniaxial and triaxial tests). For the tests performed, herein, equation VIII-4 was simplified to the following equations (using σ_c for confining stress):

$$\theta = 0°: \quad F=0=f_0+(2f_1\sigma_c+4f_3\sigma_c^2+2f_6\sigma_c^2) + (f_1+f_2+4f_3\sigma_c+2f_5\sigma_c)\sigma_{nn}+(f_3+f_4+f_5+f_6+f_7)\sigma_{nn}^2 \qquad \text{(VIII-5)}$$

$$\theta = 90°: \quad F=0=f_0+(2f_1\sigma_c+f_2\sigma_c+4f_3\sigma_c^2+f_4\sigma_c^2+ 2f_5\sigma_c^2+2f_6\sigma_c^2+f_7\sigma_c^2)+(f_1+4f_3\sigma_c+f_5\sigma_c)\sigma_{mm} + (f_3+f_6)\sigma_{mm}^2 .$$

Of course, the coefficients f_k are actually functions of temperature. The data used to find these from equations VIII-5 are presented in Table XIV. More tests at confinement at temperatures greater than 21°C are needed for the solution, as well as tests using various ratios of σ_A/σ_C, where $\sigma_A = \sigma_{33} - \sigma_C$; for instance, we let σ_A be small while σ_c fails the specimen, again at various θ to bedding. These types of tests are currently in progress.

TABLE XIV

DATA FOR STRENGTH ENVELOPE CHARACTERIZATIONS

Core Orientation	Confining stress: σ_c MPa(psi)	Temp. (°C)	Axial Failure Strenth - MPa (psi)	
θ=0°	< 0.1 (<15)	21°	72.5	(10,500)
	< 0.1 (<15)	93°	30.3	(4,400)
	< 0.1 (<15)	121°	21.4	(3,100)
	< 0.1 <15)	204°	15.2	(2,200)
	20.7 (3000)	21°	147	(21,300)
	34.5 (5000)	21°	179	(26,000)
	69.0(10000)	21°	257	(37,200)
θ=90°	< 0.1 (<15)	21°	64.9	(9,400)
	< 0.1 (<15)	93°	30.3	(4,400)
	< 0.1 (<15)	121°	18.6	(2,700)
	< 0.1 (<15)	204°	9.7	(1,400)
	20.7 (3000)	21°	141	(20,400)
	59.0(10000)	21°	233	(33,800)
θ=45°	< 0.1 (<15)	21°	63.4	(9,200)
	< 0.1 (<15)	38°	60.0	(8,700)
	< 0.1 (<15)	93°	45.5	(6,600)
	< 0.1 (<15)	121°	31.0	(4,500)
	< 0.1 (<15)	204°	9.0	(1,300)

REFERENCES

Abou, Sayed, A. S. — "Fracture Toughness, K_{IC} of Triaxially Loaded Indiana Limestone", pps. 2A8, 1-8, in Proc. 18th U.S. Symp. on Rock Mech., published by Colorado School of Mines (CSM) Press, June, 1977.

Allred, V. D. — "Shale Oil Recovery from Fractured Oil Shale", published by Marathon Oil Co., U.S. patent #3,730,270, 1974.

Amazigo, J. C. Hutchinson, J.W. — "Crack-Tip Fields in Steady Crack Growth with Linear Strain Hardening," J. Mech. Phys. Solids, 25, 2, 8, 1977.

Begley, J. A. Landes, J. D. — "The J-integral as a Fracture Criterion," 1971 Nat. Symp. on Frac. Mech. Part II, ASTM, STP 514, 1971.

Bowie, O.L. Freese, C. E. — "Central Crack in Plane Orthotropic Rectangular Sheet," Int. Jour. Frac. Mech., 8, 1, 49-58, 1972.

Brace, W. F. — "Micromechanics in Rock Systems", Structure, Solid, Mechanics and Engineering Design, ed. by M. Te'eni, Wiley-Interscience, London, 1971.

Bridges, J.E. Tafloue, A. Snow, R. H. — "Net Energy Recoveries for the In-Situ Dielectric Heating of Oil Shale," presented at IIT Research Inst., Chicago, June 6, 1978.

Busey, H. M. — "Method of Extracting Oil and By-Products from Oil Shale," spon. by McDonnell Douglas Corp., U.S. Pat. 3,596,993, 1972.

REFERENCES (CONTINUED)

Cameron Engineers, Inc. "A Technical and Economic Study of Candidate Underground Mining Systems for Deep, Thick, Oil Shale Deposits," Phase I, Report, USBM Contract SO 241074, July 1975.

Carpenter, H.C. Sohns, H.W. "Development of Technology for In-Situ Oil Shale Processes," Proc. 7th Oil Shale Symp., CSM Quart. 69, 2, 1974.

Cleary, M. P. Class Notes, MIT Course 2.074, "Mechanics of Porous/Geological Materials," Fall, 1977.

Cleary, M. P. "Fracture Discontinuities and Structural Analysis in Resource Recovery Endeavors," J. Pressure Vessel Tech., 100, 1-11, Feb. 1978a.

Cleary, M. P. "Some Deformation and Fracture Characteristics of Oil Shale," pp. 72-82 in Vol. II of Proc. 19th U.S. Symp. on Rock Mech., pub. by Mackay School of Mines, May, 1978b.

Cleary, M. P. "Underground Fracturing for Enhanced Recovery of Oil and Gas," Report to Marathon Oil Co., Sept., 1978c.

Cleary, M. P. "Primary Factors Governing Hydraulic Fractures in the Heterogeneous Stratified Porous Formations," ASME Paper No. 78-Pet 47, presented at Energy Tech. Conf. and Exhibition, Houston, TX, Nov. 1978d.

REFERENCES (CONTINUED)

Clifton, R. J.
Simonson, E. R.
Jones, A. H.
Green, S. J.
"Determination of the Critical Stress-Intensity Factor K_{IC} from Internally Pressurized Thick-Walled Vessels,", Exp. Mech., 16, 6, 1976.

Closmann, P. J.
Nordgren, R. P.
"Method of Producing Shale Oil from a Subterranean Oil Shale Formation" spon. by Shell Oil Co., U.S. Pat. 3,501,201, 1968.

Cook, N. G.
Harvey, V. P.
"An Appraisal of Rock Excavation by Mechanical Hydraulic, Thermal and Electromagnetic Means", Proc. 3rd Cong. of Int. Soc. for Rock Mech., in Advances in Rock Mechanics, 13, 1599, 1974.

Cunningham, R. A.
"An Empirical Approach for Relating Drilling Parameters," presented at SPE-AIME 52nd Annual Fall Tech. Conf. and Exhibition, Denver, Oct., 1977.

Dravo Corporation
"Analysis of Large Scale Non-coal Underground Mining Methods", Report to USBM, Contract SO 122059, Jan. 1974.

East, J. H.
Gardner, E. D.
"Oil Shale Mining, Rifle, Colorado, 1944-56", USBM Bulletin 611, 1964.

Einstein, H. H.
Class Notes, MIT Course 1.342 "Rock Mechanics II", Spring, 1978.

Einstein, H. H.
Alva-Hurtado, J. E.
"A Review of Equipment Available for In-Situ Testing of Soil," MIT Source, Cambridge, Sept., 1975.

REFERENCES (CONTINUED)

Ellington, R.T. — "Method of Retorting Oil Shale In Situ", spons. by Atlantic Richfield Co., U.S. patent 3,586,377, 1972.

Felix, D.T.
Pelifsky, A.H.
Herbert, G.N. — "Use of Sonic Energy for Rupturing Molecular Bonds in Shale Oil Recovery", spons. by Resources Research and Development Corp., S.African patent 69,08,905, 1974.

Fenix and Scisson Inc. — "Technical and Economic Study of an Underground Mining, Rubblization and In Situ Retorting System for Deep Oil Shale Deposits", Phase I Report, USBM Contract SO 241073, Aug. 1975.

Gandhi, K.R. — "Analysis of an Inclined Crack Centrally Placed in an Orthotropic Rectangular Plate", Jour. Strain Analysis, 7, 3, 157-162, 1972.

Garret, D.E. — "In Situ Process for Recovery of Carbanaceaus Materials from Subterraneous Deposits", spons. by Occidental Petroleum Corp., US patent 3,661,423, 1972.

Gilliland, H.E. — "In Situ Retorting of Oil Shale Using CO_2 as Heat Carrier", spons. by Continental Oil Co., US patent 3,480,082, 1971.

Grady, D.E.
Kipp, M.E. — "Oil Shale Fracture and Fragmentation at Higher Rates of Loading", in Proc. 20th US Symp. on Rock Mech., spons. by Univ. Texas at Austin, Austin, TX, June 4-6, 1979.

Grantmyre, I.
Hawkes, I.
"High Energy Impact Rock Breaking", reprint from The Canadian Mining and Metallurgic Bulletin, July, 1975.

Greenfield, R.J.
Shuck, L.Z.
Keech, T.W.
"Hydraulic Fracture Mapping Using Electrical Potential Measurements", In Situ 1(2), 147-169, 1977.

Hangen, J.A.
"A Study of Deformation and Fracture in Oil Shale", M.S. Thesis, MIT, Sept. 1977.

Hearmon, R.F.
"An Introduction to Anisotropic Elasticity", Oxford Univ. Press, Oxford, England, 1961.

Hendrickson, T.A.
"Oil Shale Processing Methods", Proc. 7th Oil Shale Symp. CSM Quart., 69, 2, 1974.

Herce, J.A.
"Method for Producing Shale Oil from an Oil Shale Formation", spons. by Shell Oil Co., US patent 3,593,790, 1972.

Hill, W.
"Slot-Cutting in Oil Shale," MS Thesis, MIT, Sept., 1979.

Hoagland, R.G.
Hahn, G.T.
Rosenfield, A.R.
"Influence of Microstructure on Fracture Propagation in Rocks", Rock Mechanics, 5, 77, 1973.

Jaeger, J.C.
Cook, N.G.W.
"Fundamentals of Rock Mechanics", pub. by Methuen & Co., Ltd., London, 1975.

James, R.F.
"The Current US Energy Situation", article appearing in Boston Globe, March 6, 1979.

Johnson, J.N.
"Dynamic Anisotropic Constitutive Relative for Oil Shale - Final Report", Terra Tek report TR D5-25 for Sandia Labs, Contr. No. 51-8488, June, 1975.

Lama, R.D.
Vutukuri, V.S.
"Handbook on Mechanical Properties of Rocks", Trans. Tech Publications, Clousthal, Germany, Vols. I and II, 1978.

McCarthy, H.E.
Cha, C.P.
"Oxy Modified In Situ Process Development and Update", pub. by Occidental Exploration and Prod. Co., Bakersfield, CA, 1977.

Merrill, R.H.
"Design of Underground Mine Opening, Oil Shale Mine, Rifle, Colorado", USBM RI 5089, 1954.

Miller, J.S.
Walken, C.J.
Eakin, J.L.
"Fracturing Oil Shale with Explosives for In Situ Oil Recovery", USBM RI 7874, 1974.

Obert, E.F.
"Internal Combustion Engines and Air Pollution", Harper and Row, New York, 1973.

Panel on Rock Mech. Problems of U.S. Nat. Comm. for Rock Mech.
"Limitations of Rock Mechanics in Energy-Resource Recovery and Development", pub. by Nat. Acad. of Sciences, Wash. D.C., 1978.

Paris, P.C.
Sih, G.C.
"Stress Analysis of Cracks", ASTM STP 381, Amer. Soc. Test Mat'l., 1965.

Parker, H.W.
"Production of Oil from a Nuclear Chimney in an Oil Shale by In Situ Combustion", spons. by Phillips Petroleum Co., US pat. 3,490,529, 1970.

Parker, J.
"Practical Rock Mechanics for Miners", pub. by White Pine Copper Co., Michigan, 1968.

Peterson, C.R.
"Mechanical Mining and In Situ Retorting of Oil Shale", Preprint Proc. 18th US Symp. on Rock Mech., Keystone, Colorado, June, 1977.

Peterson, C.R. — Class notes, MIT course 2.741 "Fundamentals of Mining Technology", Fall, 1978.

Prats, M. — "Permeabilizing by Acidizing Oil Shale Tuffaceous Streaks in and Oil Recovery Therefrom", spons. by Shell Oil Co., US pat. 3,481,398, 1968.

Purce, J.R. — "Procedure for In Situ Recovery of Minerals and Derivatives Thereof with the aid of Laser Beams", spons. by Woods R & D Co., 1975.

Raju, A.M. — "Elastic Static, and Dynamic Behavior of Layered Rifle Oil Shale and Coal", M.S. Thesis, CSM, T941, 1961.

Reed, R.P.
Boade, P.R. — "Stress Waves Measured and Calculated for In Situ Explosive Rubblization Experiments in Oil Shale", pp. 5B5, 1-7, in Proc. 18th US Symposium on Rock Mech., pub. by CSM Press, June, 1977.

Rice, J.R. — "A Path-Independent Integral and the Approximate Analysis of Strain Concentration by Notches and Cracks", J. Appl. Mech. Trans., 35, 3, 1968.

Rice, J.R.
Paris, P.C.
Merkle, J.G. — "Some Further Results of J-Integral Analysis and Estimates", Progress in Flow Growth and Frac. Tough. Test., ASTM STP 536, AMER. Soc. Test and Mat'l, 231, 1973.

Schmidt, R.A. — "Fracture Toughness Testing of Rock", in Closed Loop, pub. by MTS System Corp., 5, 3, 1975.

REFERENCES (CONTINUED)

Schmidt, R. A. — "Fracture Mechanics of Oil Shale -- Unconfined Fracture Toughness, Stress Corrosion Cracking, and Tension Test Results," pp. 2A2, r6, in Proc. 18th, U.S. Symp. Rock Mech., pub. by Colo. School of Mines Press, June 1977.

Schmidt, R. A.; Huddle, C. W. — "Fracture Mechanics of Oil Shale -- Some Preliminary Results," Sandia Labs Report SAND-76-0727, Feb., 1977.

Schmidt, R. A.; Schuler, K. W. — "Mechanical Properties of Oil Shale from Anvil Points under Uniaxial Compression", Sandia Lab Report SAND-74-0035, Aug., 1974.

Schuler, K. W. — "Lateral Deformation Gage for Rock Mechanics Testing", Sandia Lab. Report, preprint to Exp. Mech. Jour. 1977.

Sellers, J. B.; Haworth, G. R.; Zanbas, P. G. — "Rock Mechanics Research on Oil Shale Mining", SME/AIME Trans., 252, 2, 1972.

Simmons, G.; Brace, W. F. — "Comparison of Static and Dynamic Measurements of Compressibility of Rocks", J. Geophy. Res., 70, 22, 1965.

Smith, J. W. — "Theoretical Relationship Between Density and Oil Yield for Oil Shales," USBM RI 7248, 1969.

REFERENCES (CONTINUED)

Sohns, H. W. — "Feasibility of In-Situ Retorting of Green River Oil Shale Utilizing Nuclear Explosives for Fracturing," Proc. 3rd Int. Atomic Energy Agency -- Peaceful Nucl. Expl. Panel, Vienna, Austria 1974.

Ueber, R. C.; Van Mours, P.; Brew, J. R. — "Laterally Expanding Oil Shale Permeabilization," spons. by Shell Oil Co., U.S. Pat. 3,759, 328, 1974.

Walsh, J. B. — "The Effects of Cracks on the Compressibility of Rocks," J. Geophys. Res., 70, 2, 1965.

Walten, D. K.; Slusser, M. S. — "Method of Recovering Hydrocarbons from Oil Shale", Spons. by Mobil Oil Co., U. S. Pat. 3,542,131, 1971.

Wilkening, W. W. — "Dilatational Deformation and Fracture in Barre Granite," ScD Thesis, MIT, June, 1976.

Yen, T. F. — "Science and Technology of Oil Shale," pub. by Ann Arbor Science Publ., Inc., Ann Arbor, Mich., 1976a.

Yen, T. F. — "Oil Shale", pub. by Elsevier Scientific Pub. Comp., Amsterdam, 1976b.